Universidade de Aveiro
2020
Departamento de Eletrónica, Telecomunicações e Informática

Manuel dos Santos Neves

Laser Phase Noise Mitigation for Subcarrier-Multiplexing Optical Transmission Systems

Mitigação do Ruído de Fase dos Lasers em Sistemas de Transmissão Ótica Multiportadora

Universidade de Aveiro
2020
Departamento de Eletrónica, Telecomunicações e Informática

Manuel dos Santos Neves

Laser Phase Noise Mitigation for Subcarrier-Multiplexing Optical Transmission Systems

Mitigação do Ruído de Fase dos Lasers em Sistemas de Transmissão Ótica Multiportadora

Dissertação apresentada à Universidade de Aveiro para cumprimento dos requisitos necessários à obtenção do grau de Mestre em Engenharia Eletrónica e Telecomunicações, realizada sob orientação científica do Professor Doutor Paulo Miguel Nepomuceno Pereira Monteiro, Professor Associado do Departamento de Eletrónica, Telecomunicações e Informática da Universidade de Aveiro e sob a coorientação do Doutor Fernando Pedro Pereira Guiomar, Investigador do Instituto de Telecomunicações de Aveiro.

o júri / the jury

presidente / president

Prof. Doutor Pedro Miguel Ribeiro Lavrador
Professor Auxiliar do Departamento de Eletrónica, Telecomunicações e Informática da Universidade de Aveiro da Universidade de Aveiro

vogais / other members

Prof. Doutor Andrea Carena
Professor Associado do Politecnico Di Torino (arguente principal)

Prof. Doutor Paulo Miguel Nepomuceno Pereira Monteiro
Professor Associado do Departamento de Eletrónica, Telecomunicações e Informática da Universidade de Aveiro (orientador)

agradecimentos / acknowledgements

I would like to take this opportunity to say a few words of gratitude to the people and entities that made me able to achieve this work.
First of all, I want to thank my supervisor, Prof. Paulo Monteiro, for it was his determination and trust in me that, still in an early stage of my academic path, made me have the first contact with the optical communications research group, in Instituto de Telecomunicações, in Aveiro. Without him, I would never have followed this path, this path at which I know I will always be able to look back with pride and satisfaction.
I want to leave a sincere note of gratitude to Fernando Guiomar, Ph.D., for being an unquestionably good co-supervisor, as much as a good discussion colleague. He always showed a humble posture while also having valuable insights, which really motivated me to enter the world of research, without fear of making mistakes in the first steps.
Finally, I want to thank the entities that supported this work, the developed research was supported in part by the European Regional Development Fund through the Competitiveness and Internationalization Operational Program, Regional Operational Program of Lisbon, Regional Operational Program of the Algarve, in component FEDER, and the Foundation for Science and Technology, through the projects RETIOT (POCI-01-0145-FEDER-016432), ORCIP (CENTRO-01-0145-FEDER- 022141) and SOCA (CENTRO-01-0145-FEDER-000010).

keywords

Optical Communications, Coherent Optical Transmission Systems, Multi-Subcarrier Systems, Digital Signal Processing, Phase noise, Carrier Phase Estimation, Chromatic Dispersion

abstract

Multi-subcarrier optical systems have recently attracted the attention of the scientific and industrial communities, owing to their inherent advantages in terms of fiber propagation performance as well as their implementation complexity, when compared with legacy single-carrier systems. With the imminent introduction of next-generation transceivers supporting aggregate symbol-rates beyond 100 Gbaud, the achievable gains provided by multi-subcarrier modulation are becoming increasingly more important, thereby attracting the attention of several leader optical manufacturers, which are now including this technology in their portfolio.

However, the transition from single-carrier to multi-subcarrier modulation still requires significant optimization of digital signal processing subsystems, in order to maximize the inherent potential of subcarrier multiplexing.

In this thesis, techniques for carrier phase estimation are explored. The penalty associated with the usage of the methods used in single-carrier systems when changing to a multi-subcarrier system is quantitatively studied and the need for a change in such methods is evidenced.

Several jointly processing carrier phase estimation approaches are employed to improve the performance of phase recovery algorithms, resulting in an improvement in the power requirements for multi-subcarrier systems. In particular, a novel approach to carrier phase estimation is developed and assessed. This new method increases the tolerance of the system to chromatic dispersion and makes viable the usage of multi-subcarrier systems with a high number of subcarriers, highly outperforming any other carrier phase estimation approach for such systems.

Finally, a novel low-complexity implementation of a digital monitoring system is suggested. It is capable of measuring the laser line width of the transmitter and local oscillators lasers. This implementation is only made possible by the nature associated with the novel algorithm presented.

palavras-chave Comunicações Óticas, Sistemas de Transmissão Ótica Coerentes, Sistemas Multiportadora, Processamento Digital de Sinal, Ruído de Fase, Estimação da Fase da Portadora, Dispersão Cromática

resumo Os sistemas ópticos multiportadora atraíram recentemente a atenção das comunidades científicas e industriais, devido às suas vantagens inerentes em termos de desempenho de propagação de fibras, bem como da sua complexidade de implementação, quando comparados aos sistemas de portadora única. Com a introdução iminente de transceptores de última geração que suportam taxas agregadas de símbolos além de 100 Gbaud, os ganhos alcançáveis proporcionados pela modulação multiportadora estão a tornar-se cada vez mais importantes, atraindo assim a atenção de vários líderes no fabrico óptico, que agora incluem este tecnologia no seu portfólio. No entanto, a transição da modulação de portadora única para multiportadora ainda requer otimização significativa dos subsistemas de processamento de sinal digital, a fim de maximizar o potencial inerente da multiplexação de subportadoras.

Nesta tese, são exploradas técnicas para estimativa da fase portadora. A penalidade associada ao uso dos mesmos métodos utilizados em sistemas de transportadora única ao mudar para um sistema de múltiplas subportadoras é estudada quantitativamente e a necessidade de uma alteração desses métodos é evidenciada.

Várias abordagens de processamento conjunto entre as várias subportadoras são empregadas para melhorar o desempenho dos algoritmos de estimativa da fase portadora, resultando numa melhoria nos requisitos de energia para sistemas de múltiplas subportadoras. Em particular, uma nova abordagem para a estimativa da fase portadora é desenvolvida e avaliada. Este novo método aumenta a tolerância do sistema à dispersão cromática e viabiliza o uso de sistemas com um alto número de subportadoras, superando em desempenho qualquer outra abordagem de estimativa de fase portadora para estes sistemas.

Por fim, é sugerida uma nova implementação de baixa complexidade de um sistema de monitorização digital. É capaz de medir a largura da linha espectral dos lasers do transmissor e do oscilador local. Esta implementação só é possível devido às caracteristicas de implementação do novo algoritmo apresentado.

Contents

List of Tables

Intentionally blank page.

List of Figures

Intentionally blank page.

List of Acronyms

ADC Analog to Digital Converter

ASIC Application Specific Integrated Circuit

AWGN Additive White Gaussian Noise

B2B Back-to-Back

BASS Blind Adaptive Source Separation

BER Bit Error Rate

BPS Blind Phase Search

CD Chromatic Dispersion

CDE Chromatic Dispersion Equalization

CMA Constant Modulus Algorithm

CPE Carrier Phase Estimation

CPR Carrier Phase Recovery

CW Continuous Wave

DAC Digital to Analog Converter

DBP Digital Back Propagation

DFB Distributed Feedback

DRS Dual-Reference Subcarrier

DSP Digital Signal Processor

ECL External Cavity Laser

EDFA Erbium-Doped Fiber Amplifier

EEPN Equalization-Enhanced Phase Noise

FD-CDE Frequency Domain

FEC Forward Error Correction

FFT Fast Fourier Transform

FIR Finite Impulse Response

FPGA Field Programmable Gate Array

GMI Generalized Mutual Information

GVD Group-velocity Dispersion

IFFT Inverse FFT

IIR Infinite Impulse Response

IM·DD Intensity-Modulation and Direct-Detection

IQM In-phase and Quadrature Modulator

ISI Inter-Symbol Interference

JBPS Joint BPS

LED Light Emitting Diode

LLW Laser Line Width

LMS Least Mean Square

LO Local Oscillator

LPN Laser Phase Noise

M-PSK M− Phase Shift Keying

M-QAM M− Quadrature Amplitude Modulation

ML Maximum Likelihood

MLSE Maximum Likelyhood Sequence Estimation

MSC Multi-Subcarrier

MSE Mean Squared Error

MZM Mach-Zehnder Modulator

NFDM Nyquist Frequency Division Multiplexing

NGMI Normalized GMI

NLPN Non-Linear Phase Noise

NMSE Normalized Mean Square Error

NS Normalized Separation between reference subcarriers

P Pilots

PBC Polarization Beam Combiner

PBS Polarization Beam Splitter

PND Percentage of the Normalized Difference

PR Pilot Rate

QAM Quadrature Amplitude Modulation

QPSK Quadrature Phase Shift Keying

SBPS Staggered BPS

SC Single-carrier

SE Spectral Efficiency

SNR Signal to Noise Ratio

SP Spaced Pilots

SRC Single Reference Carrier

SSMF Standard Single Mode Fiber

TD-CDE Time Domain

VV Viterbi-Viterbi

WDM Wavelength-Division Multiplexing

Intentionally blank page.

List of Symbols

I in-phase component of a signal

L fiber length

N_{SC} number of subcarriers

Q quadrature component of a signal

R_{P} pilot rate

R_{MSC} symbol rate of each subcarrier

T_s symbol period

ΔT_{CD} inter-subcarrier temporal delay caused by chromatic dispersion

Δf the spectral width of a laser

β_2 group velocity dispersion parameter

$\hat{\phi}_{\mathrm{LO}}$ estimated laser phase noise generated at the receiver

$\hat{\phi}_{\mathrm{PN}}$ estimated phase noise

$\hat{\phi}_{\mathrm{TX}}$ estimated laser phase noise generated at the transmitter

ϕ_{LO} laser phase noise generated at the receiver

ϕ_{PN} phase noise

ϕ_{TX} laser phase noise generated at the transmitter

$\mathbf{M}$ number of unique symbols in a modulation format

Intentionally blank page.

Chapter 1

Introduction

1.1 Background

The massive growth in data traffic that has been characterizing this century is a consequence of the unquestionable value brought to us by the Internet. Considering that virtually every piece of data sent over the Internet is at some point transmitted through an optical link [1], it is easy to understand how any study related to the enhancement of optical systems is of utter importance. Furthermore, it should be noted that the need for higher transmission rates is particularly felt these recent times when we are more dependent than ever on the internet speed to perform our daily tasks remotely, with the lack thereof representing an obstacle to communication.

Throughout the world, more than two billion kilometers of optical fibers have been deployed [1], meaning that the secret behind improving the transfer rates of optical transmission systems, while aiming at cost-efficient short-medium term solutions, is to focus on the deployment of advanced optical transceivers. These advanced optical transceivers enable faster transmission rates with low power consumption and without the need to change the already laid fiber network.

Coherent detection allied with advanced Digital Signal Processors (DSPs) is globally considered to be the primary technology to increase the capacity of an optical transmission system [2, 3]. And DSPs are vital in coherent detection because they play an indispensable role in compensation, mitigation and exploitation of the existing impairments in an optical transmission system [4, 5], might they be associated with the propagation of the signal throughout the fiber or with the optical transceivers themselves.

However, as any engineer would expect, such good news never come alone. As much as coherent optical systems are made to sound good in the previous lines, they still present some challenges. The fiber impairments present an obstacle to the maximum achievable rates that modern fast hardware can provide. Thus, every effort and success in reducing their respective impact on the achievable data rates is of interest. Lately, there have been several studies manifesting the interest for Multi-Subcarrier (MSC) as opposed to single-carrier systems. This interest is explained by the fact that it has been experimentally demonstrated that MSC systems, with the help of advanced DSPs, can: i) improve the tolerance to both linear and nonlinear fiber impairments [6–8] and ii) reduce the complexity of optical transceivers [9]. These advantages of MSC systems translate into a more power-efficient system. In addition, MSC systems bring the opportunity to develop novel approaches for the compensation of optical system impairments,

with potential advantages over single-carrier systems, not only regarding their reduced complexity and energy efficiency, but also benefiting from an increased frequency resolution, thereby increasing the interest of advanced DSPs specifically designed for MSC systems. Examples of such MSC-specific approaches are: i) the mitigation of non-linear phase noise through the inter-subcarrier nonlinear noise correlation [10], ii) the design of pre-emphasis techniques that treat each subcarrier independently [11] and iii) the use of joint subcarrier processing for carrier phase estimation [12]. The latter being the topic of focus of the present dissertation.

While the vast research on the topic of MSC systems emphasizes very well its academic and research value, commercial companies have also demonstrated interest in this technology, evidencing its commercial value as well. Two exceptionally relevant companies in this context are Infinera and Ciena. Both these companies currently dedicate part of their portfolio to MSC systems and have several patents on the topic [13–17].

Now, changing the subject to the universe of research on the topic of optical fiber communication systems, there are several interesting advantages that make it quite accessible and appealing. One of the main reasons is that, unlike wireless communications, the transmission channel presents a very low deviation from theoretical models, which means that the effects of the signal during the transmission are known with relatively good accuracy. This property greatly facilitates the research on coherent optical systems, by enabling the development of highly accurate simulation models for optical fiber [18–20], which are able to provide results, yielding valid measurements and allowing the evaluation of DSP approaches, in a timely manner [21, 22]. Another important reason is that, with the emergence of DSP as well as with the tendency to bring most of the transmitter's and receiver's processing to the digital domain, every day the similarity between the simulations and the practical results is diminishing. With all this being said, it is unquestionably the best approach for a researcher that aims to develop new and disruptive approaches to DSP subsystems to learn his ways around a simulator of an optical transmission system, alongside with the gathering of skills to effectively program DSP algorithms and learn important metrics to properly measure and display data and the results.

1.2 Motivation and Objectives

The motivation behind this study arose from the recent interest in MSC systems, and the respective realization that there was an unaccounted impact associated with the performance decrease of Carrier Phase Estimation (CPE) mechanisms in these systems. In fact, this impact is so noticeable that it is the main limitation to the maximum number of subcarriers an MSC system can have [9]. This is problem is caused by the fact that, while there has been extensive research on the topic of phase noise estimation and compensation, most solutions are designed only for single-carrier systems, and, when applied to multi-subcarrier systems, these algorithms are generally applied without modification, each subcarrier individually. And, on that cue, the goal of this work is to make an in-depth analysis of the relation between the performance of CPE approaches and the number of subcarriers. Doing so will open a path to attempt to make the approaches compatible with a system with a higher number of subcarriers, removing the limitations associated with carrier phase tracking, thus allowing to take full advantage of

the great tolerance that these systems have to the fiber impairments and improving the performance of MSC systems. This will increase their already existent commercial value. In short, this dissertation aims to study the application and adaptation of common CPE algorithms to MSC systems.

Having introduced the topic of this dissertation, and the motivation that constitutes its foundation, now the respective objectives are summarized:

- Study coherent optical transmission systems and respective DSP components with emphasis on the MSC-specific requirements, to learn how to handle the simulator and be able to perform changes in the DSP;
- Measure quantitatively the impact of transitioning from a single-carrier to a multi-subcarrier system;
- Create, implement, validate and optimize CPE approaches that can increase the performance of MSC systems in comparison to the single-carrier ones.

1.3 Dissertation Structure

The structure of this dissertation was crafted to take the reader throughout the sequence of events that sum up the developed work, justifying each evolution and decision taken. The dissertation is divided into four main chapters, each with three to four sections. In the following lines, the structure of this document is summarized, attributing to each of the remaining chapters and their sections the due topics.

Chapter 2 is the chapter in which it is analyzed the state of the art in the area of this research, it represents the initial phase of the developed work, the gathering of knowledge required to initiate the research. Section 2.1 encompasses a revision of the general structure of coherent optical transceivers with a special emphasis on their DSP units, namely their MSC-specific constituents. Section 2.2 is devoted to the analysis of the Laser Phase Noise (LPN), the study of its origin, how to model it and several techniques to compensate for it. Section 2.3 has a similar purpose, but assesses Chromatic Dispersion (CD) instead of LPN.

Chapter 3 is the first chapter with practical results, it incorporates the study of a problem associated with the migration to a MSC system. Section 3.1 introduces the underlying algorithms used for two CPE methods of particular importance in the context of the dissertation. They are presented in this part rather than in Section 2.2 to emphasize the importance of understanding of the implementation of CPE methods, to enable the design of enhanced CPE versions specific for MSC systems. Section 3.2 introduces the simulation environment chosen for obtaining the practical results, as well as the default scenario considered. Section 3.3 is where the performance of CPE approaches is firstly assessed with respect to the change of the number of subcarriers in the system. Section 3.4 presents the same results as the previous section, but now with a non-null transmission length, which makes the performance susceptible to one of the most affecting impairments, the effect of CD.

Chapter 4 represents the first step towards MSC-specific CPE approaches, making use of the information regarding LPN estimates in all subcarriers. Section 4.1 describes how the implementation of CPE algorithms seen in Section 3.1 can possibly be adapted to

improve its performance. In Sections 4.2 and 4.3 the respective performance is assessed, in scenarios with and without the effect of CD, similarly to Sections 3.3 and 3.4.

Chapter 5 is the one in which the main novel contributions of this dissertation are detailed, including a novel CPE technique. Section 5.1 describes the principles behind this novel method and how it is employed. Section 5.2 evaluates how the performance of this algorithm can be optimized, and then assesses its performance against the best results attained with earlier approaches. Section 5.3 evaluates the possibility of performing digital monitoring, capability brought by the details of the implementation of the novel method.

Chapter 6 is the last chapter. In it, an overview of the entire results is made, conclusions are taken and, afterwards, future work is discussed.

1.4 Contributions

The work developed in the scope of this dissertation has given fruit to two main contributions:

- The filling of a provisional patent application, covering the novel method completely born from the work evolution and studies performed in the thesis, presented in Chapter 5;
- Preparation of a paper entitled "Digital Monitoring and Mitigation of Laser Phase Noise Using a Dual-Reference Subcarrier Approach" to be submitted to the IEEE/OSA Journal of Lightwave Technology.

Chapter 2

State of the Art

2.1 Coherent Optical Transmission Systems

Studies on coherent optical fiber communications date back to the 1980s [23]. The appeal on these systems, as opposed to legacy Intensity-Modulation and Direct-Detection (IM·DD) systems, is motivated by their greater sensitivity at the receiver that allows longer transmission distances. The increased sensitivity at the receiver is achieved by mixing the received signal with a Local Oscillator (LO), which, by increasing the received optical signal power after the photo-detection, allows for a decrease in the influence of thermal noise at the receiver. Curiously enough, the biggest advantage nowadays associated with coherent systems (their capacity to implement spectrally efficient modulation formats) was not the scientific drive at the time.

Although coherent systems showed great potential, it was not until the uprising of Digital Signal Processors (DSPs) that they became widely used, as it enabled carrier recovery and compensating for the fiber transmission impairments that, for some years, had made IM·DD schemes the most efficient choice, since IM·DD receivers were not sensitive to the carrier phase nor to the polarization of the transmitted signal. Adding to this, the emergence of Erbium-Doped Fiber Amplifiers (EDFAs) and of Wavelength-Division Multiplexing (WDM) technology, allowed the increase in both the limited transmission distances and the low throughput associated with direct detection systems.

Nowadays, due to the increasing demand for higher capacity in the networks, the study of coherent systems with the promise of higher transmission rates has been revived, with the help of faster Digital to Analog Converters (DACs) and Analog to Digital Converters (ADCs), as well as the faculty to implement Application Specific Integrated Circuits (ASICs). It is important to highlight that, in coherent systems, it is possible to completely retrieve the analog signals received at the optical receiver to the digital domain with negligible loss of information, which means that all signal equalization and compensation can be done in the digital domain, thus relaxing the requirements of the optical components, because most non-idealities can be overcome with the usage of DSP. With all this in mind, this section will go through all the fundamental blocks that build up a coherent optical transmission system. Firstly, in Subsection 2.1.1 a look at the typical structure of a coherent optical transmitter will be taken, followed by an overview of the main DSP functions, in Subsection 2.1.2. Afterwards, and to conclude, the same will be done for the optical receiver, in subsections 2.1.3 and 2.1.4, respectively.

2.1.1 Architecture of Coherent Optical Transmitters

In Figure 2.1 is represented the typical architecture of a coherent optical transmitter, based on a dual-polarization configuration, a usual approach to double the Spectral Efficiency (SE). The transmitter's DSP takes as an input two data streams, containing only information bits to be transmitted in the $x-$ and $y-$ polarizations, and, after processing them, outputs two pairs of I and Q digital signals, one for each polarization. Each of the four signals is input into a DAC, and the output analog electrical signals are ready to modulate the carrier, in the two In-phase and Quadrature Modulators (IQMs). Each of the two IQMs takes one of the $x-$ or $y-$ polarizations, obtained from the transmitter's laser using a Polarization Beam Splitter (PBS). The outputs of the IQMs are optical signals modulated in-phase and quadrature, one in each of the two orthogonal polarizations. Finally, these two optical signals, $E_{s,x}$ and $E_{s,y}$, are merged together using a Polarization Beam Combiner (PBC) and the complete optical signal, E_s, is ready to be transmitted.

In the next few paragraphs, a brief description of each building block will be presented.

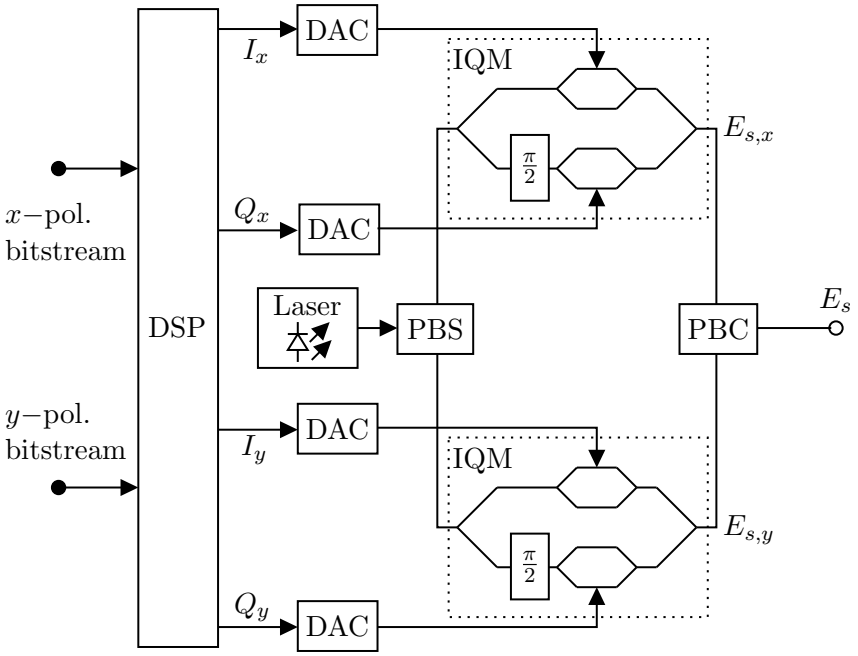

Figure 2.1: Common Architecture of a Coherent Optical Transmitter.

DSP

The transmitter DSP is responsible for the pre-processing of the signals to transmit, its primary task is to implement signal modulation in the complex plane, and afterwards, to shape the pulses in an appropriate format. Additional pre-processing can be done, namely, signal pre-distortion, to compensate fiber impairments right in the transmitter side and also the addition of redundancy to the transmitted bits, implementing Forward Error Correction (FEC) encoding. Considering that signal processing is the scope of this thesis, a more detailed description of this block will be given in Subsection 2.1.2.

DACs

DACs have several important aspects that must be taken into consideration when evaluating their adequateness to the system at issue. Two off the most important aspects to be taken into account when designing a DAC are: i) bit resolution, which if not high enough, can cause significant quantization noise; and ii) sampling rate, which, following Nyquist's sampling theorem [24], must be at least twice the baudrate of the system for penalty-free communication. Concerning the latter, it is important to bear in mind that in practice it is very rare to find optical transceivers in the market that actually follow this rule. In order to reduce the cost and/or exploit the maximum symbol-rate, it is very common to find optical transceivers with DACs operating at 1.5 samples per symbol, because the associated penalty is very small. Another important aspect to have in consideration is the dynamic range of the ADC, to make sure there is no signal clipping.

Laser

The Laser is responsible for the generation of a Continuous Wave (CW) optical carrier. Lasers are required as opposed to simple Light Emitting Diodes (LEDs) because of their spectral properties. While LEDs have very wide spectra, in the order of the tenths of nanometers [24], lasers can achieve much narrower spectra, common lasers having under 3 nm spectrum. Furthermore, coherent communications, demand high-performance lasers. Among the most used laser sources are single-mode Distributed Feedback (DFB) lasers and External Cavity Lasers (ECLs), achieving extremely thin spectra. In fact, the width of the optical source, and its deviation from the ideal null width are the cause of the problem that this dissertation aims to solve. An in-depth analysis of the laser's non-idealities will be given in Section 2.2.

In-Phase and Quadrature Modulators

IQMs, as the name implies, are the elements of the transmitter that allow the modulation of both the I and the Q signals, given an optical single-polarization signal, thus performing electrical to optical up-conversion. The typical configuration of IQMs is shown in Figure 2.2 [23], where it is possible to identify two Mach-Zehnder Modulators (MZMs) and one phase shifter. MZMs have a basic functioning principle based on the fact that an electrical field applied to a material can change its refractive index, thereby being able to apply a phase change on the propagating signal. The optical signal at the input, E_{in} is split in two branches, with a 3 dB polarization-maintaining splitter. Then, one of the branches is subject to an electrical field that will impose an optical phase shift of $\pi/2$, by applying the voltage $-V_{\pi/2}$, thus obtaining the quadrature signal to be modulated. Now we have two optical signals, in-phase and quadrature, ready to be modulated. Each of the two goes through an MZM, in a push-pull configuration, using as a driving signal the electric analog signals generated in the DACs, represented in the figure as u_I and u_Q. The two branches are now coupled again, post-modulation, achieving an IQ modulated optical signal, E_{out}.

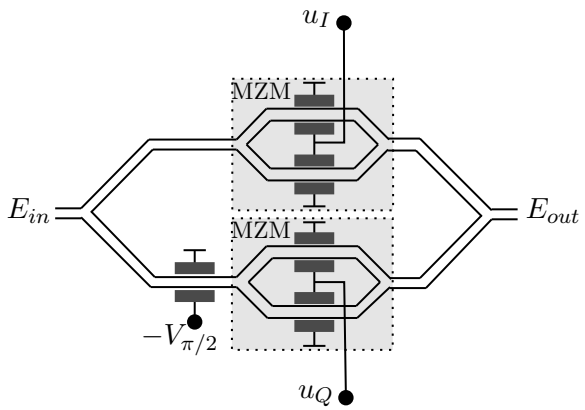

Figure 2.2: In-phase and Quadrature Modulator (IQM) scheme.

2.1.2 Transmitter's Digital Signal Processor

Up until now, the description of the transmitter has been independent of whether we are dealing with a Single-carrier (SC) or a Multi-Subcarrier (MSC) system, which proves how it may be easy to change to the latter without any modification on the basic design of the network. However, as it can be observed in Figure 2.3, it is in the DSPs that the differences are seen, namely on the coexistence of several subcarriers and of the grayed out blocks, which are the MSC-specific ones. Note that, in addition to the blocks displayed in the DSP figure, some systems apply pre-distortion to the signal, by applying the inverse channel response of the fiber, and by doing so, throughout propagation, the fiber impairments are canceled out. However, these techniques can equally be done in the receiver DSPs, and that is the model that will be considered in the context of the present work. Furthermore, in the Figure's FEC encoding is considered to have been performed before the subcarrier demultiplexing, but it could also be performed independently per subcarrier, however that is not going to be studied in the scope of this dissertation.

The next paragraphs of this subsection are devoted to summarizing the blocks that constitute the common transmitter's DSP of an MSC system.

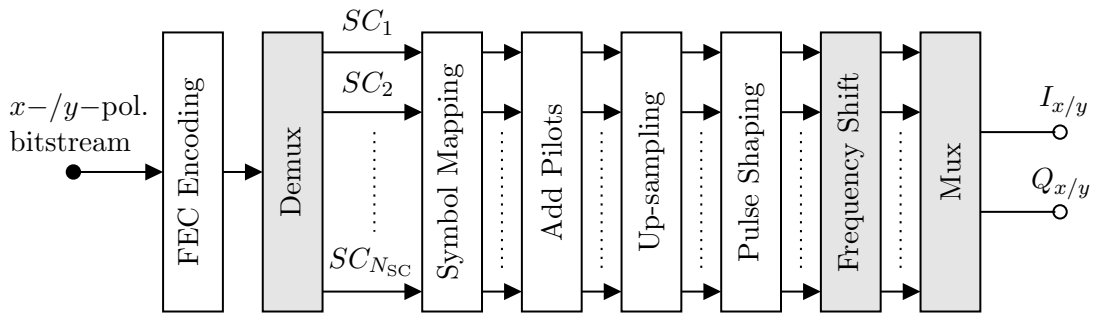

Figure 2.3: Scheme of a Transmitter Digital Signal Processor of an MSC System.

Forward Error Correction Encoding

FEC encoding consists of the addition of purposely redundant bits to the original bitstream, to add tolerance to errors that might have occurred during the signal detection, caused by noise or any other impairment. Typical FEC rates for modern coherent optical transceivers are in the order of 20%, meaning that for every 100 bits in the original bitstream, 20 additional bits will be inserted. This relatively large overhead associated with advanced soft-decoding mechanisms has proven to be able to yield a net coding gain of up to 12 dB [25], allowing to meet the typical transmission systems requirements of a post-FEC Bit Error Rate (BER) of the order of 10^{-15} with a considerably high FEC threshold and lower power consumption.

Demultiplexing

The demultiplexing block divides the data bitstream into N_{SC} bitstreams. This division of bits per subcarrier must take into account the number of pilot symbols to be added to that same subcarrier. The need for insertion of pilot symbols will be addressed further ahead, but, since they take up space of regular symbols, this block needs to assure that the bitstream splitting is done accounting for the space needed for their addition.

Symbol Mapping

The symbol mapping, as the name suggests, is where the bits are transformed into symbols, following a certain modulation format. Symbol mapping is essential in a transmission system, because, while in binary modulation formats we are limited to an SE of 1 bit/s/Hz/polarization, multi-level modulation formats enable an increase in the SE by a factor of m_b, which corresponds to the number of bits sent per symbol, which, given the number of unique symbols in a modulation format, M, is given by $\log_2(\mathrm{M})$.

Benefiting from the in-phase and quadrature modulation capabilities of the optical transmitter described in Section 2.1.1, several modulation formats can be utilized for coherent optical communications. In this regard, M− Phase Shift Keying (M-PSK) and M− Quadrature Amplitude Modulation (M-QAM) are among the most utilized modulation formats, with a prevalence of the latter, thanks to its improved Euclidean distance. Multi-level modulation formats can have their symbols represented on the complex plane, forming a so-called signal constellation. M-PSK consists of a constant modulus signal in which the information is modulated only on the phase, with all symbols being equally spaced over a circumference on the complex plane whose radius corresponds to the constant modulus of the signal. M-QAM consists of a signal in which, as the name implies, the symbols are modulated in both in-phase and quadrature components separately, using discrete amplitude levels, forming a constellation characterized by a grid-like aspect. Note that, for M=4, both M-PSK and M-QAM converge to a Quadrature Phase Shift Keying (QPSK) constellation.

Considering that M-QAM is not only the most common high order modulation format but it is also the one used for simulations in the present work, a more detailed description is now given.

Each symbol from the constellation can be represented as:

$$s_k = s_k^I + i s_k^Q, k \in [1, 2, ..., \mathrm{M}] \tag{2.1}$$

where s_k^I and s_k^Q correspond to the I and Q components. To each s_k a combination of m_b bits is attributed. Figure 2.4 shows an example of a 64-QAM constellation on the complex plane, with all the s_k and the respective bits. The choice of the m_b bits for each symbol is typically not arbitrary, following a Gray coding strategy, which means that any two adjacent symbols in the constellation must have a unitary Hamming distance on the respective bit sequence, assuring that a symbol error resulting in the misevaluation of a symbol by an adjacent symbol results only in one-bit error out of the corresponding m_b bits.

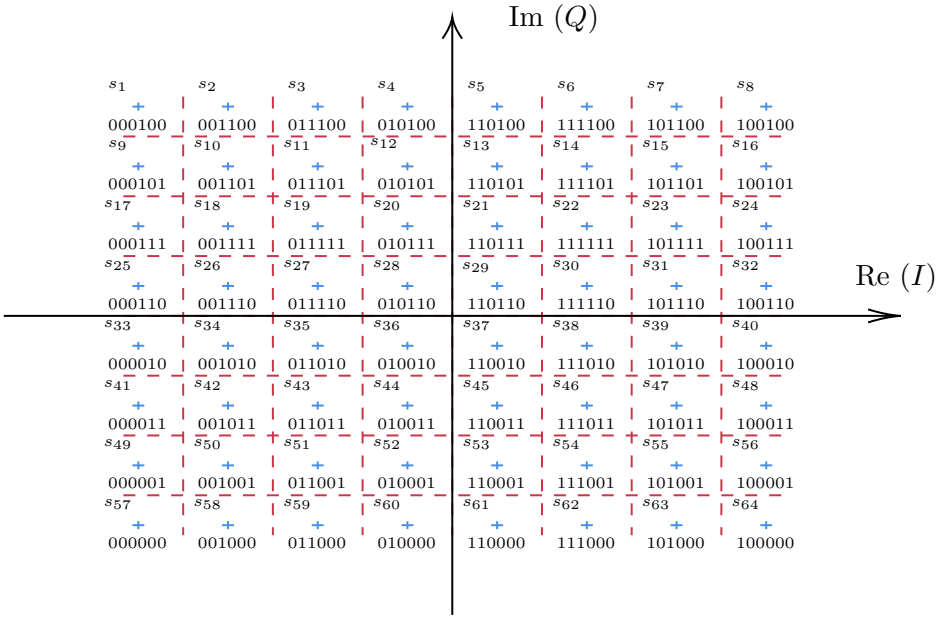

Figure 2.4: 64-QAM constellation with Gray coding.

Pilots Addition

After the conversion to symbols on the complex plane, pilot symbols are inserted to aid on the convergence of specific DSP subsystems. Pilots are an important part of this dissertation and consequently will be thoroughly analyzed in Section 2.2.

Up-sampling

At this point, each subcarrier's symbol sequence is complete, and there is one digital value per each symbol. Now, to prepare the subcarrier for the pulse shaper, an up-sampling operation is required. Up-sampling is performed by inserting $N-1$ zeros after each symbol, where N is the number of samples required per symbol. In SC systems, N is usually 2, to satisfy Nyquist's sampling theorem. However, in MSC systems, that value is multiplied by N_{SC}, accounting for the fact that the subcarriers will eventually be multiplexed together, and the overall signal will still have to obey the sampling theorem.

Pulse Shaping

Pulse shaping is one of the most important parts of the Transmitter's DSP, as it allows to control the signal bandwidth and the Inter-Symbol Interference (ISI).

Unlike a basic rectangular pulse, a spectral efficient pulse shaping must have a finite bandwidth, so that it is possible to accommodate the maximum number of signals in a given allocated spectral band without having to worry about signals overlapping or getting distorted by the filtering of the signal on the allocated band. Another important requirement of the pulse shape is to assure there is no ISI, which means that, in a sampling moment only the respective symbol can have a non-null amplitude.

Having these two requirements met, the typically used pulse shape is based on a raised-cosine pulse shaping filter, whose time and frequency formulations are presented below, in expressions (2.2) and (2.3), respectively, where β represents the roll-off factor and can take any value in the interval $[0, 1]$.

$$h_{RC}(t) = \begin{cases} \frac{\pi}{4T_s}\text{sinc}\left(\frac{1}{2\beta}\right), & \text{if } t = \pm\frac{T_s}{2\beta} \\ \frac{1}{T_s}\text{sinc}\left(\frac{t}{T_s}\right)\frac{\cos\left(\frac{\pi\beta t}{T_s}\right)}{1-\left(\frac{2\beta t}{T_s}\right)^2}, & \text{otherwise} \end{cases} \tag{2.2}$$

$$H_{RC}(f) = \begin{cases} 1, & \text{if } 0 \leq |f| \leq \frac{1-\beta}{2T_s} \\ \frac{1}{2}\left[1+\cos\left[\frac{\pi T_s}{\beta}\left(f-\frac{1-\beta}{2T_s}\right)\right]\right], & \text{if } \frac{1-\beta}{2T_s} \leq |f| \leq \frac{1+\beta}{2T_s} \\ 0, & \text{otherwise} \end{cases} \tag{2.3}$$

Firstly, concerning expression (2.2), we can see how h_{RC} is null in multiples of T_s other than zero, as required to remove ISI. Secondly, concerning expression (2.3), we can see how the pulse has a finite bandwidth that, depending on the value of the β parameter, can be as low as $1/2T_s$.

While the raised-cosine pulse shaping filter fills both requirements, only the bandwidth one is strictly needed for the signal transmission, the ISI requirement is only really required when sampling the signal at the receiver. So, given the fact that a filtering operation will be needed in the receiver, the best pulse shape at the transmitter is actually the root raised-cosine, which, albeit not removing ISI at the transmitter, maintains the same bandwidth. At the receiver, a matched filter will be applied, equally, a root raised-cosine filter and, consequently, the filtering is half done in the transmitter and half in the receiver, achieving a raised-cosine filter at the receiver, with the ISI requirement fulfilled.

Frequency Shift

This block is one of the three that is specific to Multicarrier systems. Each subcarrier, k, will have to be shifted to its corresponding baseband frequency, f_k, to form the complete SC equivalent baseband signal. This scheme is usually called Nyquist Frequency Division Multiplexing (NFDM) [26]. The frequency of each subcarrier is given

by Equation (2.4). It is really important to notice that this implementation of NFDM, and consequently the frequency shifts, is completely applied in the digital domain, representing no differences in the physical architecture of the transmitter's DSP.

$$f_k = \left(k - \frac{N_{\text{SC}} + 1}{2}\right) \frac{1+\beta}{2T_s} \tag{2.4}$$

Multiplexing

With all the subcarriers filtered and properly aligned in the frequency domain, multiplexing them is as simple as adding all the digital signals together, and, from the complex result, the real and imaginary components correspond respectively to the $I_{x/y}$ and $Q_{x/y}$ components.

With the objective of making it clear that the use of subcarrier multiplexing does not represent an additional usage of spectrum, let us look into Figure 2.5, where we can see the spectrum of a single-carrier system and one of an MSC system, both systems having the same overall transmission rate. An equal spectral occupancy can be observed.

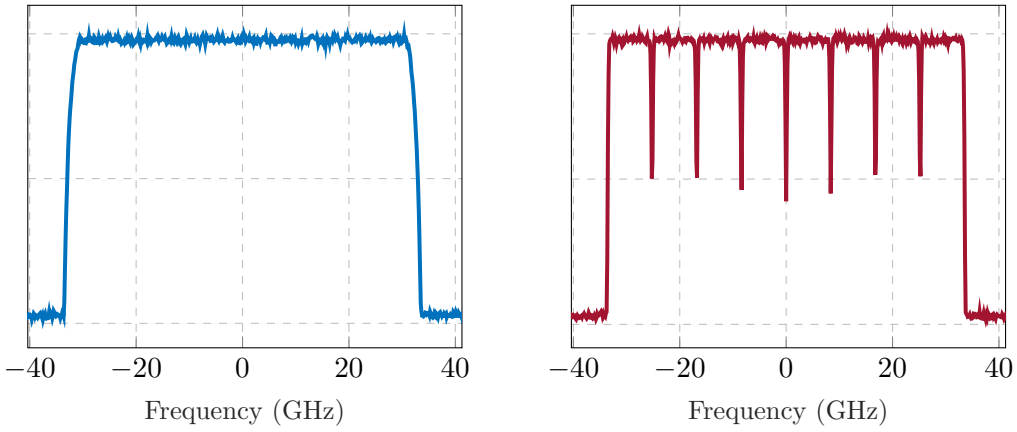

Figure 2.5: Spectrum occupancy of equivalent single-carrier (a), and MSC (N_{SC}=8) (b), systems.

2.1.3 Architecture of Coherent Optical Receivers

The typical architecture of a polarization diversity coherent optical receiver is shown in Figure 2.6, which matches the double polarization transmitter described in Subsection 2.1.1. Looking into the figure of the receiver's architecture, it can be seen that, as the optical signal, E_s, is received, it is split in a PBS into the $x-$ and $y-$ polarizations. In parallel, the local oscillator is similarly split and then both polarizations are separately processed, mixing the received optical signal, $E_{s,x/y}$, with the local oscillator's, $E_{lo,x/y}$, to perform an intradyne down-conversion in a 90° Optical Hybrid. Note that the down-conversion is called intradyne and not homodyne because it cannot be considered that the signal is brought to a zero frequency, but rather to a near-zero frequency, which is because the LO is not locked to the transmitter's laser, considering the difficulty of

implementation of an optical phase-locked loop at such high frequencies. The solution is then to leave the compensation to the digital side, as will be seen in Subsection 2.1.4. The output signals of the optical hybrid are then fed into balanced photodetectors to finally retrieve the I and Q components of each polarization. These four signals can then be converted to the digital domain in the ADCs and are fed into the receiver's DSP were the original $x-/y-$ polarization bitstreams are recovered.

Let us now analyze each main building block separately.

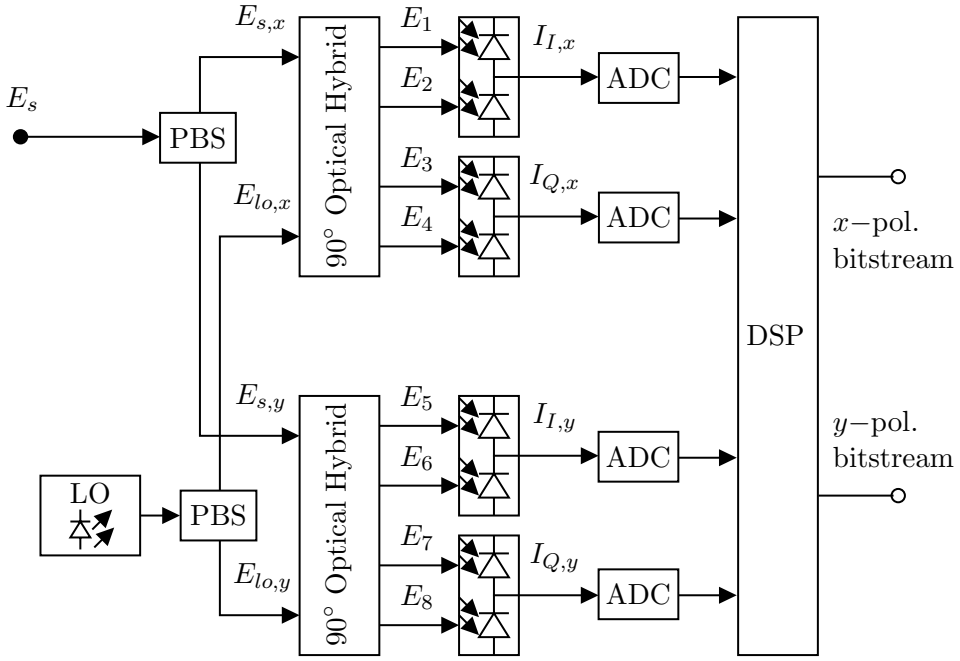

Figure 2.6: Common Architecture of a Coherent Optical Receiver.

Local Oscillator

The LO is a CW laser, like the one in the transmitter. It is fundamental because it is the optical signal used to convert the received signal to baseband, in order to be able to be sampled. The ideal complex electrical field of the LO is given by:

$$E_{lo}(t) = A_{lo} \exp\left(-i(\omega_{lo} t + \theta_0)\right), \tag{2.5}$$

where A_{lo} is LO's constant complex amplitude, w_{lo} the angular frequency and θ_0 the initial phase. As mentioned earlier, the laser is hereby considered as an ideal light source, and in Section 2.2 we will get into the details of lasers' non-idealities.

90° Optical Hybrid

To better understand the operation performed by the 90° Optical Hybrid, let's look at Figure 2.7, where a scheme of such equipment can be seen. It is composed of two polarization-maintaining splitters, one phase modulator performing a shift of $\pi/2$ and two 3 dB couplers. Considering the electrical complex field of the received signal, E_s, as:

$$E_s(t) = A_s \exp\left(-i(\omega_s t + \theta_s(t))\right), \tag{2.6}$$

where A_s is the complex amplitude, w_s the angular frequency and θ_s the phase, we can describe the four outputs of the 90° Optical Hybrid as a function of $E_{s,x/y}$ and $E_{lo,x/y}$ in the following manner:

$$E_{1/5} = \frac{1}{2}\left(E_{s,x/y} + E_{lo,x/y}\right) \tag{2.7}$$

$$E_{2/6} = \frac{1}{2}\left(E_{s,x/y} - E_{lo,x/y}\right) \tag{2.8}$$

$$E_{3/7} = \frac{1}{2}\left(E_{s,x/y} - iE_{lo,x/y}\right) \tag{2.9}$$

$$E_{4/8} = \frac{1}{2}\left(E_{s,x/y} + iE_{lo,x/y}\right) \tag{2.10}$$

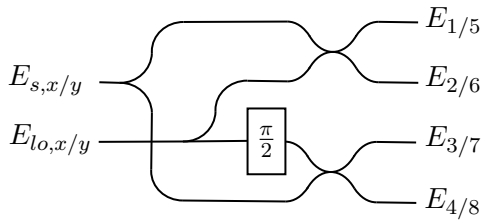

Figure 2.7: 90° Optical Hybrid scheme.

Balanced Photodetectors

The balanced photodetectors are responsible for the optical to electrical conversion of the I and Q components of each polarization. A balanced scheme is used to improve the receivers sensitivity: by performing differential reception, the constant component of the signals can be removed, thus being able to only amplify the information-carrying part of the signals. Considering an ideal reception, these are the obtained photocurrents:

$$I_{I,x/y}(t) = R\sqrt{P_{s,x/y}(t)P_{lo,x/y}}\cos\left(\theta_{s,x/y}(t)\right) \tag{2.11}$$

$$I_{Q,x/y}(t) = R\sqrt{P_{s,x/y}(t)P_{lo,x/y}}\sin\left(\theta_{s,x/y}(t)\right) \tag{2.12}$$

where R corresponds to the responsivity of each photodiode, P_s and P_{lo} to the respective signals' power and $\theta_{s,x/y}$ to the modulated phase in the received signal in each polarization.

ADCs

ADCs are responsible for converting the set of analog electrical signals into the digital domain. They have similar important parameters to take into consideration to the DACs, addressed in Subsection 2.1.1.

Receiver's DSP

Having now completely recovered the digital in-phase and quadrature signals generated for each polarization in the transmitter, in the receiver DSP they are treated to minimize the transmission error rate. The digital operations performed on the received signals are analyzed in the next subsection.

2.1.4 Receiver's Digital Signal Processor

In this subsection, an overview is made of the several blocks that constitute a receiver's DSP of an MSC system, whose MSC-specific blocks are grayed out. Compared with the corresponding transmitter-side DSP, normally the DSP subsystem is more intensive at the receiver, owing to the fact that many impairments are stochastic, and therefore cannot be predicted and compensated for at the transmitter. In Figure 2.8 we can see the main blocks in a possible configuration.

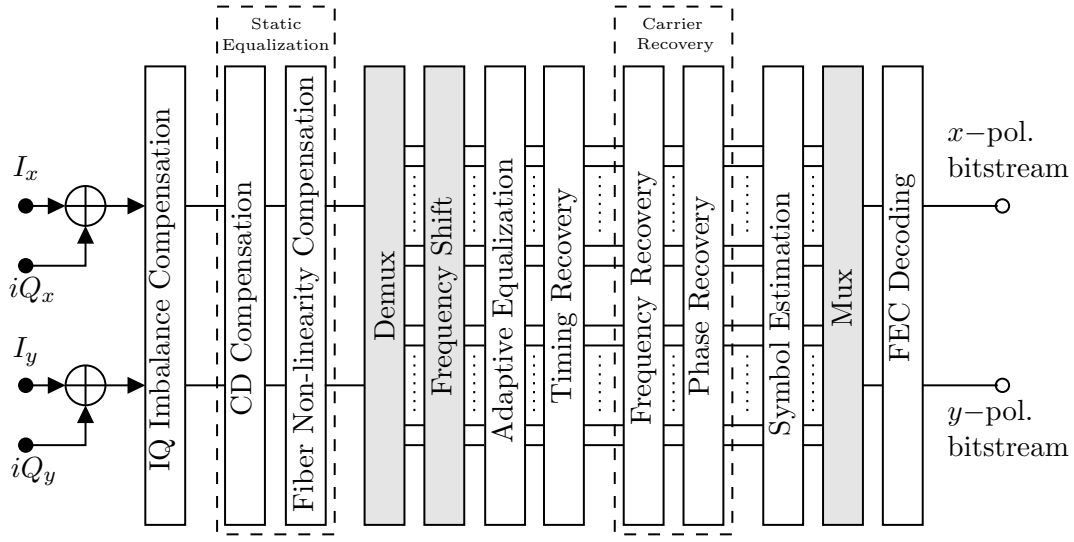

Figure 2.8: Common blocks of an MSC System Receiver DSP, in a possible configuration.

IQ Alignment and Imbalance Compensation

This block is required because, due to different path lengths of the I and Q signals of both polarizations, there can occur a temporal misalignment between the four signals, usually called timing skew, which should be compensated before anything else. To this purpose, a timing de-skew algorithm is generally applied, as seen in [27]. Having now all the four signals aligned, it is still required to compensate for any imbalance between balanced photodetectors that may have caused an orthogonalization problem. To compensate for this imperfection, techniques based on Blind Adaptive Source Separation (BASS) method can be applied, as proposed in [28].

Chromatic Dispersion Compensation

Chromatic Dispersion (CD) plays a key role in the subject of this thesis, consequently, its compensation demands an in-depth analysis, which will be performed in

Subsection 2.3.

Fiber Non-linearities Compensation

While MSC systems have proved to be more tolerant to fiber non-linearities [29–31], compensation can still be applied to increase the system's transmission reach [31].

As seen in Figure 2.8, this is one of the two blocks included in the static equalization. Its designation is due to the time-invariant properties of the non-linear fiber impairments. Common compensation techniques are based on Digital Back Propagation (DBP) which, given the received signal, involves inverting the effects caused by propagation on the digital domain [32, 33]. The main drawbacks of these techniques are their high computational requirements, thus, extensive studies are being led to reduce the complexity needed to perform the DBP technique [34, 35].

Demultiplexing and Frequency Shift

On these three blocks, the signal is now split into the various subcarriers, with the knowledge of each subcarriers' central frequency (given by expression (2.4)). The matched filter, a root raised-cosine shaping filter, is now applied to simultaneously filter the spectral components of the adjacent subcarriers and to improve the Signal to Noise Ratio (SNR). Afterwards, a frequency shift is employed to move all subcarriers to baseband.

Adaptive Equalization

Adaptive equalization is performed, in each subcarrier independently to complement the static equalization performed, which can be both due to under- or over-compensation in the previous static stages.

On this stage, and only in the scenarios with dual polarization, it is also simultaneously done the polarization demultiplexing.

The two most common types of adaptive equalizers utilized in coherent optical transceivers are based on Least Mean Square (LMS) and on Constant Modulus Algorithms (CMAs) [36]. The latter provides the advantage of being phase-insensitive, therefore enabling the realization of adaptive equalization prior to carrier recovery. However, the standard CMA is more adapted to constant module constellations, thus, for M-QAM modulation formats, modified CMA techniques are employed [37].

Timing Recovery

Timing recovery, also known as clock recovery, is intended to retrieve the transmitter's clock, to remove jitter associated with the sampling instants on both the phase and frequency shifts between the clocks of the transmitter and receiver. This is an important aspect to correct, since the absence of ISI associated with the raised-cosine pulse shape is only assured if the sampling instant is duly aligned. Timing recovery is divided into two phases, a primary phase, where the time deviation is estimated, and a secondary one, where the signal is equalized to match the ideal sampling moment. Among a plethora of algorithms, the Gardner timing error detector is one of the most commonly employed methods in coherent optical transmission systems [38, 39].

Frequency Recovery

Frequency offset recovery is the first stage of carrier recovery. The block is responsible to measure the prevailing offset from the zero frequency, a consequence of this receiver being an intradyne receiver as opposed to a homodyne receiver. For M-QAM formats, typical approaches are algorithms based on blind frequency search [40], which are based on testing a range of test frequencies and find the one that minimizes a determined cost function. Other approaches are feedforward algorithms such as [41, 42] and frequency-domain tone observation [43, 44].

Phase Recovery

The second block of the Carrier Recovery is Carrier Phase Recovery (CPR) which, being the main topic of the dissertation, has a devoted Subsection, 2.2.

Symbol Estimation

Albeit sounding like a presumably simple procedure, symbol estimation can be explored up to a relatively complex degree. For instance, acknowledging the existence of any residual memory of the channel, Maximum Likelyhood Sequence Estimation (MLSE) approaches can be employed. Given a block of symbols with noise, this technique tests several possible combinations and outputs the symbol sequence that results in a minor error [45]. Other approaches involve a neural network, to estimate non-linear classifiers improving the performance of symbol estimation in systems with non-linear effects [46]. However, even if complex approaches to symbol estimation mechanisms can be used, in Additive White Gaussian Noise (AWGN) systems the optimal solution is based on the Euclidean distance, and this is the solution elected in most commercial systems. This symbol estimation is performed in a rather intuitive manner. Given a timed and equalized signal, a stream of symbols, estimating each symbol consists simply of translating a received symbol to its nearest corresponding symbol on the fixed constellation, the Euclidean distance is measured on the complex plane after having the constellation normalized to the mean power of the received signal. The final step of symbol estimation consists of transforming the symbol into its corresponding bit sequence. Note that, at this stage, pilot symbols are disregarded, if they have not been removed in the previous block.

Multiplexing and Forward Error Correction Decoding

At this stage, several bitstreams have been retrieved, one bitstream per carrier for each polarization. All there is left to do is to combine back the bitstreams in the proper order and, after that, perform FEC decoding. This, once again, assumes the usage of joint FEC decoding, which is not a requirement in MSC systems, as mentioned in Subsection 2.1.2.

2.2 Laser Phase Noise: Modeling and Compensation

When described in the previous section, a laser's electrical complex field was presented in its ideal form, in expression (2.5). However, real lasers have an electrical

complex field that is better described by expression (2.13).

$$E_l(t) = A_l\sqrt{1+y(t)}\exp\left(-i(\omega_l t + \theta_0 + \theta_l(t))\right), \tag{2.13}$$

where y and θ_l represent the intensity and phase fluctuations that real lasers present. Laser Phase Noise (LPN) is the result of the sum of these phase fluctuations on the transmitter's laser and the LO.

Unfortunately, these laser phase fluctuations do not constitute a negligible deviation from the ideal lasers, they represent a big constrain on information transmission, concerning that, as thoroughly explored in Section 2.1, the carrier's phase is used to send information and, consequently, changes on the expected carrier phase distort the sent information. However, they always exist in real systems, and thus the concept of Laser Line Width (LLW) was created. This name is related to the width of the optical spectrum of the laser being evaluated (more precisely, the full width at half-maximum power).

A smaller LLW indicates a respectively narrower spectrum, which leads to fewer phase fluctuations. Ideally, LLW would be zero. LLW is consequently seen as a measure of how good a laser is. Typical values for LLW in coherent optical transmission systems are in the 100 kHz to 10 MHz range [23]. It is with this range in mind that the simulations will be analyzed in the following chapters.

2.2.1 The Wiener Phase Noise Model

Having acknowledged its existence, the first step towards being able to compensate the phenomena is to be able to understand its nature and behavior. Laser Phase Noise (LPN) can be modeled as a Wiener process, formulated by the following expression [47]:

$$\phi_{\mathrm{PN}}(k) = \sum_{i=-\infty}^{k} f_i, \tag{2.14}$$

where f_i represents an independent and identically distributed Gaussian variable with a zero mean and whose variance, σ_f^2, is given by:

$$\sigma_f^2 = 2\pi(\Delta f \times T_s), \tag{2.15}$$

where T_s is the period of a symbol and Δf is directly connected to the above-mentioned LLW. It represents the contributions of the LLW of both the transmitter's laser and the LO. We can consider the addition of both lasers' LPN as a single total LPN only because of the mathematical properties of a Wiener process, which assure that the sum of two independent Wiener processes also corresponds to a Wiener process, whose variance is the sum of the variance of the two originating Wiener processes. From a physical standpoint, this combined LLW approach also implicitly requires that the two lasers are co-located, which is not typically the case. Nevertheless, this issue will be revisited later in this thesis, when addressing the impact of CD in such scenarios.

It shall be noted that the relation of T_s with the variance of the LPN is very intuitive, considering that a larger symbol period is more likely to imply a larger variation of the LPN. This has an important relation with the analysis done in this work.

Looking at Figure 2.9, two distinct examples of the behavior of LPN can be seen, where its arbitrary and cumulative nature is well visible.

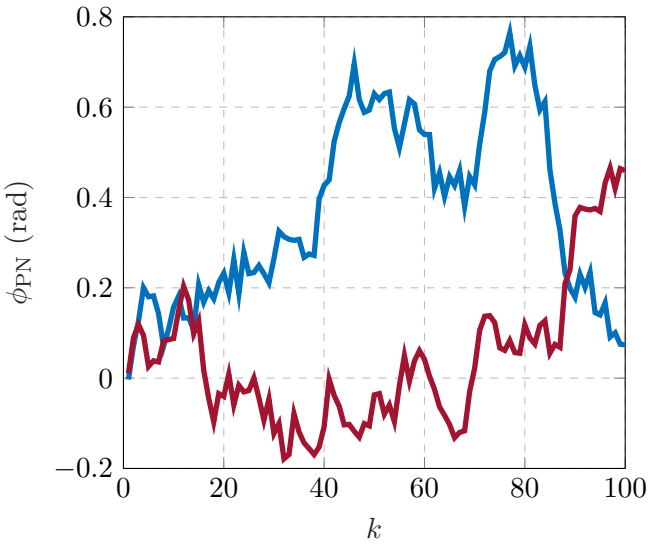

Figure 2.9: Two different instances of LPN.

A typical coherent transmission system demands tracking and compensation of the LPN, because this noise translates directly to a rotation of the constellation, and without it, the transmitted symbols become indistinguishable, as it can be observed in Figure 2.10.

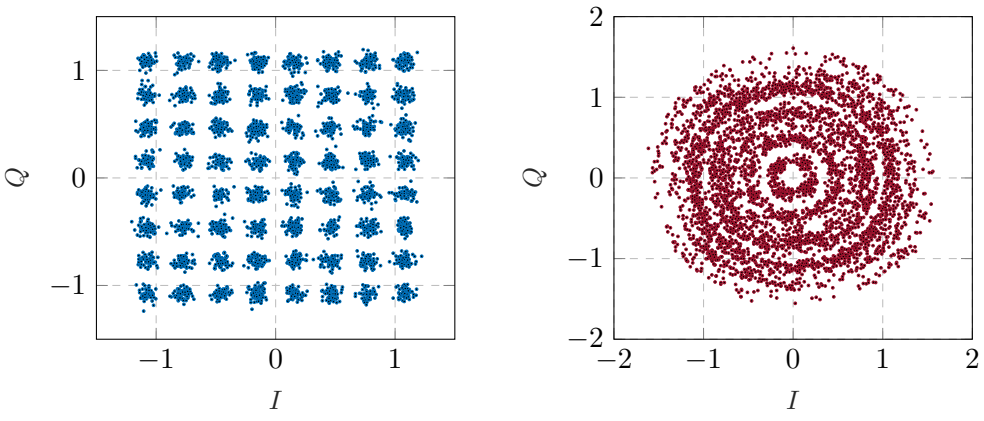

Figure 2.10: 64-QAM constellation without (a) and with (b) the impact of LPN, for Δf=100 kHz and $1/T_s$=64 GHz.

2.2.2 Carrier Phase Estimation and Compensation

Digital compensation of LPN takes advantage of its known properties, namely the fact that it is a cumulative process, to estimate its evolution and properly correct it. Algorithms that aim to correct LPN are called Carrier Phase Estimation (CPE) algorithms. While there are several different implementations, which will be described in

the paragraphs below, they all have the same working principle. They receive a signal, S_{rx}, with a strong distorting effect of phase noise, ϕ_{PN}, and build an estimate of it, $\hat{\phi}_{\mathrm{PN}}$. Upon building this estimate, the phase noise is corrected simply applying to the complex received signal a symmetric phase rotation:

$$S_{rx}(k) = S_{rx}(k) \times \exp(-i\hat{\phi}_{\mathrm{PN}}(k)) \tag{2.16}$$

One of the first widely used Carrier Phase Estimation (CPE) algorithms, famous for its application in QPSK systems, was the Viterbi-Viterbi (VV) algorithm [48]. In it, by raising each symbol to the fourth power, the symbols' original phase is canceled out and the phase that is left corresponds to four times the phase noise affecting that same symbol at reception. By dividing this phase by four, we get the phase noise estimate at that symbol, making this a genius and simple approach to estimate LPN. This method can easily be scaled to any M-PSK system, by switching the fourth power by the M-th power, with the only problem being the lower LPN tolerance, considering that the highest phase noise amplitude it can properly correct is half the phase between two symbols in the constellation, π/M. However, VV is not directly applicable to M-QAM constellations, due to the lack of phase equidistance in such constellations, thus not being able to blindly perform a constellation rotation that removes the dependence to the phase of the symbol transmitted. While modifications for M-QAM systems have been studied and presented [49], the performance is still limited for higher constellation orders.

Aiming at increasing the LPN tolerance for M-QAM formats, another CPE is proposed in [47]. It is called Blind Phase Search (BPS) and it gets its name from the fact that it can extract the phase from the received signal blindly, meaning that there is no need to add overhead to the received signal in order to estimate the signal phase deviation. This CPE algorithm plays an important role in the scope of this dissertation, and will be further analyzed in the next chapter. Nevertheless, it can already be said that it works by performing a number of rotations, given a number of test phases, on the received signal, and then the LPN estimation corresponds to the negative value of the rotation that minimizes the mean square error between the rotated constellation before and after the decision circuit.

Within the scope of this work, being it in a simulated environment, we will be using Blind Phase Search (BPS) exactly as presented in [47]. In practical applications, however, BPS presents a problem associated with its complexity, as the complexity increases with the number of test phases, and the number of test phases has to be increased for higher-order M-QAM formats [50]. To overcome this problem, a Maximum Likelihood (ML) CPE approach is suggested in [50]. This approach reduces BPS's complexity by resorting to several cascaded phase recovery stages. The first stage is a coarse BPS, reducing the number of test phases, followed by any number of ML CPE stages.

All the previously described approaches suffer from a problem inherent to their blind nature. Given that M-QAM constellations have rotational symmetry, cycle slips can occur and they are undetectable by blind approaches. Pilot symbols can thus be periodically inserted to remove the phase ambiguity associated with blind algorithms. This is, however, obviously done at the expense of decreasing the net data rate. A fundamental part of the work done in this dissertation revolves around how the number of pilots used per subcarrier can correctly be minimized while maintaining the quality of CPE algorithms. A detailed oversight of how the pilot symbols are inserted into the transmitted

symbol stream is given in the next chapters. After removing the LPN with Pilots, a second stage of CPE can be used, with BPS, without any additional overhead required and correcting reminiscent LPN that the first stage of CPE with Pilots was not able to correct.

2.3 Chromatic Dispersion: Modeling and Compensation

In Standard Single Mode Fiber (SSMF), a broadband transmitted signal suffers a broadening of the pulse, which is a consequence of the phase velocity of the spectral components depending on the respective frequency. This effect is known as CD, Group-velocity Dispersion (GVD), intramodal dispersion or even simply fiber dispersion. In an SSMF, it is caused by two contributions, material dispersion, intrinsic to the material used on the fiber, and waveguide dispersion, which depends on the physical characteristics of the fiber and can even be modeled to achieve a desired value (this matter won't be discussed on the present dissertation, but it can be studied in [24]). The broadening of the pulse on the transmitted signal causes ISI, and has a significant impact on the received signal. This impact makes it necessary to be able to model the behavior of CD and then develop techniques to mitigate it.

2.3.1 Time- and Frequency-Domain Analytical Modeling of Chromatic Dispersion

The frequency-domain transfer function that translates the accumulated effect of CD on the optical fiber is given by expression (2.17), where β_2 is the GVD parameter, ω is the angular frequency and z is the spatial coordinate:

$$H_{\mathrm{CD}}(\omega) = \exp(i\frac{\beta_2}{2}\omega^2 z) \tag{2.17}$$

Analyzing CD's transfer function, we can see that it has a unitary norm, meaning that it has no effect on the propagating signal's amplitude. Moreover, focusing our attention on a single frequency component of the transmitted signal, ω_k, we can see that CD's unique effect on that frequency component corresponds to a constant phase delay. This is interesting, because such an impacting fiber impairment could, in theory, be perfectly fixed with the timing recovery, if only the transmitted signal had a bandwidth narrow enough for it to be considered as having a single frequency. This fact that every frequency suffers a different constant phase delay is the obvious cause of the pulse broadening effect. Each component of a signal travels at a different group velocity through the fiber, which will cause the pulses to have a broadening correspondent to the largest delay between any two frequency components that make up the signal.

As the number of subcarriers in a system increases, while keeping the data transmission rate, the frequency band of each subcarrier decreases inversely proportionally, considering that the overall band used must remain the same. This mathematical consequence of the increase in the number of subcarriers presents an advantage concerning CD, because a signal whose spectrum is narrow enough, does not suffer significant pulse broadening, but rather just a temporal delay between the different subcarriers. So, an MSC system with a high enough number of subcarriers, concerning the effects of CD, can almost be seen as a set of non-affected subcarriers with a temporal displacement

among them. With that said, and under the mentioned assumption, the expression for that inter-subcarrier temporal delay is now derived.

Being $\phi_{\mathrm{CD}}(\omega)$ the phase imposed by CD at frequency ω, we can write:

$$\frac{\partial \phi_{\mathrm{CD}}}{\partial \omega} = \beta_2 \omega z \tag{2.18}$$

having the relation between phase and frequency:

$$\frac{\partial \phi}{\partial t} = \omega \tag{2.19}$$

we can now replace $\phi_{\mathrm{CD}}(\omega)$ by $t_{\mathrm{CD}}(\omega)$, the time delay associated with $\Phi_{\mathrm{CD}}(\omega)$, making the necessary adjustments:

$$\frac{\partial t_{\mathrm{CD}}}{\partial \omega} = \beta_2 z \tag{2.20}$$

The delay between the center frequencies of two adjacent subcarriers, assuming a constant β_2, can then be approximately given by:

$$\Delta T_{\mathrm{CD}} = L \beta_2 \Delta \omega \tag{2.21}$$

In the expression, the parameter L is the length of the fiber and $\Delta\omega$ is the spacing between subcarriers. Alternatively, ΔT_{CD} can also be expressed as a function of the dispersion parameter, $D = -2\pi c \beta_2 / \lambda^2$, expressed in ps/(km·nm), resulting in:

$$\Delta T_{\mathrm{CD}} = D L \Delta \lambda \tag{2.22}$$

In this case, L is expressed in km and $\Delta\lambda$ in nm. Having reached the time delay between adjacent subcarriers, we can extend our CD analysis. In typical systems, being the inter-subcarrier frequency spacing roughly equal to the subcarrier's frequency width, ΔT_{CD} not only represents the temporal delay between the subcarriers but also the largest delay between two frequency components of the same subcarrier. Thus, for a scenario in which no compensation for the CD is performed, we can additionally conclude that the assumption that there is no significant pulse broadening in a subcarrier is valid as long as the following condition is met:

$$|\Delta T_{\mathrm{CD}}| << T_s \tag{2.23}$$

2.3.2 Zero-Forcing Equalization of Chromatic Dispersion

Chromatic Dispersion Equalization (CDE) is one of the key DSP subsystems, as previously highlighted in Subsection 2.1.4. Given the time-invariant nature of CD, the equalization of the CD accumulated throughout the optical link can be performed in a static manner, using a zero-forcing equalizer. The transfer function of such filter must be the inverse transfer function of the CD seen in expression (2.17), which can be formulated as:

$$H_{\mathrm{CD}^{-1}}(\omega) = \exp(-i \frac{\beta_2}{2} \omega^2 z) \tag{2.24}$$

Note that this filter is usually applied on the received signal as a whole, disregarding whether it is a system with one or many subcarriers (this was implicit back in Figure 2.8,

when we saw that each entire polarization component entered the static equalization, before demultiplexing).

The equalization can be performed on the Time Domain (TD-CDE) or on the Frequency Domain (FD-CDE), and the choice between one of them is usually based on the metric of complexity. TD-CDE is preferred when the intended transmission length is small. It is performed resorting to Finite Impulse Response (FIR) [51] or Infinite Impulse Response (IIR) [52] filters. The IIR implementation has the advantage of requiring a significantly smaller number of taps than the FIR. However, IIR filters have a feedback structure that makes it impossible to do a parallel implementation, unlike FIR filters, and, for that reason, FIRs are typically the default choice for TD-CDE implementations. The theoretical expression for the FIR tap coefficients in the time domain is given by [53]:

$$a_k = \sqrt{-i\frac{T^2}{2\pi\beta_2 L}}\exp\left(i\frac{T^2}{2\beta_2 L}k^2\right) \tag{2.25}$$

where k is the index of each of the tap coefficients and T is the sampling frequency. The value of k is defined in the interval:

$$-\left\lfloor\frac{N}{2}\right\rfloor \leq k \leq \left\lfloor\frac{N}{2}\right\rfloor \tag{2.26}$$

where N is the upper bound for the number of taps [53], and it is given by:

$$N = 2\left\lfloor\frac{\pi\beta_2 L}{T^2}\right\rfloor + 1 \tag{2.27}$$

It can be noticed how the required number of taps increases with the increase in the accumulated CD.

As the transmission length increases, FD-CDE outperforms TD-CDE in terms of complexity, as concluded in [54]. This difference in the performance is due to the fact that this equalization is performed by an Fast Fourier Transform (FFT), the application of the inverse CD transfer function, and an Inverse FFT (IFFT). And, as it is of common knowledge, extensive studies have been done on the reduction of the complexity of FFT/IFFT operations. Efficient implementations of these equalization techniques are the overlap-save/add algorithms [55]. The only major disadvantage associated with FD-CDE is that it leaves us with fewer optimization possibilities, as opposed to TD-CDE, in which the development of low complexity implementations is a very researched topic [56, 57].

While there are many approaches to compensate for the accumulated CD, might those be on the time domain or on the frequency domain, one work that is of major interest to the scope of this dissertation, is the method proposed in [58], where it is experimentally demonstrated that it is possible to perform a system architecture in which the effects of CD can be almost completely disregarded by dividing the signal into subbands, that are analogous to subcarriers in MSC systems, and simply performing timing recovery and minimal equalization afterwards. Thus proving that in MSC systems, given a high enough number of subcarriers, it is experimentally possible to demonstrate higher tolerance to CD, being the most impacting consequence of CD a mere temporal displacement between subcarriers, as theoretically derived above. This experimental validation will prove fruitful in the scope of this work, in Chapter 5.

Intentionally blank page.

Chapter 3

CPE Using Independent Subcarrier Processing

When describing the effect of Laser Phase Noise (LPN) in Chapter 2, it was observed through expression (2.15) that its impact would be worse as the product $\Delta f \cdot T_s$ increases. For a given fixed transmission system, however, Δf does not change, being solely related to the physical properties of the laser. But, given the dependence on T_s, if we increase the number of subcarriers, it is clear to predict that it will have a significant impact on the performance of Carrier Phase Estimation (CPE) algorithms. Figure 3.1 makes the understanding of this impact easier. A higher number of subcarriers for the same baudrate must imply longer symbols, in fact, N_{SC} and T_s are proportional. The red dots in the figure indicate the sampling instant for each symbol, and the vertical dashed lines stipulate the T_s of the single-carrier system. As the number of subcarriers increases, T_s increases, thus reducing the granularity of sampling instants, and consequently, making it more difficult to estimate LPN.

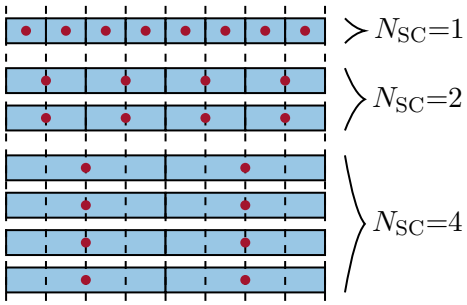

Figure 3.1: Effect of increasing N_{SC} on T_s (red dots indicate the sampling instant for each symbol and the vertical dashed lines stipulate the symbol duartion of the single-carrier system)

In this chapter we will analyze quantitatively what is the penalty associated with increasing the number of subcarriers of a system without changing the CPE algorithms applied, always having the equivalent single-carrier system as a starting point for comparison.

As simulation played a huge role in the context of this work, being all of the work built in a coherent transmission system simulator, it was a major part of the research to understand CPE algorithms and how they could be implemented in a simulated envi-

ronment. For that reason, in Section 3.1 an in-depth description of the CPE algorithms used is performed. After doing so, the simulation environment, the system parameters and the performance metrics will be introduced, in Section 3.2. Finally, the performance of the CPE algorithms is assessed without and with the effect of Chromatic Dispersion (CD), in Subsections 3.3 and 3.4, respectively.

3.1 Implementation of CPE Algorithms

Understanding the implementation of state of the art CPE algorithms is essential, only after doing so can these be explored and adapted to Multi-Subcarrier (MSC) systems. In this Section two of the aforementioned CPE algorithms are described, Blind Phase Search (BPS) and Pilots.

3.1.1 Blind Phase Search

This algorithm works by grabbing a subset of $2N+1$ received symbols, and rotating them by $B+1$ test carrier phase angles, θ_b, with:

$$\theta_b = \left(\frac{b}{B} - \frac{1}{2}\right) \cdot \gamma, b \in \{0, 1, ..., B\} \tag{3.1}$$

In the expression above, γ represents the maximum non-redundant angle on the constellation, i.e. the maximum angle without rotational symmetry (for instance, $\gamma = \frac{\pi}{2}$ for square Quadrature Amplitude Modulation (QAM) constellations). Applying BPS in an angle wider than γ would be useless, because, as will be shown further ahead, BPS extracts the LPN estimate from the rotation that best places a certain noisy symbol in a constellation position, meaning that there would be an infinite number of ideal solutions of the form $\theta_b + k\gamma$, with k taking any integer value.

For each rotation θ_b of the signal, a decision is made resorting to the decision circuit, thus inserting all rotated $2N+1$ points in the corresponding constellation fixed point, based on the decision criteria. Afterwards, the sum of the squared distance in the complex plane between the symbols before and after the decision is calculated, and the angle θ_b that minimizes this sum corresponds to the resulting phase noise estimation, following a Mean Squared Error (MSE) criteria.

Mathematically we can write the phase noise estimation for each symbol k, $\hat{\phi}_{\text{PN}}$, as:

$$\hat{\phi}_{\text{PN}} = \arg\min_{\theta_b} \sum_{n=-N}^{N} |S_{rx}(k) \times \exp(i\theta_b) - \lfloor S_{rx}(k) \times \exp(i\theta_b) \rfloor_{\mathbf{D}}|^2, \tag{3.2}$$

in which $\lfloor \cdot \rfloor_{\mathbf{D}}$ is the decision circuit outcome.

Turning now our attention to N, which was imposed at the beginning of the algorithm's description without explanation, let's try to understand why it is a necessity. Ideally, if there was no noise aside from the phase noise, N would be zero, but, because Gaussian noise adds up with phase noise, phase noise can be wrongly estimated for a symbol alone. Therefore, to reduce the effect of other sources of noise, we must have N greater than zero. The compromise we face when choosing a value for N is that a much higher N increases complexity and might attenuate the phase noise fluctuations that we intend to estimate, after all, it is still noise we are estimating, and we know

that statistically the LPN average is null. This imposes an upper bound for the value of N. Similarly, there is also a lower bound for N, because, while the effect of LPN causes the symbols to stray far from their original spot, Gaussian noise also presents a similar effect, but, not having a cumulative nature, there is no interest in accounting for it, so a minimum value of N is required to filter such Gaussian noise. In [47] a value of $N \in [6, 10]$ is presented as a fairly good choice, in a scenario that resorts only to BPS as a CPE mechanism. Note that, in this dissertation, N is expressed as a function of the number of taps, and the number of taps corresponds to $2N + 1$. The number of taps is the length of the moving average filter applied for the LPN estimation, which is clearly equivalent to the N described above.

This algorithm presents, however, a problem already suggested above, stemming from the rotational symmetry of the constellation. The problem is materialized in the form of the so-called *cycle slips*. A value of phase noise that represents an angle larger than $\frac{\gamma}{2}$ will be badly evaluated, due to the phase ambiguity associated with the rotational symmetry of M− Quadrature Amplitude Modulation (M-QAM) constellations.

Now, to summarize the algorithm and understand one possible implementation on the simulator, the pseudo-code to achieve an implementation of the BPS algorithm is described:

```
function CPE:BPS(S_rx(k))
    for θ_b, b ∈ [0, B] do
        S_rot(k) ← S_rx(k) × exp(iθ_b)
        S_ref(k) ← ⌊S_rot(k)⌋_D
        error(b, k) ← |S_rot(k) − S_ref(k)|^2
        error(b, k) ← average(error(b, k), number of taps)
    end for
    φ̂_PN(k) ← − min(θ_b,error(b, k))
    S_rx(k) ← S_rx(k) × exp(iφ̂_PN(k))
    return S_rx(k)
end function
```

In the pseudo-code above, $\min(\cdot)$ denotes the choice of θ_b that minimizes the error for each received symbol $S_{rx}(k)$.

3.1.2 Pilot-driven CPE

A solution to prevent phase ambiguity on the LPN estimations, and consequent *cycle slips*, is presented in [59]. It consists of interleaving within the data a pattern of specific sequences of pilot symbols, whose value is known at the receiver. With their presence, a periodic absolute reference for the phase noise value is achieved, because, at the receiver, we know exactly the sequence of pilot symbols that was originally sent by the transmitter.

These pilots are multiplexed with a predefined Pilot Rate (PR), R_{P}. The PR represents the ratio between data symbols and the sum of data and pilot symbols sent. For instance, a PR of 15/16 means that, for every 15 symbols of payload, it is inserted one pilot, making up 16 symbols.

Knowing that at the transmitter we sent a pilot, P, in the following manner:

$$S_{tx}(k) = \begin{cases} P_n, & \text{if } k \text{ is a multiple of } (1 - R_{\mathrm{P}})^{-1} \\ \text{payload}, & \text{otherwise} \end{cases} \tag{3.3}$$

from our received symbol sequence, we can extract the received pilots in the following way:

$$P'_n = S_{rx}(k)|_{k \text{ multiple of } (1-R_{\mathrm{P}})^{-1}} \tag{3.4}$$

Estimating phase noise is now as simple as:

$$\hat{\phi}_{\mathrm{PN}}(n) = -\arg(P_n \cdot P'^{*}_n) \tag{3.5}$$

This, however, gives only an estimate of ϕ_{PN} for one in each $(1 - R_{\mathrm{P}})^{-1}$ symbols. In between the pilot symbols, the phase noise estimation can be interpolated, typically using linear interpolation for simplicity.

Similarly to BPS, this algorithm is also susceptible to erroneous estimations of LPN caused by Gaussian noise. Practical implementations of this algorithm perform a moving average over the phase estimation, with an optimized number of taps, to reduce the effect of Gaussian noise on the estimation of the overall LPN. Therefore, the optimization of the number of taps for this moving average window follows similar reasoning to the one previously described for the BPS algorithm.

Now, as with BPS, the pseudo-code to achieve an implementation of CPE using pilot symbols is described to summarize the algorithm and understand one possible implementation on the simulator:

```
function CPE:PILOTS(S_tx(k), S_rx(k))
    for k multiple of (1 − R_P)^−1 do
        F(n) ← S_tx(k) × S_rx(k)*          ▷ n corresponds to k/(1 − R_P)^−1
    end for
    H(n) ← average(F(n), number of taps)
    φ̂_PN(n) ← − arctan(Im(H(n)), Re(H(n)))
    φ̂_PN(k) ← interpolation(φ̂_PN(n))
    S_rx(k) ← S_rx(k) × exp(iφ̂_PN(k))
    return S_rx(k)
end function
```

3.2 Simulation Environment and Parameters

Throughout this work, all results presented will be the result of simulation validations. For such results, a MATLAB simulator of coherent optical communication systems was used [60]. The overall structure of the used simulator matches the description of optical transmission systems in the previous chapter. Moreover, the simulator also includes simulations of the optical link between the transmitter and the receiver, which was also used on the scope of this work, whenever a non-null transmission length is mentioned. When a setup with a null transmission length is used, it is commonly called a Back-to-Back (B2B) configuration, because both transmitter and receiver are assembled "back to back", without any (significant) optical link in the middle.

Parameter	Value
Polarization	Single
Fiber type	SSMF
Fiber GVD (β_2)	$-20.4\,\mathrm{ps}^2/\mathrm{km}$
Baudrate	64GBd
Modulation format	64-QAM
FEC rate	5/6
Pilot rate (R_P)	31/32
Target NGMI	0.9

Table 3.1: Summary of Default System Parameters on the simulations performed.

In this work, the subjects of study are techniques to mitigate a phenomenon that only occurs between the electrical to optical conversion and vice-versa. As seen in Chapter 2, this conversion already happens in the analog domain. Being so, it might come off weird to be studying methods to correct a phenomenon that happens on the analog domain solely using a completely digital simulator. However, such study is not only possible but also valid due to the knowledge of the mathematical model for the LPN and due to the fact that all methods described to mitigate LPN, even on a real system, are only performed on the digital domain, this means that, validation-wise, we can disregard the analog part of the fiber transmission, if we know how does it impact every digital sample upon reaching the Analog to Digital Converter (ADC) on the receiver side.

The simulation of the fiber propagation used does not account for non-linear impairments. The type of fiber simulated is Standard Single Mode Fiber (SSMF), and thus a β_2 of $-20.4\,\mathrm{ps}^2/\mathrm{km}$ was considered.

In most results and unless expressly stated otherwise, the scenario considered is an optical link considering a single polarization, a baudrate of 64GBd, which is divided equally by the several subcarriers, a 64-QAM modulation, a Forward Error Correction (FEC) code rate of 5/6 and a pilot-rate of 31/32, with the number of taps optimized. A summary of these values can be seen in Table 3.1.

The performance metric used was the required Signal to Noise Ratio (SNR) to achieve a Normalized GMI (NGMI) of 0.9. The description and reason of choice for this metric are given just below.

3.2.1 Normalized Generalized Mutual Information

As previously discussed in Section 2.1.2, high-performance coding plays a key role in enabling the operation of coherent optical systems at raw Bit Error Rates (BERs) of more than 2×10^{-2}, which after FEC decoding can be reduced to as low as 10^{-15}. However, it is obviously highly demanding (or even impossible) to perform simulations that can accurately measure such low post-FEC BERs, as they would imply a simulation of at least 10^{17} bits for a precise evaluation. But, regardless of how demanding it is, for commercial applications, what is of interest is the final value of BER, after FEC, because that is what ultimately affects data transmission. To simplify this evaluation of the post-FEC value, practical solutions have appeared, to make easier the performance assessment of developed algorithms and subsystems, without demanding for such intensive

simulations. These solutions are always based on finding a consistent relation between the signal before the FEC decoding and the post-FEC BER. If such relation is found, there is no need to implement the coding/decoding blocks, and consequently no need to deal with the associated extremely low BERs, bringing an important simplification to the process of validating Digital Signal Processor (DSP) techniques.

One performance metric that for some years was of interest was the usage of the pre-FEC BER. The usage of the pre-FEC BER instead of the post-FEC BER, however, implied a constant relation between them. This assumption was true in the first generation of FEC, when it was based on hard-decision implementations, since there could be defined a deterministic relation between the input and the output of the decoding, because both only handled binary values. The introduction of soft-decoding mechanisms disrupted the constant relation before seen between pre-FEC and the post-FEC BER, because the input of the FEC mechanisms were no longer binary values, but rather real values, measuring the likelihood of a bit being a certain value, in the context of a symbol. This created a significant dependence of the chosen modulation format on the post-FEC BER, given a fixed pre-FEC BER [61], critically mining its usage as a performance metric.

Generalized Mutual Information (GMI) is a relatively recent performance metric, being first introduced in 2015 [61]. In [61], GMI was evaluated against pre-FEC BER, in both linear and nonlinear regimen, and always showing a constant relation between its value (obtained before performing FEC decoding) and the post-FEC BER. For that reason, it quickly gained interest in the research community and is now widely used as a performance metric. The good performance of GMI comes from the fact that, like soft-decision FEC (and unlike pre-FEC BER), it takes as an input real values, instead of binary values, real values carrying information on the likelihood of occurrence of a '0' or a '1', given the complex value of the analog signal corresponding to the containing symbol.

Numerically, GMI represents the number of bits per symbol that can be reliably transmitted through the Additive White Gaussian Noise (AWGN) channel, so, it is always a value in $[0, \log_2(\mathrm{M})]$, for M-QAM constellations, being $\log_2(\mathrm{M})$ the ideal maximum. It is mathematically formulated as [61]:

$$GMI = \log_2(\mathrm{M}) - G(\mathrm{M}, \sigma^2), \tag{3.6}$$

where G can be seen as a measure of information loss throughout the AWGN channel and it is given by:

$$G(\mathrm{M}, \sigma^2) = \frac{1}{N} \sum_{n=1}^{N} \sum_{k=1}^{\log_2(\mathrm{M})} \log_2 \frac{\sum_{x_m \in \mathcal{X}} \exp\left(-\frac{|y_n - x_m|^2}{\sigma^2}\right)}{\sum_{x_m \in \mathcal{X}(k, b_{n,k})} \exp\left(-\frac{|y_n - x_m|^2}{\sigma^2}\right)} \tag{3.7}$$

where σ^2 is the variance of the noise on the AWGN channel, y_n is the n-th received symbol, in a block of N analyzed symbols, x_m is one of the $\log_2(\mathrm{M})$ symbols in the constellation alphabet, $\mathcal{X}$, $b_{n,k}$ is the k-th bit of the n-th transmitted symbol and, finally, $\mathcal{X}(k, b)$ is a subset of $\mathcal{X}$ containing all symbols whose k-th bit equals b, with $b \in \{0, 1\}$.

Furthermore, to achieve independence from the modulation format chosen, the GMI is usually presented as NGMI, simply resulting of the division of GMI by $\log_2(\mathrm{M})$.

Having defined NGMI, it is now important to understand what value of it we should aim for. More specifically, to understand what is the minimum required NGMI in a

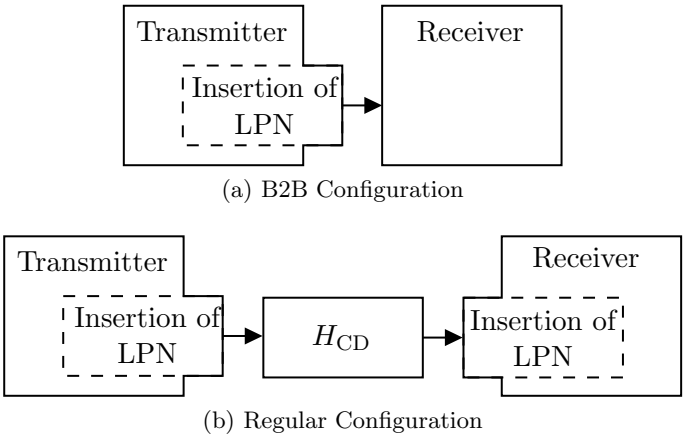

Figure 3.2: Simplified Simulator Block Diagrams, focusing on the insertion of LPN and respective interplay with CD.

system to assure that the BER requirements are met. The required NGMI is tightly related with the FEC rate of the system, because the FEC rate can be seen as the normalized number of bits that represent important non-redundant information, and, as seen above, the NGMI represents the normalized number of bits that can be considered to have been reliably received. In our simulations, we are considering a typical FEC rate of 5/6, indicating that a value of approximately 0.83 should be the goal NGMI. However, penalties associated with real implementations of FEC mechanisms have pushed the standard NGMI value to 0.9, and, for that reason, that is the same we will be using in most performance assessments. Whenever *Required SNR* is mentioned, it is implicit that it is the required SNR to achieve the target NGMI of 0.9.

3.2.2 Simulator Block Diagram

It is now important to specify the block diagram, to clarify how the effects of LPN and CD interplay. Figure 3.2 represents a simplified block diagram of the B2B configuration, 3.2a, and the configuration accounting for a non-null transmission length or regular configuration, 3.2b.

Note that this order of blocks, as every part of the simulator, was made to make sure that the simulator mimics as much as possible a real setup. On the B2B configuration, there is only a single point of insertion of LPN, as opposed to the regular configuration, where there are two points of insertion of LPN. This happens because, as mentioned in Chapter 2, in the section dedicated to modeling LPN, the sum of two effects of LPN corresponds to an equivalent unitary LPN with a Laser Line Width (LLW) equal to the sum of both of theirs, thus this simplification can be performed to lower the complexity of the simulator without any consequence. On the regular configuration, however, this simplification is no longer valid, due to the distortions inserted by CD, between both moments of insertion of LPN. In the experimental results oh this dissertation, when the value of LLW is expressed, it always corresponds to the sum of the systems' LLW. When there are two moments of LPN insertion on the simulation, the value of the LLW is, by default, equally distributed between both insertion blocks if nothing is stated otherwise.

3.3 Performance Assessment without Chromatic Dispersion

When describing both Pilots and BPS methods in Section 3.1, it has been briefly discussed how there is a compromise associated with the choice of the number of taps: on the one hand, an exaggeratedly high number of taps could filter out components of LPN, worsening the performance of CPE algorithms, while, on the other hand, an exaggeratedly low number of taps could include on the LPN estimator undesired Gaussian noise. In this first part, for a single-carrier system, N_{SC}=1, and for the usage of Pilots only, we will see the importance of optimizing the number of taps, and how an optimum value can be extracted. Note that the same following analysis could be done to a scenario with both Pilots and BPS as well as with any other number of subcarriers.

Figure 3.3 depicts the required SNR to meet the target NGMI as a function of the combined aggregate LLW of the system, for different numbers of taps. In it, it is clear to see how the number of taps impacts significantly the performance of CPE algorithms and it must be optimized. Notice how the slope of the required SNR decreases as the number of taps increases. This is because, at lower LLWs, the largest contribution to phase noise jumps estimated at each symbol is caused by Gaussian noise, and thus a higher number of taps outperforms a lower number of taps. On the other hand, at higher LLWs, a major part of the phase noise jump is caused by LPN, resulting in lower tap numbers being associated with a better performance. The theoretical limit represents the required SNR to obtain an NGMI=0.9 if there was no phase noise on the system. In the case of this figure, the ideal number of taps can be considered approximately constant, 7 taps. It should be realized that in some cases an adaptive number of taps as a function of the LLW may be required, but that is not the case of the scenarios presented throughout this work, given the LLW and operating SNR ranges considered.

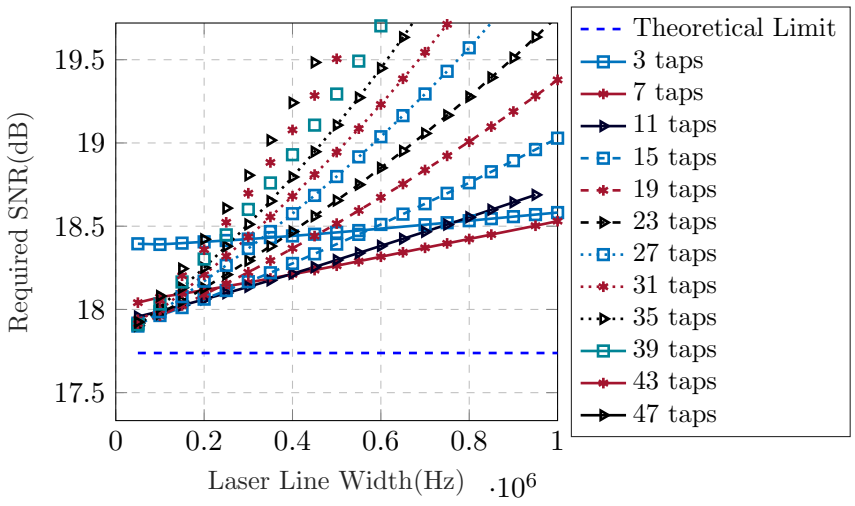

Figure 3.3: Effect of the number of taps chosen on the performance of CPE algorithms.

With the importance of the optimization of the number of taps in mind, for the remaining of the thesis all results presented will have been optimized to the number of taps, to simplify result analysis. Nevertheless, the optimum number of taps considered will be indicated. It shall be noted that in scenarios in which both Pilots and BPS

are applied, the optimization was performed in two steps, first optimizing the number of taps for the Pilots and then optimizing the number of taps for the BPS. It is thus assumed that such approach leads to good optimization results. The alternative would be to perform cross optimization, which was not done due to the associated complexity. Concerning the number of taps on future results, the notation "$x + y$ taps" represents the taps used when two CPE stages were performed. x is the number of taps used on the first stage, using Pilots, and y the number of taps used on the second stage, BPS variants.

Now that we have established the importance of the number of taps, let's move on to the main point of this chapter, which is to measure the impact of the symbol rate in the performance of CPE algorithms. In Figure 3.4 we are able to see the results of increasing the number of subcarriers while maintaining the overall bitrate of the system. Analyzing the figure we can see how the required SNR increases along with the number of subcarriers, because the increase in the number of subcarriers will increase T_s. The tendency that is seen corresponds to what would be expected, because we know that the variance of the Gaussian variable that models the LPN is both a function of LLW and T_s, thus, as an example, fixing our attention on the results for 8 and 16 subcarriers, and at LLW of 400 kHz and 800 kHz, we know that the symbol period changes by a factor of two as well as the LLW, thus bearing similar performances in terms of required SNR.

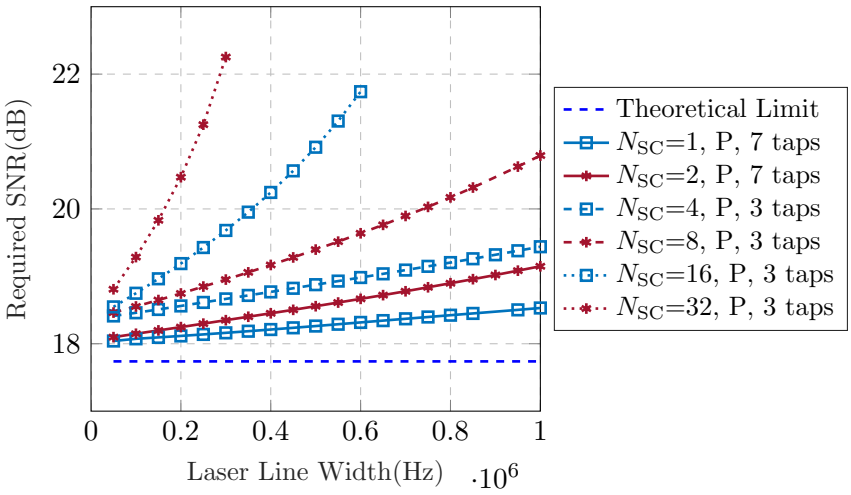

Figure 3.4: Performance of CPE using only Pilots (P), for several values of N_{SC}.

Now, BPS can be added as a second stage of CPE, to attempt to correct reminiscent LPN left uncorrected by the usage of Pilots, mainly a consequence of the interpolation performed between non-Pilot symbols. The results obtained are shown in Figure 3.5, where a slight improvement in the required SNR can be observed. The improvement, however, only slows down the impact of the LLW, causing a visible horizontal stretching effect. It does not affect the overall relation between the curves, and the tendency to get increased SNR requirements when opting for a system with a higher number of subcarriers. On these terms, it is still a clear disadvantage to opt for an MSC system.

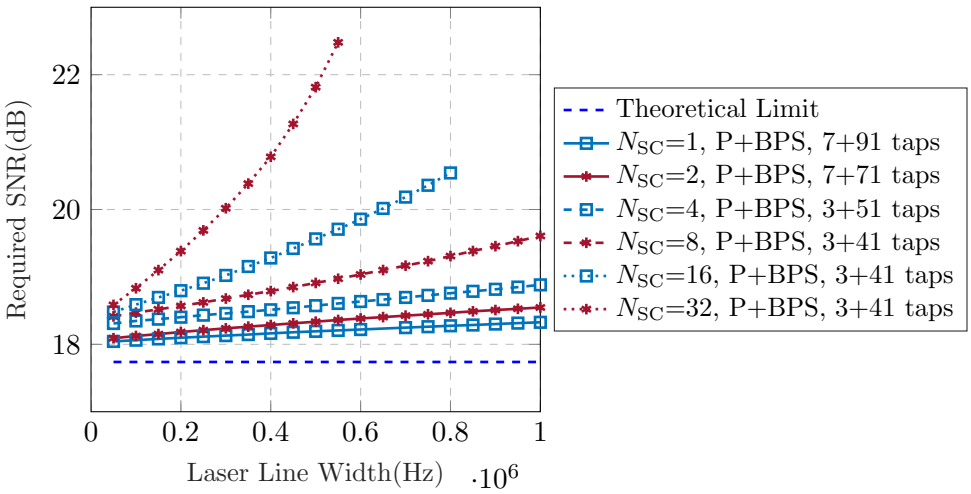

Figure 3.5: Performance of CPE using a first stage with Pilots (P) and a second stage with BPS, for several values of N_{SC}.

3.4 Performance Assessment with Chromatic Dispersion

Now, it is analyzed how the presence of CD impacts the performances observed in the last section. It is expected to have the performance of systems with a smaller number of subcarriers more affected than those with a larger number of subcarriers, because, as seen earlier, an increase on the number of subcarriers represents a decrease on the bandwidth of each subcarrier, which will thus decrease the relative impact of CD on the subcarrier, considering that the transfer function of CD, (2.17), is a constant phase rotation whose value, in a fixed transmission system, is solely a function of the frequency.

In Section 2.3 an expression was derived, (2.23), that imposes a rough condition on the ratio $|\Delta T_{CD}|/T_s$, and it has been concluded that this ratio should be below one to assure Inter-Symbol Interference (ISI)-free operation, in a system with the effect of CD but without Chromatic Dispersion Equalization (CDE). Let us now look at the values that this ratio takes in our simulation environment, in Figure 3.6. It is very important to find a relation between this ratio and the actual SNR penalty as a function of the number of subcarriers of the system. We can see that, before CDE, only an N_{SC}=32 would respect the pulse broadening condition at the 2000km range. On the other extreme, a N_{SC}=1, for the same transmission length, will suffer an enormous pulse broadening, corresponding to around a thousand times the symbol period. Such high pulse broadening values will make the usage of CDE imperative. However, while CDE equalizes the signal and restores the transmitted signal, removing ISI, it also affects LPN. To the LPN component inserted by the transmitter's laser, CDE will be beneficial, in the sense that it will restore its initial state, just as with the transmitted signal. However, for the LPN inserted by the Local Oscillator (LO), which had not suffered from the effect of CD, this will result in an effect equally disruptive, the effect of CD^{-1}, which causes a pulse broadening effect that is equal to the one experienced by the signal before CDE, changing its nature and thus its model accuracy. This effect of CDE on the LO's LPN component is known in the literature as Equalization-Enhanced Phase Noise (EEPN) [62], and it adds to the LPN model a new contribution, which is a function of the

accumulated CD and of the symbol period, thus increasing its variance, and worsening the performance of CPE algorithms.

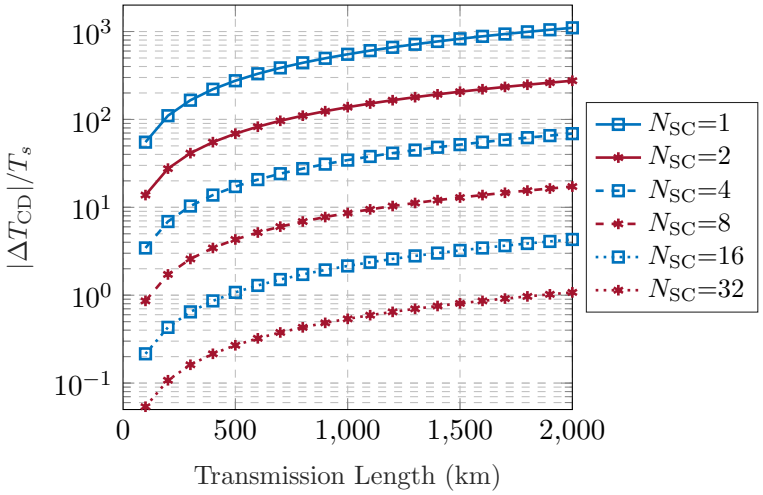

Figure 3.6: Pulse broadening ratio condition as a function of the transmission length.

In Figure 3.7, the impact of CD in a single-carrier system is shown. In this scenario, both Pilots and BPS were used. As a point of comparison, the results for a B2B setup were added, which correspond to a scenario without the effect of CD, already assessed in Figure 3.5. We are able to see how the increase on the fiber length, L, causes the CD impact to be more noticeable, for instance, when considering an L=2000 km, which is a typical transmission distance for the kind of coherent systems assessed in this work, and a LLW of 1 MHz, a single-carrier system requires approximately 4 dB higher SNR to achieve the same target NGMI.

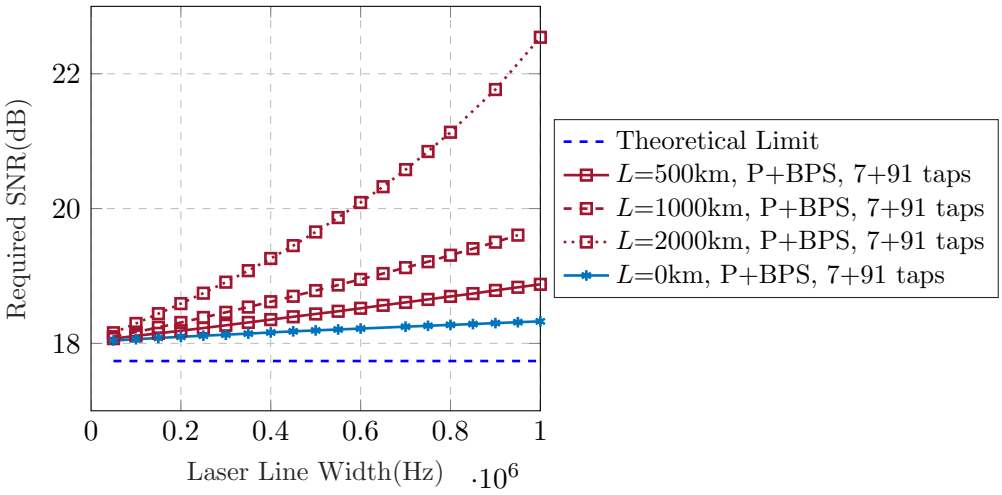

Figure 3.7: Performance of CPE with two stages, Pilots and BPS, in the presence of CD for single-carrier systems.

Taking a look at a system with a higher number of subcarriers now, Figure 3.8 shows how in an MSC system with just 8 subcarriers CD presents little to no additional power

requirement, because the value of required SNR has not changed noticeably independently of L. This result makes perfect sense, because, assuming an ideal CDE, it has been seen that the only impact of CD is on the pulse broadening of the LO's LPN. For N_{SC}=8, it was shown in Figure 3.6 that the normalized pulse broadening is always lower than 20 symbols, for transmission distances below 2000 km, which is smaller than the LPN pulse broadening imposed by the moving average of the optimum number of taps, thus, the effects of the pulse broadening aren't felt, as they are erased by the nevertheless required LPN filtering. Note that this condition obviously does not hold true for the single-carrier scenario, whose normalized pulse broadening is already over 250 symbols for a transmission distance of 500 km and thus the measured penalty.

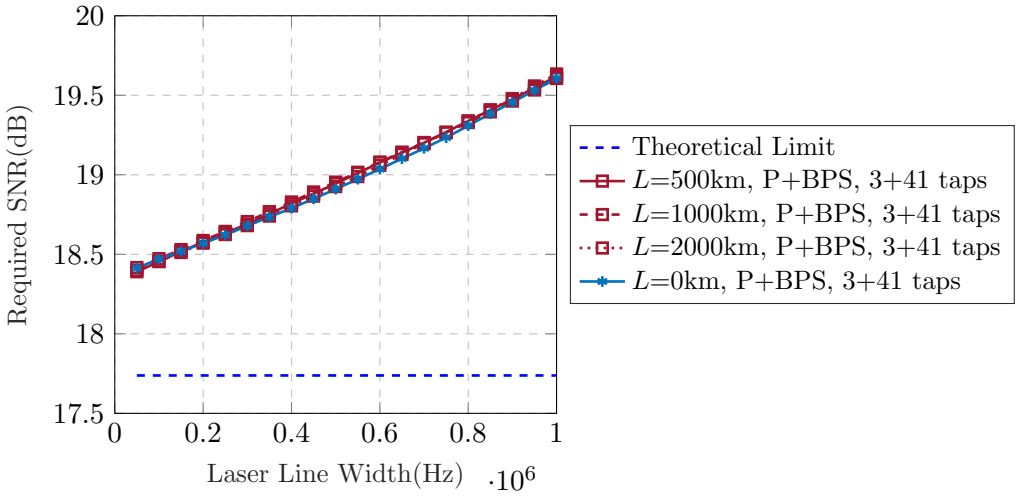

Figure 3.8: Performance of CPE with two stages, Pilots and BPS, in the presence of CD for N_{SC}=8.

Extending our analysis to a higher number of subcarriers, it is possible to measure quantitatively the penalty in the Required SNR of CD as the number of subcarriers varies. This impact can be presented in two interesting ways, which will be analyzed just below.

The first way, emphasizes that it is important to analyze what is the additional power required to achieve the same NGMI, as we increase the number of subcarriers, assuming linear propagation. With that objective in mind, Figure 3.9 shows that, for a fixed transmission length of 2000 km, a number of 8 subcarriers or higher is enough to completely ignore the impact of CD on the power requirements. Once again, it is curious to analyze how this interplays with the values that the ratio $|\Delta T_{CD}|/T_s$ takes in this interval. In general, the penalty associated with CD-enhanced phase noise can be considered negligible once the CD-induced pulse broadening becomes shorter than the optimized CPE averaging window. Naturally, this condition is more easily met for MSC signals with a high enough number of subcarriers, which in the considered simulation scenario corresponds to $N_{SC} \geq 8$.

While the results discussed in the former paragraph might sound compelling, it is important to bear in mind that, while CD adds no penalty to systems with $N_{SC} \geq 8$, there is still the penalty associated with the increase of the number of subcarriers, observed in the previous section. This takes us to the second analysis in which the impact of

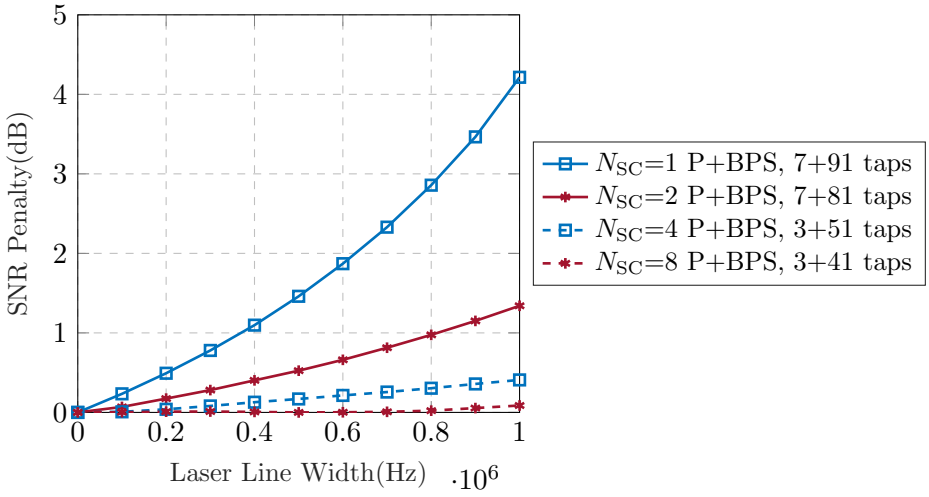

Figure 3.9: Penalty associated with CD for L=2000km, using as base for comparison the respective B2B scenario.

CD can be presented. A more thorough SNR penalty analysis would be to account for both effects, the penalty associated with CD and the one associated with the number of subcarriers. Figure 3.10 shows those results, for a fixed fiber length of 2000 km. This time, the penalty is referenced to the theoretical limit of the required SNR.

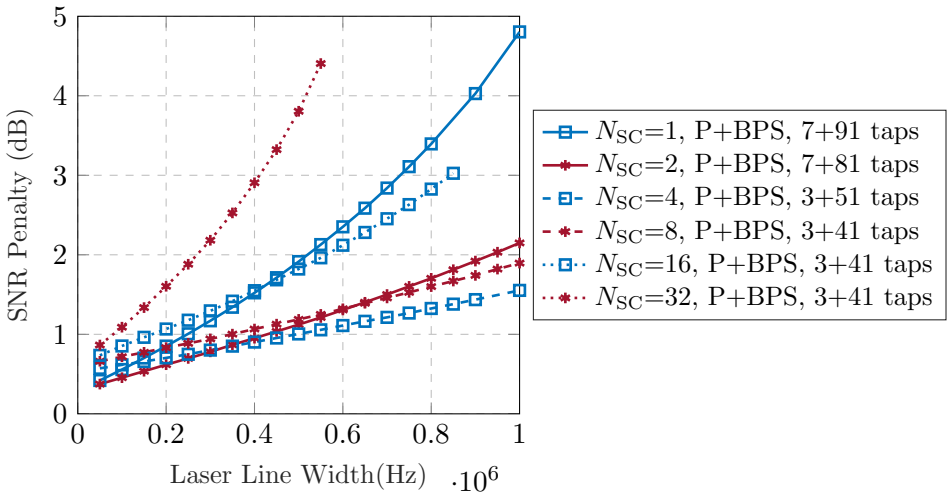

Figure 3.10: Penalty associated with CD for L=2000km, using as base for comparison the theoretical value of the required SNR.

From the analysis of Figure 3.10, two major conclusions can be drawn: i) while efficient for low laser linewidths, the single-carrier solution becomes strongly affected by EEPN at combined laser linewidths of roughly more than 200 kHz, which limits its performance in long-haul optical links that are mildly impaired by phase noise; ii) an optimized compromise between enhanced resilience to EEPN and CPE implementation penalty can be obtained by using 4-8 subcarriers, which corresponds to a symbol-rate per subcarrier in the range of 8-16 Gbaud. It is worth noting that this range of symbol-

rates is very well aligned with few recent practical demonstrations of commercially-ready MSC transceivers [9]. The reason for the choice of these symbol-rates is certainly not only a coincidence, and thus it clearly demonstrates the relevance of the problem hereby addressed. Stemming from the preliminary simulation analysis carried out in this chapter, in the next chapters we will proceed seeking novel solutions to enable the use of lower symbol-rates per subcarrier (ideally 2-4 Gbaud, in order to optimally explore the effect for symbol-rate optimization [6]) with reduced implementation penalty.

As a closure for this chapter, one shall note that, up until now, the best compromise between the impact of CD and the one of the increase on the number of subcarriers, for the scenario analyzed of a transmission length of 2000 km is the case with 4 subcarriers, using two stages of CPE, and no alternative with 32 subcarriers or more seems implementable with anywhere near similar performance.

Chapter 4

CPE Using Joint Subcarrier Processing

In Chapter 3 we saw that, while all Carrier Phase Estimation (CPE) algorithms developed for single-carrier systems can be directly applied to each subcarrier of a Multi-Subcarrier (MSC) system individually, that is not the best approach, and it brings a non-negligible penalty when compared to the performance of the respective single-carrier systems, stemming from the fact that T_s enlarges by a factor of N_{SC}. Given this and the fact that all subcarriers in a channel are always processed at the same moment, it is only a natural evolution to have jointly processed CPE techniques, thereby enabling to overcome the penalty associated with the decrease of the symbol rate.

The study of how to properly employ the typical CPE mechanisms in MSC systems is not a novelty, it is pretty much a logical step, when trying to migrate from a single-carrier system to an MSC, trying to make the most of their increased tolerance to fiber impairments. In this chapter, possible approaches aiming at optimizing the performance of CPE algorithms in MSC systems are presented, always having as a starting point the premise of never adding additional overhead to the transmitted signal, to be able to make a fair performance comparison at all times.

In Section 4.1 modifications to the typical CPE algorithms assessed in Chapter 3 are described. Then, in Sections 4.2 and 4.3, their performance is assessed, without and with the effects of Chromatic Dispersion (CD), respectively.

4.1 Optimization of CPE Algorithms for Multicarrier Systems

In this section there is a subsection devoted to the optimization of pilot-based CPE, presenting two different approaches, and a subsection devoted to Blind Phase Search (BPS), also presenting two different approaches.

4.1.1 Pilots

Concerning Pilots, when T_s increases, with the increase in the number of subcarriers, the time gap between Pilots also increases, because the same Pilot rate in symbols with a longer period will represent a worse estimate of the Laser Phase Noise (LPN).

Intending to achieve the same time gap between Pilots in an MSC system as in a single-carrier system, there are three main possibilities. The first, highly undesirable, would be to simply increase the Pilot rate for each carrier. This would not, however, be a fair comparison, because we are increasing the overall overhead, and the system no longer would be comparable to an equivalent single-carrier system, which is our goal. The second approach is, while keeping the same Pilot rate in each subcarrier, instead of inserting Pilots synchronously, insert them spaced out, Spaced Pilots (SP). This way all the Pilots from the various subcarriers can be combined achieving once again the same desired Pilot rate as in the equivalent single-carrier system. The third would be to send all the pilots in a single subcarrier, a Single Reference Carrier (SRC), thus increasing the pilot rate of a subcarrier and applying the same phase correction for all, thereby also maintaining a fixed pilot-rate.

Spaced Pilots

If instead of sending the pilots simultaneously to all subcarriers, we evenly space the pilots between the various subcarriers and correlate the phase estimation attained from each of them, we can have a CPE with the same granularity as in the single-carrier scenario. Similar approaches have been assessed, as is the case in [63].

In Figure 4.1 we see an example of this concept, in which the squares represent the various sent symbols, and the red symbols represent the ones corresponding to pilots, visibly equally spaced throughout the time.

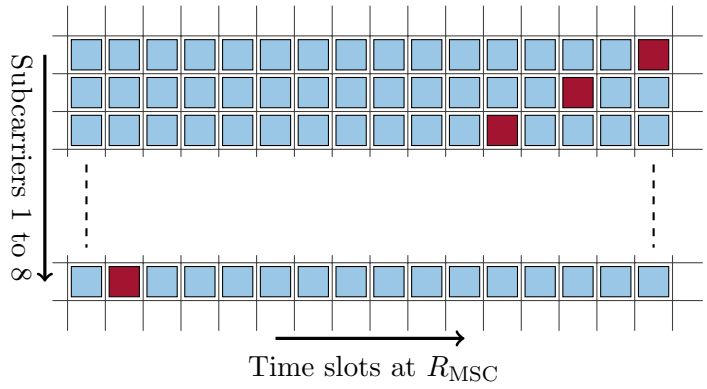

Figure 4.1: Example of application of Spaced Pilots for $N_{\mathrm{SC}} = 8$ and $R_{\mathrm{P}} = \frac{15}{16}$.

As described in 2.2, when in a single-carrier system, adding the Pilots is simply interleaving the signal with the known Pilots sequence, P_n, at all $m(1-R_{\mathrm{P}})^{-1}$ indexes. Now, in MSC, each subcarrier will still have a Pilots periodicity of $(1-R_{\mathrm{P}})^{-1}$, however, to guarantee the same absolute frequency of LPN estimation as in the single-carrier system, we will have to add an offset, $\delta_{P,n}$, to the instance of Pilot appearance. This offset is constant throughout the time and has a different value for each subcarrier:

$$\delta_{P,n} = -\left\lfloor \frac{n-1}{N_{\mathrm{SC}}} \cdot (1-R_{\mathrm{P}})^{-1} \right\rfloor, n \in 1,2,...,N_{\mathrm{SC}} \tag{4.1}$$

Using equation (4.1) in the example in Figure 4.1 we obtain for $n = 1,2,3,...,8$, $\delta_{p,n} = 0,-2,-4,...,-14$. This leaves us with the following formulation of the indexes to

place the Pilots:

$$index\ of\ P_{n,k} = k(1 - R_{\mathrm{P}})^{-1} - \left\lfloor \frac{n-1}{N_{\mathrm{SC}}} \cdot (1 - R_{\mathrm{P}})^{-1} \right\rfloor \tag{4.2}$$

After recovering the Pilots at the receiver's Digital Signal Processor (DSP), $P'_{n,k}$, and retrieving the phase estimations, using equation (3.5), we can map all the estimations to respective indexes and obtain the complete estimate for ϕ_{PN}.

Single Pilots Reference Carrier

By having all Pilots put in a single subcarrier, as shown in Figure 4.2, we can relax complexity on the receiver, by avoiding to perform CPE in all subcarriers, and also avoiding to interpolate information from the several subcarriers to build an LPN estimate. We simply need CPE in the subcarrier with the pilots to build an estimate of the carrier phase noise. The same phase compensation is then applied to all subcarriers. A conceptually similar scheme to CPE is proposed in [12], treated as "CPE1".

Additionally, when CD is added, there might be expected gain from the lack of need to interpolate among differently timed signals.

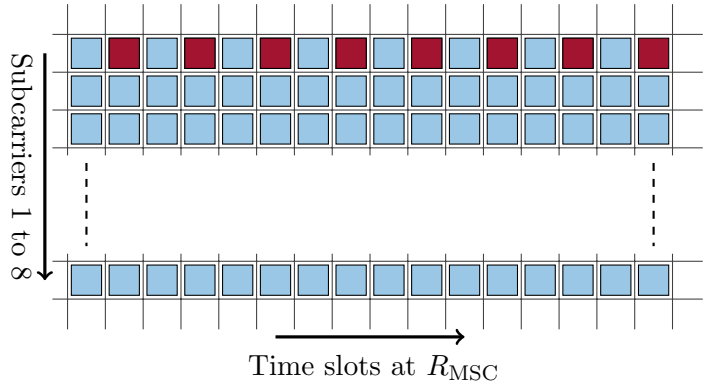

Figure 4.2: Example of application of Single Pilots Reference Carrier for $N_{\mathrm{SC}} = 8$ and $R_{\mathrm{P}} = \frac{15}{16}$.

The practical implementation of this algorithm does not differ much from the implementation of the regular Pilots, described in Chapter 3. The only two notable modifications are the Pilot Rate (PR) on the subcarriers and the fact that the subcarriers without Pilots (all but the reference carrier) will have a carrier phase correction mechanism consisting of the application of the phase estimate obtained from the reference subcarrier.

Given a system with an overall PR of R_{P}, the effective PR of the reference subcarrier, $R_{\mathrm{P}ref}$, will be:

$$R_{\mathrm{P}ref} = 1 - (1 - R_{\mathrm{P}})N_{\mathrm{SC}} \tag{4.3}$$

To close this subsection, it is worth mentioning that hybrid approaches stemming from the previously described concepts of "spaced pilots" and "pilot reference subcarrier" can also be considered. For instance, instead of a single reference subcarrier concentrating all the pilot symbols, one can also consider $N < N_{\mathrm{SC}}$ reference subcarriers with

spaced indexing of pilot sequences between them. Although these hybrid approaches will not be explored in this chapter for simplicity, this concept will come in handy during the presentation of Chapter 5.

4.1.2 Blind Phase Search

Concerning BPS, it may seem like a harder challenge than pilots, because inherently it requires all received symbols to be used during the phase estimation process. In this case, there are two main approaches to match the estimating frequency of LPN achieved in single-carrier systems. The first is to average all the BPS phase estimations and apply the same phase correction on all subcarriers: this will allow the number of taps to decrease, because the error associated with the blind estimate will decrease. The second is to stagger all the subcarriers in time, making use of the fact that all subcarriers need to be oversampled in an MSC system.

Joint Blind Phase Search

As already suggested above, the first and most obvious approach to optimize the performance of BPS in MSC systems is to make use of all the estimates being made in parallel, evidenced by Figure 4.3, to generate a more noise-tolerant estimate. This approach was based on the approach called "CPE3" in [12]. Within the framework of this thesis, this approach will be henceforth designated as Joint BPS (JBPS).

The performance improvement provided by this algorithm comes from the usage of the average of several subcarriers' phase estimates, which make the phase estimate at each time instant less affected by Gaussian noise, thus relaxing the number of taps required. Consequently, fewer taps mean a smaller spreading of the LPN value at each instant, obtaining a better estimate. Eventually, it is expected that, with a high enough number of subcarriers in a system, a single-tap CPE becomes optimal. Notice, however, that this inserts a dependence of the number of taps on the number of subcarriers. Additionally, as the number of subcarriers increases, there is a longer time gap between CPE estimates, increasing the probability of cycle slips.

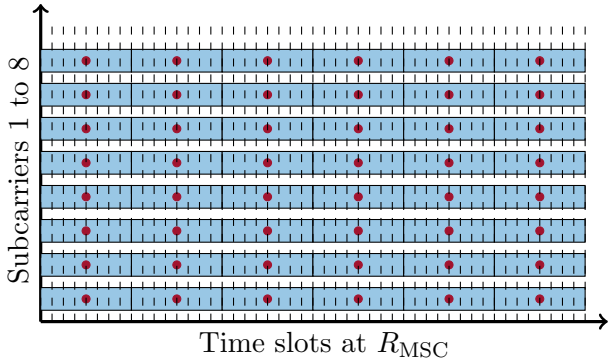

Figure 4.3: Diagram evidencing the LPN sampling instants for $N_{\mathrm{SC}} = 8$, when using regular BPS.

Staggered Blind Phase Search

An alternative approach to improve the performance of BPS in MSC systems is by making use of the high sampling rate needed for MSC, ($2 \times N_{\mathrm{SC}}$ times the symbol rate of each subcarrier, R_{MSC}) to, once again, have more granularity on the phase estimations. This approach was also implemented and studied in [64]. In this dissertation, this approach receives the name of Staggered BPS (SBPS). It can be implemented in practice by adding a delay to each subcarrier k,

$$\delta_{\mathrm{SBPS},k} = \frac{1}{R_{\mathrm{MSC}} N_{\mathrm{SC}}} \cdot (k-1), k \in 1, 2, ..., N_{\mathrm{SC}} \tag{4.4}$$

By doing so, we go from the scheme in Figure 4.3, in which we only have an absolute CPE frequency equal to the subcarrier symbol rate, to the scheme in Figure 4.4, in which we have an absolute CPE frequency N_{SC} times higher, i.e. equal to the single-carrier CPE frequency.

The red dots in the figure indicate the point at which the symbol is evaluated, and, consequently, the time instant at which the carrier phase noise is estimated. With the help of this figure, the utility of staggering the subcarriers becomes obvious.

The BPS algorithm can then work exactly as it would in a single-carrier system because all the symbols of the various subcarriers can be aligned in time to form a stream of symbols equal to the one sent if it were the case of a single-carrier system. This method has two advantages in comparison with JBPS: i) it removes the dependency of the number of subcarriers on the number of taps and ii) it does not increase the time between CPE estimates.

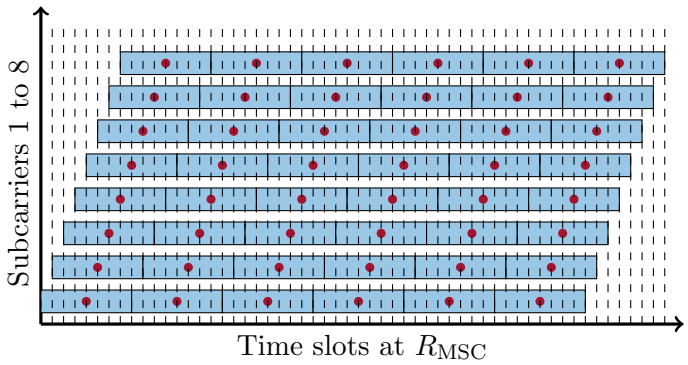

Figure 4.4: Example of application of Staggered BPS for $N_{\mathrm{SC}} = 8$.

4.2 Performance Assessment without Chromatic Dispersion

In this section, will be assessed the performance of the joint subcarrier CPE methods described above, starting with the pilot-based CPE approaches. To simplify the analysis, only the scenario with N_{SC}=32 will be shown, which will be compared to the scenario of a single-carrier system. This simplification is done under the clear assumption that if the approaches can match a single-carrier scenario, any lower number of subcarriers can also match the performance of the system with 32 subcarriers.

In Figure 4.5 we can see how both approaches discussed at the beginning of the chapter can effectively match the performance of the pilot-based CPE in single-carrier systems, without adding any overhead, given that in both cases the overall PR was the same. These are very encouraging news in the context of this dissertation, as it means that, at least for Back-to-Back (B2B) scenarios, the impact of the increase of the symbol period can be mitigated by the aforementioned joint subcarrier pilot-based CPE approaches. Indeed both the SP and the SRC methods are found to yield similar performance in a CD-less scenario. The choice between one of these approaches can then be motivated by other practical design factors. For instance, in a system with strong optical filtering [65] it might be beneficial to consider the use of a SRC, placed on the edge of the channel, thereby reducing the impact of the filtering on the actual information data.

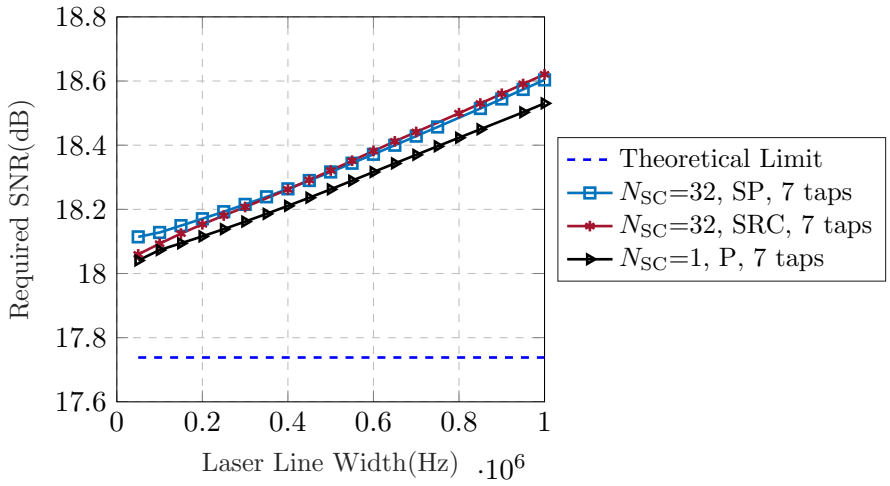

Figure 4.5: Performance of CPE algorithms based solely on the usage of pilot symbols, in particular, the performance of the suggested algorithms: Spaced Pilots (SP) and Single Reference Carrier (SRC).

Similarly, the same comparison can be done with both JBPS and SBPS, in Figure 4.6. We can see that a regular BPS has no gain when compared to SP for N_{SC}=32. This makes sense, because, with SP at R_P=31/32 and 32 subcarriers, we already have a phase estimate for each symbol, thus regular BPS is not expected to improve performance. However, both SBPS and JBPS show performances much closer to one of the single-carrier system. Notice how the dependence on N_{SC} of the optimum number of taps was felt on the JBPS but not on the SBPS, in which the number of taps remained very close to the one of the single-carrier system.

When opting between SBPS and JBPS in the next simulations, SBPS was chosen because although it presents the same results as JBPS, it has the advantage of having a number of taps that is independent of the number of subcarriers. The typical ratio between the number of taps of SBPS and the one of JBPS is N_{SC}, which is easily understood by the fact that in JBPS, every N_{SC} phase estimates are averaged for a given symbol. That ratio is numerically verified by the results in Figure 4.6, where, in the implementation with 32 subcarriers, changing from SBPS to JBPS meant a division of the optimum number of taps by approximately 32. This dependence of the number

of subcarriers on the number of taps represents yet another limitation to JBPS, because if the optimal number of taps is lower than N_{SC}, the optimal performance cannot be achieved, being an additional reason to drop the JBPS approach, in favor of the SBPS one.

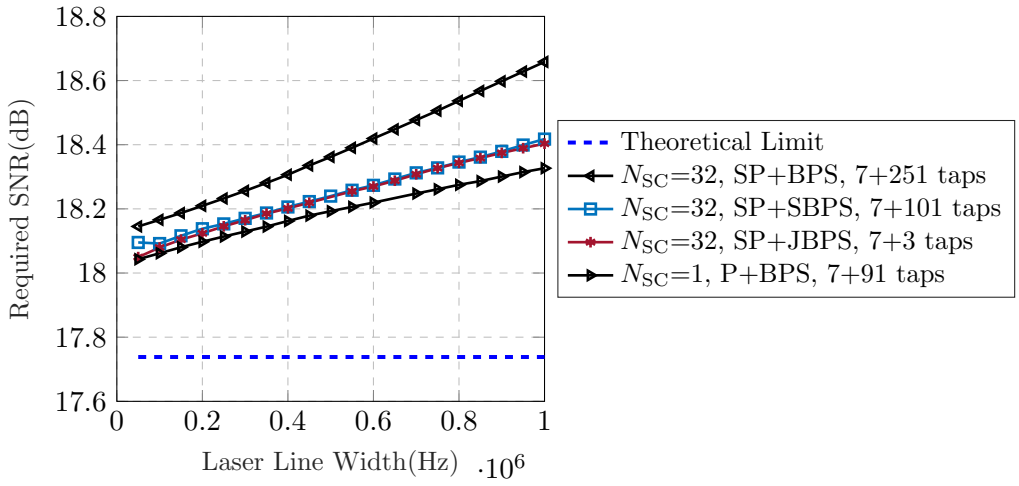

Figure 4.6: Performance of CPE algorithms based on the usage of SP and with different approaches to the second stage of CPE, in particular, the performance of the suggested algorithms: Staggered BPS (SBPS) and Joint BPS (JBPS).

The results in Figure 4.6 were promising, approximating the performance of SBPS in a system with 32 subcarriers to the performance of regular BPS in single-carrier systems. However, a pilot rate of 31/32, for this particular case, did not leave much room for improvement between the performance of regular BPS in both single-carrier and 32 subcarriers systems. To better analyze the possible gain introduced by SBPS, let us now consider a scenario with lower usage of Pilots, to increase the potential improvement gap between the performance of regular BPS in both systems. Figure 4.7 shows a similar setup to the one used in the previous simulations, but with an increased pilot rate, R_P=511/512. At this pilot rate, we can see that the performance of SP for N_{SC}=32 still matches one of the regular pilots for a single-carrier system, but now the required Signal to Noise Ratio (SNR) is much larger for both, given the smaller frequency of Pilots. Regular BPS can present a major gain in the single-carrier system, but little to none in the MSC. This is where the gain of the usage of SBPS is made obvious, because it enables to match the performance of regular BPS in a single-carrier system, which is the major objective of this study. It is important to notice how in these last two approaches the optimum number of taps was maintained, emphasizing the independence of the number of taps on the number of subcarriers used for the SBPS.

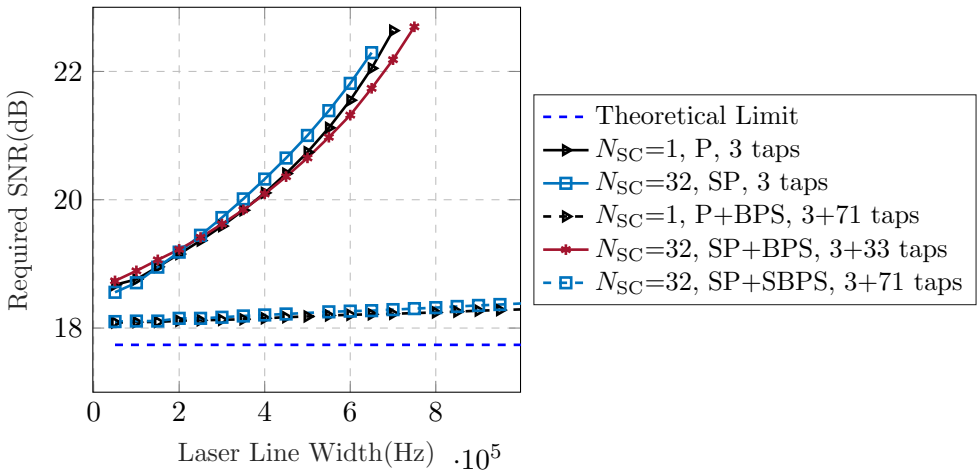

Figure 4.7: Performance of the SBPS algorithm with a higher R_P of 511/512.

4.3 Performance Assessment with Chromatic Dispersion

In the previous chapter, Chapter 3, it was seen how when processing subcarriers independently, CD does not pose a problem for $N_{SC} \geq 8$, i.e. for symbol-rates per subcarrier below 8 GBaud. But what is the impact of using joint subcarrier processing when the effect of CD is present? Figure 4.8 shows the behavior of the SP (4.8a), SRC (4.8b) and SBPS (4.8c). In these, we can evaluate how the effect of joint-subcarrier CPE processing interplays with the existence of CD.

We can see that, for any of the previously suggested jointly processed CPE techniques, the performance is always worse than the performance of single-carrier systems, independently of the transmission length, even for the SRC approach, which is the best-performing approach of the three seen in Figure 4.8. This way it seems that the advantage brought to us by the usage of MSC systems concerning the tolerance to CD is not compatible with the joint processing techniques. This happens because, even though each subcarrier in MSC systems is not affected by CD, the LPN affecting each subcarrier is still different, which means that joint CPE processing cannot be done without taking into consideration the effects of CD.

It is, however, an interesting conclusion, that the LPN among the subcarriers differs so much that the penalty from assuming it remains unchanged is larger than the penalty associated with the Equalization-Enhanced Phase Noise (EEPN) in single-carrier systems.

The accelerated rate at which the impact of CD is felt as the transmission distance increases is now an interesting topic of analysis. In Figure 4.9 we are able to see, for a fixed value of LLW, Δf=500 kHz, how at little below 3000 km, and for N_{SC}=32, it is even better to opt for an independently processing CPE as opposed to the best-performing joint processing alternative (SRC).

This is a turning point in the study performed up until now. As of now, after reaching the current limit of the state-of-the-art on CPE strategies for MSC systems, it seems to be impossible to fight both the impact of CD and the impact of the increase in the number of subcarriers. Single-carrier systems have an intrinsic EEPN penalty due to the relation between CD and their wide spectrum. In turn, MSC systems have an intrinsic

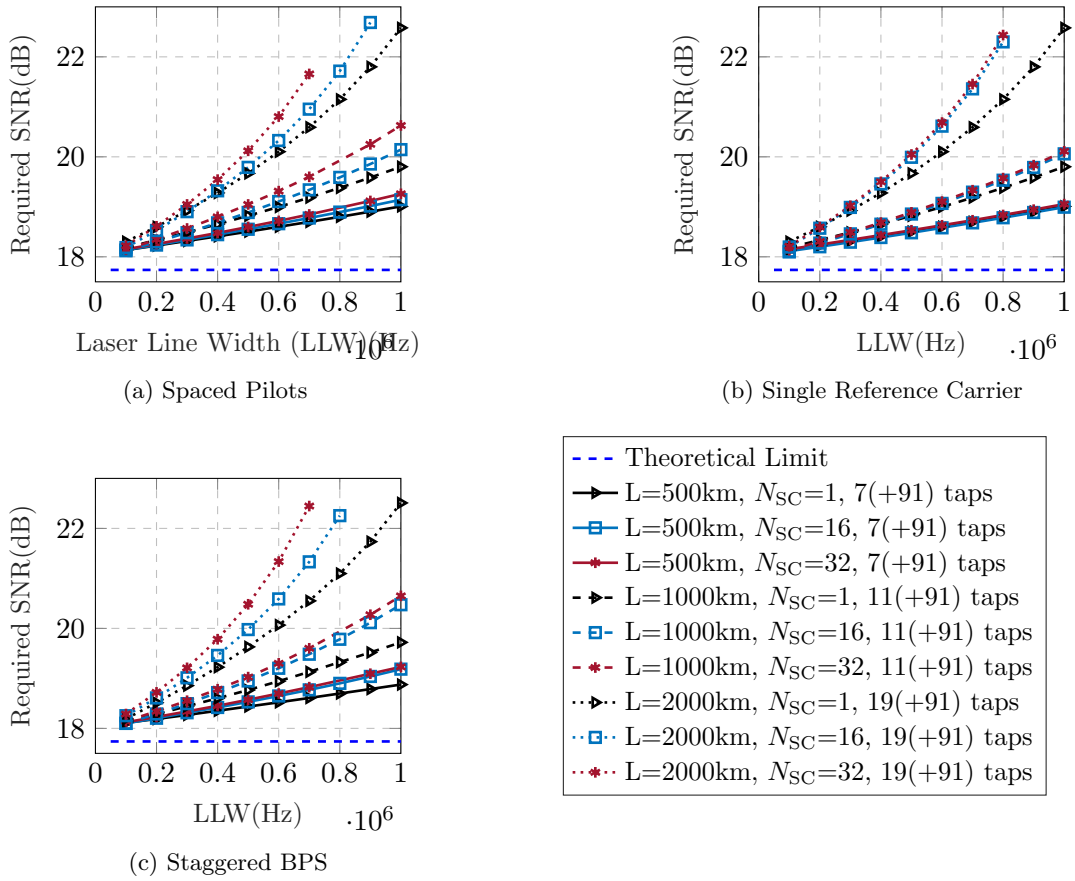

(a) Spaced Pilots

(b) Single Reference Carrier

(c) Staggered BPS

Figure 4.8: Performance of several jointly processed CPE algorithms in the presence of CD.

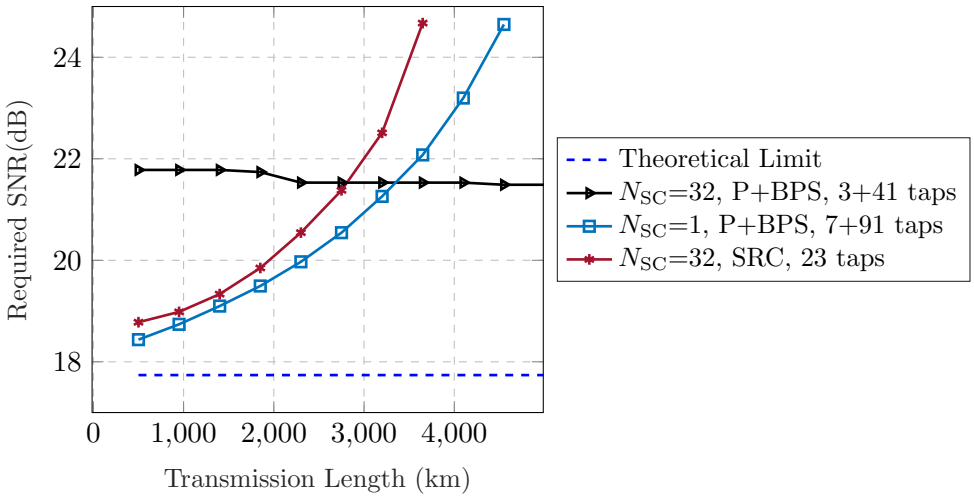

Figure 4.9: Performance of independent vs. joint processing CPE as the transmission length increases.

penalty due to the decrease of the symbol rate, which in Section 4.2 was shown to be solved with the presented joint processing techniques, but has now been demonstrated that it cannot properly deal with the effect of CD. This leaves us with a conclusion: while joint processing techniques are ideal and match the performance of single-carrier systems in scenarios with low accumulated CD, they are rendered useless when the impact of CD increases, similarly to the single-carrier equivalents or even worse than them.

This chapter ends with the realization that joint processing in MSC systems cannot work in scenarios of high impact of CD. But, one thing must be kept in mind: SP allied with SBPS still managed to perfectly match the performance of single-carrier systems in scenarios with low to none impacting accumulated CD, and SBPS presents no limitations concerning the number of taps nor the number of subcarriers, meaning that it can and should be considered in applications that can profit of longer symbol periods. One interesting area of interest for this technique could be short reach transmission systems or free-space optics, both can be considered to have low to null CD impact.

Given the lack of viable options in the state-of-the-art for long-haul MSC optical fiber transmission, in the following chapter novel dedicated CPE techniques will be devised, specifically designed for optimized performance with a high number of subcarriers and large accumulated CD.

Chapter 5

Advanced CPE Using a Novel Dual-Reference Subcarrier Approach

This chapter is once again the next logical step on the research path of this work. We have shown that joint processing for Carrier Phase Estimation (CPE) is the only possible way to match the performance of single-carrier systems. However, the added impact of Chromatic Dispersion (CD) seems to hinder any joint processing technique previously suggested. This demands for a total revision on the way joint CPE is employed, and how it can interplay with the deterministic impact of CD.

So far, we have numerically explored the impact of CD, and we have measured its associated Signal to Noise Ratio (SNR) penalty as well. Now, it is of use to pinpoint exactly where does the added penalty come from, by taking a look at a simplified block diagram of the transmission system, with the elements that constitute the impairment of CD. In Figure 5.1, we highlight four moments pre-CPE that should not be ignored or assumed perfect by the CPE subsystem. Firstly, the transmitted signal suffers the impact of the transmitter Laser Phase Noise (LPN), on the electrical to optical conversion. Secondly, the accumulated dispersion throughout the fiber distorts the transmitted signal. Next, the signal is polluted by the Local Oscillator (LO) LPN, on the optical to electrical conversion. Finally, the CD effect is corrected by Chromatic Dispersion Equalization (CDE). Only then does the signal go through CPE. Now, having seen how CDE operates in Chapter 2, we know it is obvious that even the ideal CDE cannot properly remove the impact of CD. That is because, even though the CD effect could be properly corrected, the zero-forcing CDE does not take into account the added LPN between the dispersion accumulation and respective equalization.

The objective of this chapter is to describe and explore a new approach to subcarrier joint processing CPE techniques, one that takes into account the effect of CD on the overall estimated LPN, according to the diagram in Figure 5.1. In Section 5.1 this algorithm is explained, alongside with the mathematical properties that back it up. Then, on Section 5.2 its performance is assessed. Finally, in Section 5.3 an additional advantage brought by this algorithm is explored and assessed.

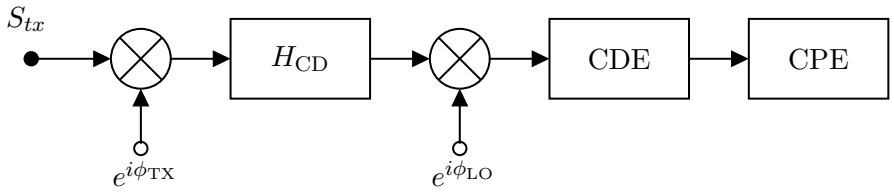

Figure 5.1: Simplified block diagram of the effects that are relevant for joint processing CPE in the presence of CD.

5.1 Dual-Reference Subcarrier CPE Algorithm

On Back-to-Back (B2B) scenarios and low transmission distances, the existence of two separate LPN Wiener processes at two different instances may not seem like a problem. They can be even considered as one. given that the sum of two Wiener processes is a Wiener process (as studied in Section 2.2). However, Group-velocity Dispersion (GVD) makes the existence of those two independent LPNs not trivial to solve. Each frequency of the channel will be transmitted at the same time, but travels at a different group velocity on the fiber, arriving at different instances to the receiver. This causes each frequency to be affected by a different overall LPN, resulting from the sum of two Wiener processes shifted differently in time. The ultimate proof that this time difference between LPNs cannot be disregarded is that, even when a perfect CDE is assumed (which is the case of our simulated results), the accumulated CD imposes an SNR penalty in joint processing CPE techniques that is, in the limit, as bad as the penalty felt on the wideband single-carrier system.

Let us now consider narrow-band subcarriers (such that we can ignore intra-subcarrier CD effects) and an ideal CDE. In this scenario, all subcarriers will have been perfectly aligned to the transmitter's side, and, each subcarrier is affected by an overall LPN that can accurately be described by a linear combination of the LPN contributions of the transmitter's and of the LO's LPN, ϕ_{TX} and ϕ_{LO}, respectively. The following expression represents the LPN affecting subcarrier n:

$$\phi_{\mathrm{PN},n}(t) = \phi_{\mathrm{TX}}(t) + \phi_{\mathrm{LO}}(t - (n-1)\Delta T_{\mathrm{CD}}), n \in 1, 2, ..., N_{\mathrm{SC}} \tag{5.1}$$

In the expression, ΔT_{CD} represents the already described time delay between two consecutive subcarriers of the optical channel. We have now established, in expression (5.1), that the affecting LPN can no longer be considered the same for all the subcarriers. Any step towards the realization of an effective jointly processed CPE on this scenario must take into consideration the distributed (transmitter and LO) origin of LPN. After CDE, all subcarriers have a common contribution of ϕ_{TX} on ϕ_{PN} but a different one of ϕ_{LO}. This means that the best approach is to estimate both ϕ_{TX} and ϕ_{LO} separately, and only then properly combine them to correct the impact of LPN in each subcarrier. This reduces the problem of estimation of N_{SC} different LPNs to the collaborative estimation of two LPNs.

Considering we now focus our attention simply on two reference subcarriers, SC_m and SC_n, whose LPN estimates, $\hat{\phi}_{\mathrm{PN},m}$ and $\hat{\phi}_{\mathrm{PN},n}$, are considered to be precise, let's

take a look at what happens when we subtract one by the other.

$$\begin{aligned}\hat{\phi}_{\mathrm{PN},m}(k) - \hat{\phi}_{\mathrm{PN},n}(k) &= \phi_{\mathrm{LO}}(kT_s - (m-1)\Delta T_{\mathrm{CD}}) - \phi_{\mathrm{LO}}(kT_s - (n-1)\Delta T_{\mathrm{CD}}) \\ &= \Delta\phi_{\mathrm{LO}}(k, \Delta T_{\mathrm{CD}})\end{aligned} \tag{5.2}$$

We have thus successfully managed to isolate the LO LPN component from the one of the transmitter. In this expression, $\Delta\phi_{\mathrm{LO}}$ represents nothing more than the change in ϕ_{LO} in the last $|(n-m)\Delta T_{\mathrm{CD}}|$ seconds. This can be somewhat mesmerizing, since **we are doing an estimation of a phenomenon, ϕ_{LO}, in two different moments based on two signals sampled at the same time**, $\hat{\phi}_{\mathrm{PN},m}(k)$ and $\hat{\phi}_{\mathrm{PN},n}(k)$. This is only possible thanks to the delays imposed by CD. So, the problem brought by CD, also provides an elegant way to solve it.

Now, aiming to achieve the regeneration of ϕ_{LO} from $\Delta\phi_{\mathrm{LO}}$, let us take as a starting point the mathematical formulation of a discrete first order integral of a signal $S(k)$:

$$S(k) = \sum_{j=1}^{k} S(j) - S(j-1) + S(0) \tag{5.3}$$

We are able to see that, to fully reconstruct $S(k)$, all we need to have is its the evolution in each symbol period and its value at the initial moment. Now, coming back to our problem at hands, what we have is not the evolution of ϕ_{LO} in the last symbol period, but rather its evolution on the last $|(n-m)\Delta T_{\mathrm{CD}}|$ seconds. The evolution of ϕ_{LO} at each symbol period can thus be approximated by:

$$\phi_{\mathrm{LO}}(k) - \phi_{\mathrm{LO}}(k-1) = \Delta\phi_{\mathrm{LO}}(k, \Delta T_{\mathrm{CD}}) \cdot \alpha, \tag{5.4}$$

with α being an adjustment factor given by:

$$\alpha = \frac{T_s}{|(n-m)\Delta T_{\mathrm{CD}}|} \tag{5.5}$$

It shall be noted that this approximation corresponds to the assumption that ϕ_{LO} had a linear behavior in the $|(m-n)\Delta T_{\mathrm{CD}}|$ seconds before each moment k, which means that the performance of this algorithm may have a dependency on the ratio $T_s/|(n-m)\Delta T_{\mathrm{CD}}|$.

Continuing the analysis, an expression for $\hat{\phi}_{\mathrm{LO}}{}'$ can now be built:

$$\hat{\phi}_{\mathrm{LO}}{}'(k) = \sum_{j=1}^{k} \Delta\phi_{\mathrm{LO}}(j, \Delta T_{\mathrm{CD}}) \cdot \alpha + \phi_{\mathrm{LO}}(0) \tag{5.6}$$

We have not yet discussed the value of $\phi_{\mathrm{LO}}(0)$, but let us delay the analysis of it for later, and assume we have it for now. Having $\hat{\phi}_{\mathrm{LO}}{}'$, our goal is now to obtain an estimate for ϕ_{TX}, $\hat{\phi}_{\mathrm{TX}}$. Considering that both $\hat{\phi}_{\mathrm{PN},m}$ and $\hat{\phi}_{\mathrm{PN},n}$ contain the same synced contribution of ϕ_{TX}, the best approach for its recovery is to remove a version of ϕ_{LO} properly aligned in time from both of these signals and average the result. Aligning the $\hat{\phi}_{\mathrm{LO}}$ in time consists of adding or removing delays that are a function of α, which, in this context, can be seen as the number of samples that pass before the effects of ϕ_{LO} measured in one of the reference subcarriers are measured on the other reference subcarrier.

Having estimated $\hat{\phi}_{\mathrm{TX}}$, it can now be assumed that it is a better estimate of ϕ_{TX} rather than $\hat{\phi}_{\mathrm{LO}}$ is of ϕ_{LO}, because it results of the average between two different LPN estimates. Under that assumption, we can do the inverse of the last steps, to obtain a second, refined, estimate of ϕ_{LO}, $\hat{\phi}_{\mathrm{LO}}$, from the subtraction of $\hat{\phi}_{\mathrm{TX}}$ from both estimates $\hat{\phi}_{\mathrm{PN},m}$ and $\hat{\phi}_{\mathrm{PN},n}$. Again, these steps can be repeated in an improvement loop, to better estimate ϕ_{TX} with the improved estimate of ϕ_{LO} and so on and so forth. There is no need to worry about the improvement loop worsening the estimates, considering that in every iteration we start from the same solid $\hat{\phi}_{\mathrm{PN},m}$ and $\hat{\phi}_{\mathrm{PN},n}$ estimations. A diagram of this algorithm can be seen in Figure 5.2.

Concerning the value of $\phi_{\mathrm{LO}}(0)$, we can now realize that it is not significant, because the initial phase, being a constant, can either be considered to be part of ϕ_{TX} or ϕ_{LO}. What is critical about the LPN is not the initial value, but rather it's evolution throughout time, and the accuracy with which it is estimated. Now, after obtaining an estimate for both, we must combine them according to Equation (5.1), as can be observed in Figure 5.3.

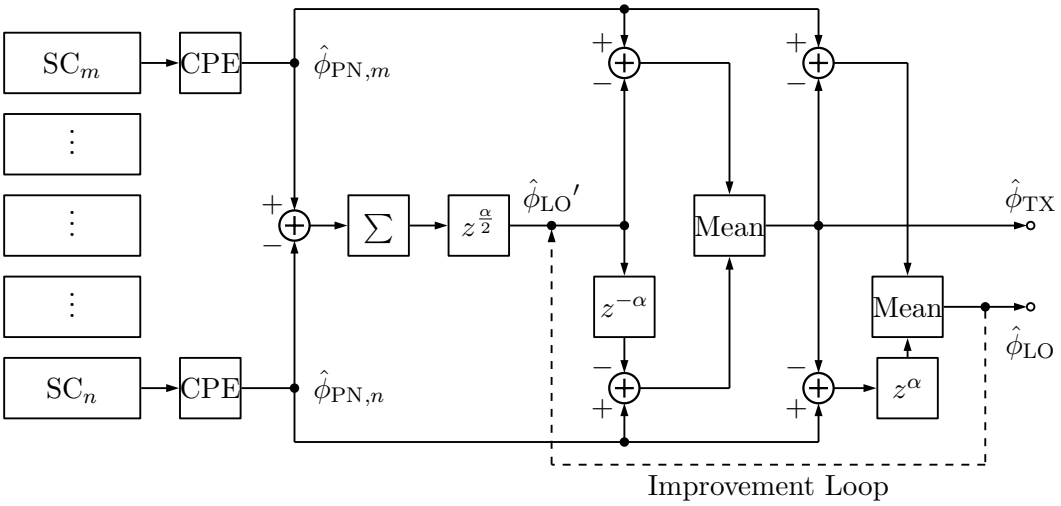

Figure 5.2: Block diagram of the DRS algorithm.

Another interesting usage of this approach is that we can now separately estimate the Laser Line Width (LLW) of both transmitter and LO lasers, performing a trivial manipulation of the expression (2.15), in the following way:

$$\Delta f_{\mathrm{TX,LO}} = \frac{\sigma^2_{tx,lo}}{2\pi T_s} \tag{5.7}$$

This allows for an unprecedented ability for constant monitoring of the state of both lasers without any significant additional complexity.

Henceforward, this algorithm will be designated as Dual-Reference Subcarrier (DRS) for basing all its phase correction simply on the usage of two reference subcarriers.

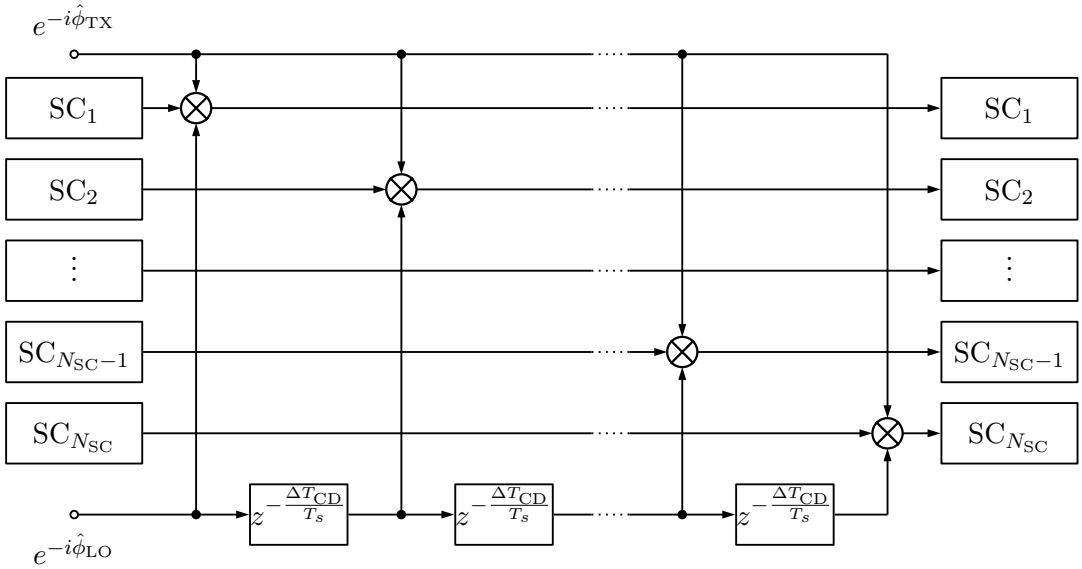

Figure 5.3: Assembly of the contributions of ϕ_{TX} and ϕ_{LO} for proper phase noise correction in the several subcarriers.

5.2 Performance Assessment

The presented algorithm requires, as the name implies, the election of two reference subcarriers. As in every other example on this work, we need to establish a fair comparison with the scenarios studied previously, thus, an overall Pilot Rate (PR) of 31/32 must be used. To calculate the equivalent PR on each reference subcarrier, the following expression can be used:

$$R_{\mathrm{P}ref} = 1 - \frac{N_{\mathrm{SC}}}{2} \cdot (1 - R_{\mathrm{P}}) \tag{5.8}$$

Doing basic replacements on the formula, we can see how, for R_{P}=31/32, this approach is limited to a scenario with N_{SC}=64, because in that case all symbols on the reference subcarrier are pilot symbols and no superior pilot rate can be achieved when using two reference subcarriers only. So far, we have addressed the need for the usage of two reference subcarriers, and we have now defined their respective PR. We shall now define the criteria on how to choose the two reference subcarriers among the pool of N_{SC} subcarriers. As a starting point, it is important to evaluate if the performance is independent of the two elected subcarriers or not. With that goal in mind, simulations were performed to estimate the required SNR as the separation between subcarriers increased. Figure 5.4 shows the results of such simulations, displaying the required SNR to achieve the target NGMI as a function of the normalized separation between reference subcarriers for different values of N_{SC}. The Normalized Separation between reference subcarriers (NS) is calculated as:

$$\mathrm{NS} = \frac{|n - m|}{N_{\mathrm{SC}}}, \tag{5.9}$$

with m and n being the indexes of the reference subcarriers. They were obtained for a transmission length of 2000 km and LLW of 1 MHz, and, for the moment, it is assumed that the optimization of the separation parameter is not dependent on the chosen L

and LLW. We are able to see how the performance really worsens when the two chosen reference subcarriers are adjacent/near each other. This performance decrease can be attributed to the fact that for subcarriers whose center frequency is closer the affecting overall LPN is more similar, mining the performance of the algorithm, once it is based on the difference between the affecting LPN on both reference subcarriers, caused by the variable delay between the addition of ϕ_{TX} and ϕ_{LO}. Now, assessing the larger reference subcarrier separations, we can see how they also do not represent the peak of performance, leading us to conclude that there is yet another important factor at play, besides the difference between the phase shifts affecting each subcarrier, because if that were not the case, the best performance would be measured at the case in which the subcarriers of reference were the ones on the extreme of the optical channel, maximizing the difference between the group velocity of each constituting frequency component of the transmitted signal. To conclude the analysis of the separation of the two elected reference carriers, let us consider as an optimum separation the one that corresponds to half the number of subcarriers of the system. This performance maximization makes sense for two main reasons: i) because it represents the point at which the reference subcarriers are separated enough to be able to have estimates of LPN in which the LO contribution is significantly displaced; ii) because the error on the LPN estimation is minimized when the distance between each subcarrier and the closest reference subcarrier is also minimized. In Figure 5.5, this latter point is put in evidence, for the case of N_{SC}=32. While the reference carriers have equivalent Normalized GMI (NGMI) values, their choice of positioning affects the NGMI of the neighbor subcarriers, and the NGMI decreases with the increase of the distance to the reference subcarriers. This dependence on the effectiveness of the CPE on the distance to the reference subcarrier suggests an imbalance on the separation of ϕ_{TX} from ϕ_{LO}, thus why, for closer subcarriers, the performance is better, because the components of ϕ_{LO} that were estimated as being part of ϕ_{TX} are still temporally aligned close to ϕ_{LO}, when the overall LPN affecting each subcarrier is constructed from $\hat{\phi}_{\mathrm{TX}}$ and $\hat{\phi}_{\mathrm{LO}}$. Furthermore, this suggests that, to fight the performance decrease caused by the LPN correction on the subcarriers that are distant to the reference subcarriers, one alternative approach could be taken, in which the Multi-Subcarrier (MSC) channel was divided into two sub-bands, and, in each of the two sub-bands, the DRS algorithm would be applied separately, each with two reference subcarriers.

The default performance results assessed hereby on will be done assuming the optimum reference subcarrier separation, that is, using the subcarriers m and n, mathematically formulated as:

$$m = \frac{N_{\mathrm{SC}}}{4} + 1 \qquad\qquad n = \frac{3N_{\mathrm{SC}}}{4} - 1 \tag{5.10}$$

However, it is important to mention that, in practical implementations, there might come gain from the placement of the reference subcarriers on the extremes of the optical channel, that is to say m,n = 1,N_{SC}. This gain is envisaged due to the fact that pilot symbols are always inserted on a Quadrature Phase Shift Keying (QPSK) constellation and thus require less SNR, thus minimizing the impact of the effect of optical filtering on the outer frequencies of the optical channel.

Having established the optimum separation between the two reference subcarriers on the DRS algorithm, only one other thing is missing to fully establish how the algorithm

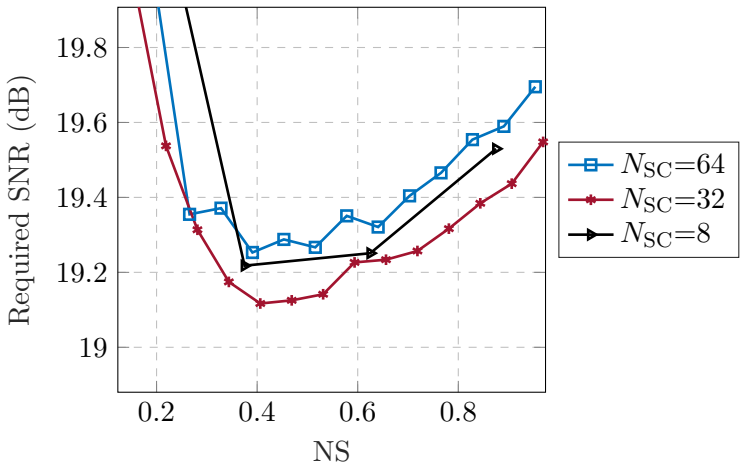

Figure 5.4: Required SNR as a function of the Normalized Separation between reference subcarriers (NS).

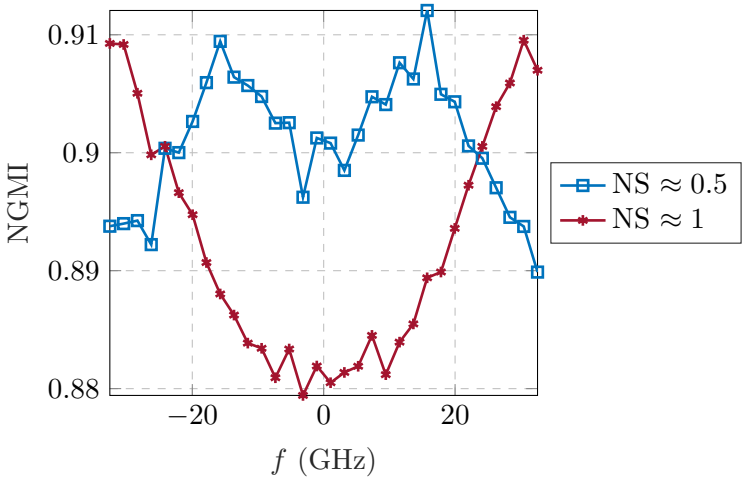

Figure 5.5: NGMI measured in each of N_{SC}=32 subcarriers, after the DRS-CPE, for two different values of NS between reference subcarriers, with a fixed SNR=19.15 dB.

should be employed for the best performance: the ideal number of iterations on the improvement loop suggested on the algorithm description. Figure 5.6 displays those exact results, evaluated for two different scenarios, a first scenario with a normalized separation of approximately 0.5, which was the one already identified as optimal, and a second one, with a normalized separation close to 1, which, while sub-optimal, may have interest on practical implementations, as pointed out above. These results were obtained for N_{SC}=32 and, similarly to the ones above, a transmission length of 2000 km and a LLW of 1 MHz. We are able to see that, for the optimal normalized separation, no improvement is seen by performing more than one iterations of the algorithm. For that reason, on the following results, only a single iteration is considered. However, for the scenario in which the reference carriers are on the extremes of the optical channel, a gain of 0.2 dB can be achieved after 3 iterations. This leads us to conclude that the usage of iterations on the algorithm may present gain when a sub-optimal reference subcarriers

separation is used.

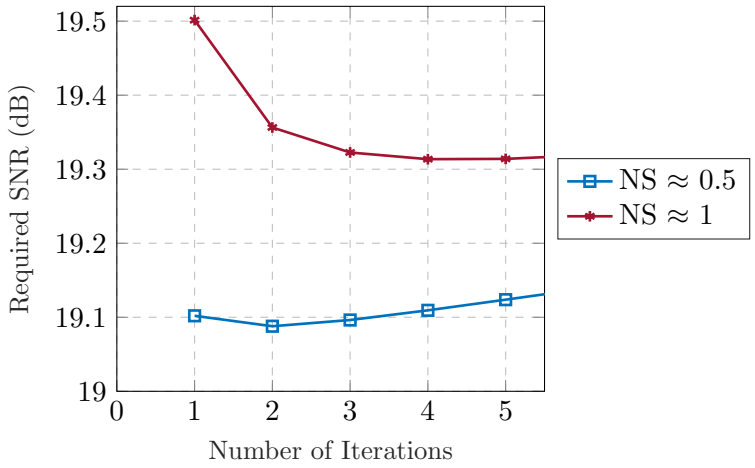

Figure 5.6: Required SNR as a function of the number of improvement iterations, for two different normalized separations (NS).

At this point, we are finally ready to assess how the DRS algorithm performs in comparison with other CPE approaches. Figure 5.7 shows a LLW sweep for a fixed transmission length of 2000 km. We present the results of DRS for 2, 4, 8, 32 and 64 subcarriers. They are compared against the best approach up until now on this type of LLW sweep, which was the approach with 4 subcarriers, independently processed Pilots and Blind Phase Search (BPS), seen on Section 3.4. Only the performances of the algorithm for 2 and 4 subcarriers were not able to outperform the scenario with pilots and BPS, but this was already expected, because, for these numbers of subcarriers, Equalization-Enhanced Phase Noise (EEPN) has an impact on the performance of CPE algorithms. Now, let's focus our attention on the performances of DRS for N_{SC}=8, 32, 64, the ones that do outperform our best scenario. While they do not significantly outperform it, it is really important to bear in mind that these results were achieved without the usage of BPS, meaning that there was only one stage of CPE, and thus a significant reduction on the complexity of the overall CPE for the same performance.

Let's now perform a distance sweep, for a fixed LLW of 1 MHz, to analyze the dependence of our proposed algorithm to the increase of accumulated CD. Figure 5.8 shows these results. Some results of interest are also shown for the use of independently processed Pilots and Pilots alongside with BPS. Starting our analysis on the results only resorting to Pilots, we can see how up until 1500 km 2 subcarriers are the ones with the best performance. After that, the accumulated CD makes 4 subcarriers the best choice, until around 4250 km, and then 8 subcarriers are the best. Note that, while with 16 subcarriers the performance is worse than with any of the above, it is also the one with the smaller slope, once again emphasizing the tolerance to CD brought by narrow spectra. Now, adding to the CPE the second stage of BPS, the best performance is for a system with 4 subcarriers with a transmission length of up to 2750 km, and then, for longer distances, the best is to change to a system with 8 subcarriers. We have successfully analyzed the best performances known so far, and we can see a clear disadvantage: the number of subcarriers of the MSC system has to be changed as a function of the intended transmission distance, if we are aiming at the best possible performance. On

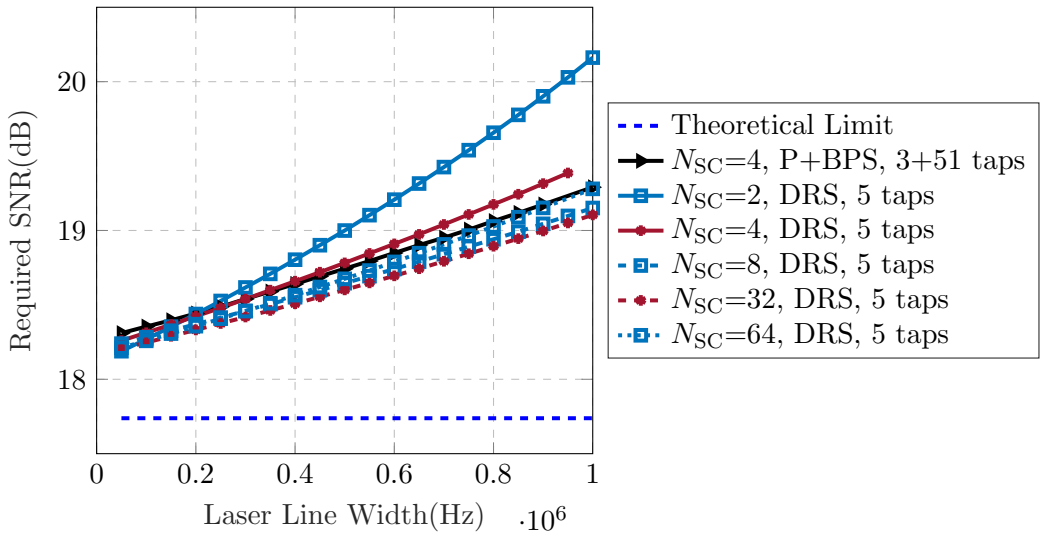

Figure 5.7: DRS performance for a fixed L=2000km and a varying LLW.

the other hand, analyzing the results of the DRS algorithm, we see that it presents a performance better than any other approach for a wide transmission range as well as for a variable number of subcarriers. This means that whether we want to opt for a system with 8, 32, or 64 subcarriers, and for any length between 500 to 5000 km, DRS is always the best choice. All this, without the added complexity brought by a BPS stage. One important thing to note at this point is also that this is the only method that enables the usage of systems with either 32 or 64 subcarriers with very low SNRs, all thanks to the success on implementing an unprecedented joint processing CPE technique that is tolerant to the CD. This algorithm can remove the limit to the choice of the number of subcarriers that first was made difficult by the carrier phase tracking point of view.

One interesting thing to analyze concerning the DRS algorithm is to measure quantitatively the impact of assuming that with only two reference subcarriers we can match the performance of having all subcarriers with the same pilot rate as in those two reference carriers. In other words, this corresponds to quantifying the error on the estimation of the LPN suffered on non-reference subcarriers. For that analysis, let's look at Figure 5.9, where the numerical results that measure that impact are displayed. For the results on the picture, a fixed LLW of 1 MHz was considered and the curves for the Pilots algorithm (non-DRS) have a PR equal to the one on the reference subcarriers, but CPE was independently processed, therefore corresponding to a much lower overall pilot-rate of $1 - N_{SC}/64$ Note again that, although this comparison is not fair from a practical point of view (huge imbalance on the overall pilot-rates), it serves the purpose of exposing the possible sources of the reminiscent penalty associated with the DRS algorithm. This way we can properly assess how good is the LPN estimate on each of the reference subcarriers, and understand if we can properly reconstruct the LPN affecting each subcarrier. We can see how this assumption never imposes a penalty larger than 0.2 dB for transmission distances below 2000 km, meaning that the extraction of both the ϕ_{TX} and ϕ_{LO} and subsequent reconstruction of the LPN affecting each subcarrier is properly achieved, matching the LPN resistance that would have been made possible with independent processing and a higher number of Pilots on all the subcarriers. For

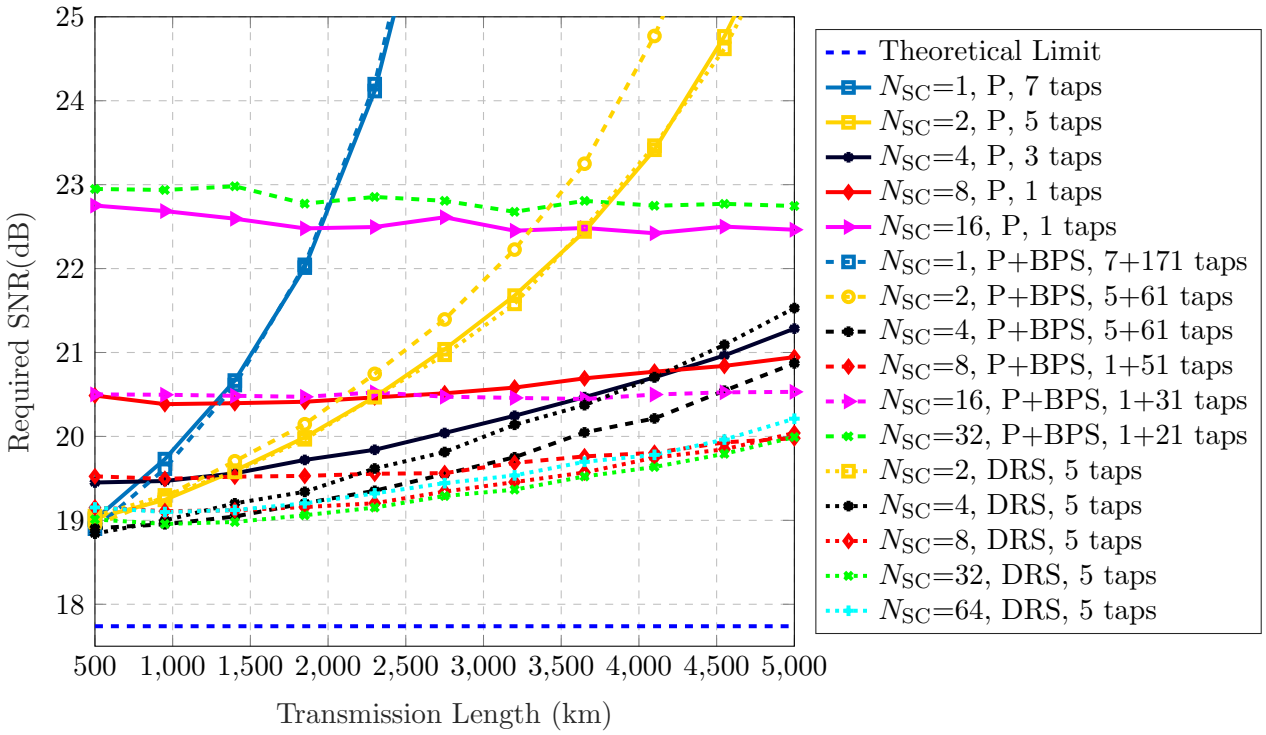

Figure 5.8: DRS performance for a fixed LLW=1 MHz and a varying transmission length.

longer transmission lengths, however, these results degrade significantly, meaning that the reconstruction of LPN is not so perfect, but it should be kept in mind that DRS still represents the best option without adding any overhead nevertheless.

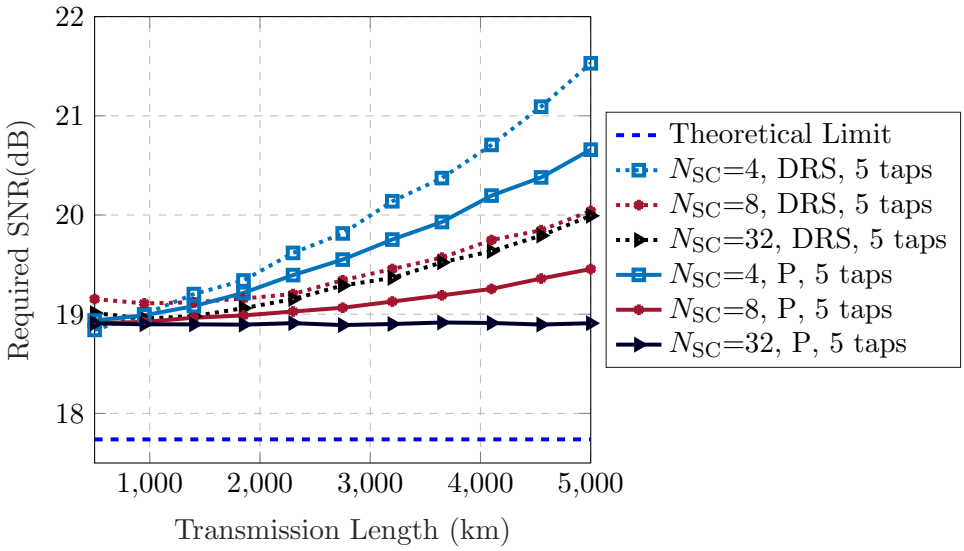

Figure 5.9: Comparison between DRS performance vs. independent subcarrier processing with an equal PR.

Further extending our analysis on the results of Figure 5.9, we can see how, for N_{SC}=32, the equivalent PR can effectively present total independence of the transmission length for the lengths considered. This is a very important conclusion, because now we know that the performance degradation of the DRS algorithm is not due to the bad estimation of the LPN impacting both reference carriers, but rather on the algorithm that derives both $\hat{\phi}_{TX}$ and $\hat{\phi}_{LO}$ itself. This demands for a revision on the algorithm, to better understand the origin of this performance degradation. Namely, we must focus on the parts of the algorithm that would be distance-dependent. This narrows our options to a single factor, the adjustment factor, α, described on expression (5.5). When first introduced, we mentioned how the usage of this factor imposed an approximation on the estimate of the value of ϕ_{LO}. Let's recall how the value of α was calculated:

$$\alpha = \frac{T_s}{|(n-m)\Delta T_{CD}|} \tag{5.11}$$

In fact, looking at its formulation, it becomes obvious that this value has a filtering effect, and $1/\alpha$ corresponds to the number of symbols through which an estimation on the value of LO is spread. Let us now match the value of $1/\alpha$ with the performance of DRS for the scenario of N_{SC}=32, and see if any conclusions can be derived, Figure 5.10 serves that purpose, and it confirms our suspicions, α imposes a penalty on the performance of the DRS algorithm as soon as the spreading it causes surpasses the spreading imposed by the optimum number of taps. Now, can this problem be solved? Or is the value of α fixed for a given scenario? Well, in fact, it can!

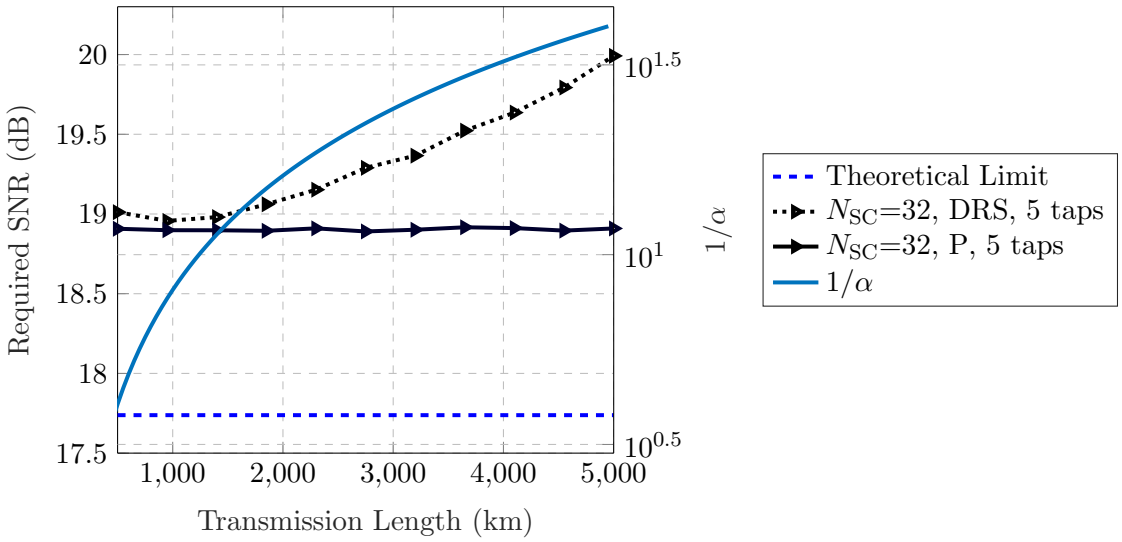

Figure 5.10: Relation between the ideal performance of DRS and the value of α.

We know that the value of α depends on the separation of the two reference subcarriers, m and n, so, if we decrease the separation between them, we will be matching the spreading imposed by the number of taps, further increasing the performance for longer transmission lengths. This has, however, the penalty of the normalized separation between reference subcarriers no longer being the optimum, the one that minimizes the distance between any subcarrier and the reference subcarrier. But we know from the results in Figure 5.4 that we still have a safe margin to decrease the separation between

the reference subcarriers without it presenting a significant impact on the required SNR. In 5.11 the performance for DRS is assessed with a variable and optimized value of α, by varying the distance between the reference subcarriers. These results are plotted alongside with the previous results for N_{SC}=32 in Figure 5.9. At a transmission length of 5000 km, the gain by optimizing the distance on the reference subcarriers is around 0.6 dB, and there's a visible reduction on the slope of the overall DRS optimized curve. However, there's still a significant penalty from the ideal results in which all subcarriers have an equivalent PR, but this is due to the fact that the choice of the separation between reference subcarriers is a compromise between two factors, the value of α and the position of the reference subcarriers that minimizes the distance from the reference subcarriers to the non-reference ones.

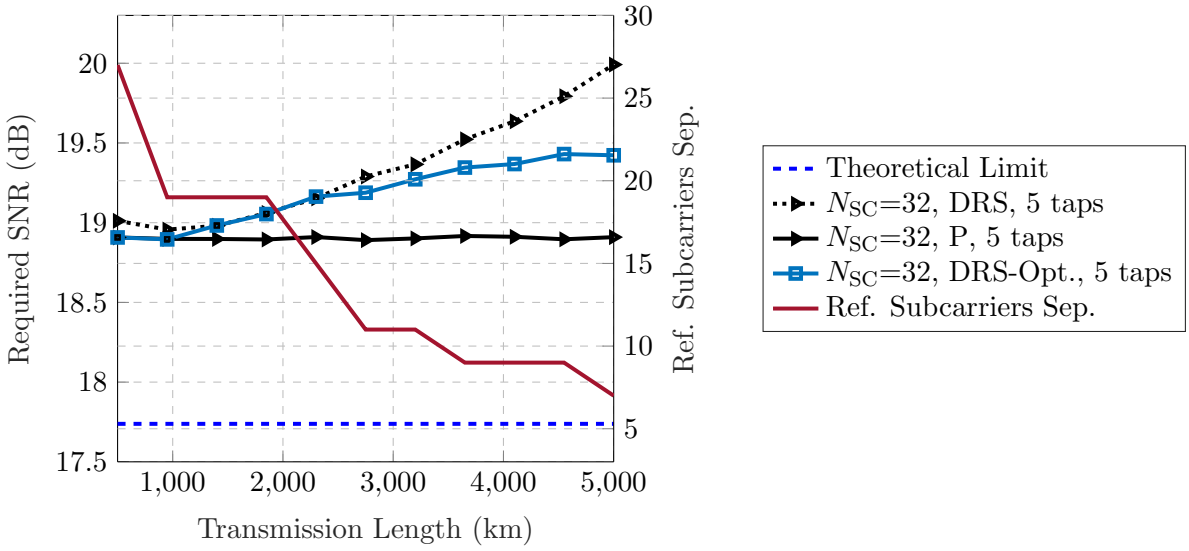

Figure 5.11: Performance of the DRS with Optimized Distance between Reference Subcarriers (DRS-Opt.), and respective values of the optimum distance between reference subcarriers.

Table 5.1 shows the equivalent inter-symbolic spread as a function of the optimum separation between reference subcarriers. The performance of the DRS matches the ideal performance of the system with the equivalent PR in all subcarriers when the inter-symbolic spread caused by α is smaller than the one imposed by the number of taps. As the accumulated CD increases, the separation between reference subcarriers has to decrease, to maintain the value of $1/\alpha$ low. However, it can't be the lowest, because the lowest would imply that the maximum distance from a reference subcarrier to any non-reference subcarrier would be too large. The optimum performance is measured when the sum of the impact of these two factors is minimized.

L (km)	Opt. Ref. Subcarriers Sep.	$1/\alpha$
500	27	7.3
950	19	9.7
1400	19	14.3
1850	19	18.9
2300	15	18.6
2750	11	16.3
3200	11	18.9
3650	9	17.7
4100	9	19.9
4550	9	22.0
5000	7	18.8

Table 5.1: Corresponding values of $1/\alpha$ for the optimum reference subcarriers separation, as a function of the transmission length.

5.3 Digital Monitoring

The topic to be explored, as the section title implies, is digital monitoring, namely the digital monitoring of the state of both lasers.

Making use of the proposed dual-reference subcarrier algorithm, this section addresses the digital monitoring of LPN in intradyne coherent optical transmission systems. While the monitoring of the overall combined laser phase noise is an inherent feature of any digital CPE algorithm, the ability of separately monitoring the transmitter and receiver lasers without modifying or even disrupting the communication has not yet been demonstrated, to the best of our knowledge. This is a unique feature of the DRS algorithm, which, within its process of phase estimation, inherently implies the separation of the two LLW sources. More importantly, this capacity is added without any significant complexity added to the system.

Before moving to the in-depth analysis and the details of LLW measurements, it is interesting to have a visual aid on how exactly is the LPN reconstructed for each of the lasers. Figure 5.12 shows the resulting estimates of both ϕ_{TX} and ϕ_{LO}, for a particular test with N_{SC}=32, L=2000 km, SNR=19.5 dB, 5 taps on the DRS algorithm and $\Delta f_{\mathrm{TX,LO}}$=500 kHz. We can see a very close overlap between the real noise and the estimate on both phenomena. For a qualitative evaluation, the Normalized Mean Square Error (NMSE) is also presented, having a value below 2 % on both.

With the promising results in Figure 5.12, we can move on to the next step, reaching a numeric estimate for the LLWs. In Section 5.1 an expression was derived that established a direct relation between system parameters, the variance of the Gaussian variable that best models the LPN and the respective LLW. Let's remember that expression:

$$\Delta f_{\mathrm{TX,LO}} = \frac{\sigma^2_{tx,lo}}{2\pi T_s} \tag{5.12}$$

Still using the same simulation scenario as for the last figure, we can directly apply expression (5.12) to estimate the LLWs. The only thing we need to obtain that we don't inherently have on the system is $\sigma^2_{tx,lo}$. Recalling Section 2.2, we saw how it could

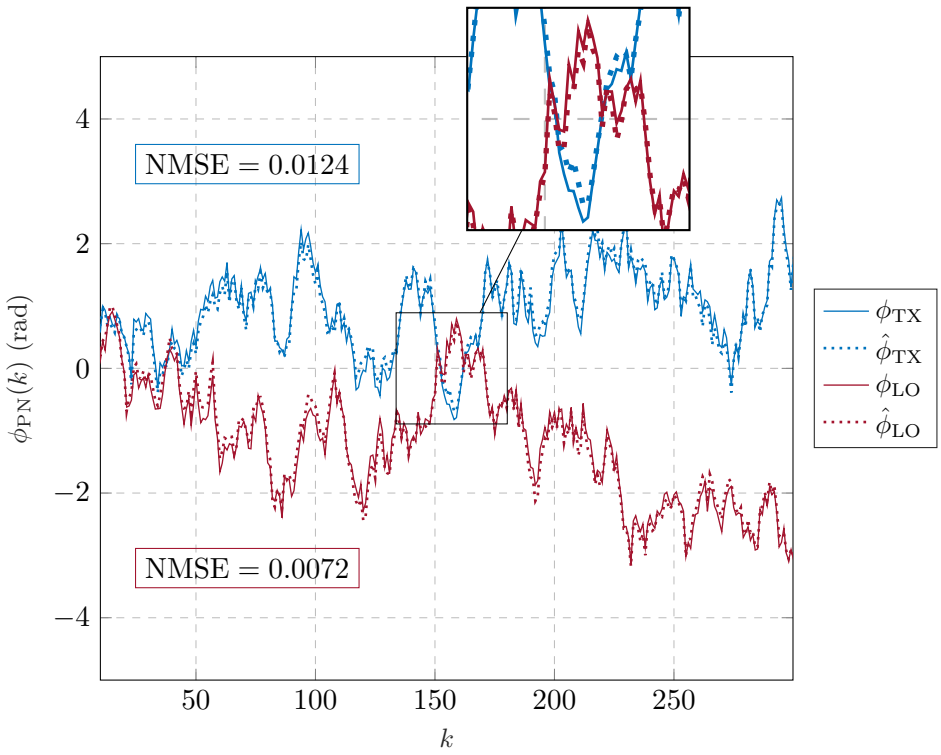

Figure 5.12: Relation between ϕ_{TX} and $\hat{\phi}_{\mathrm{TX}}$, and between ϕ_{LO} and $\hat{\phi}_{\mathrm{LO}}$, with N_{SC}=32, L=2000 km, SNR=19.5 dB, 5 taps on the DRS algorithm and $\Delta f_{\mathrm{TX,LO}}$=500 kHz.

be modeled as a Wiener process, in which each temporal transition during a time of sampling, T_s, was well modeled by a Gaussian variable of variance $\sigma^2_{tx,lo}$. Thus, to see how to obtain this value, let's remember how is the variance of a process calculated. Given a signal x, whose average value is μ_x, it's variance is given by:

$$\sigma^2 = \mathrm{E}\{x^2 - \mu_x\} \tag{5.13}$$

where $\mathrm{E}\{\cdot\}$ denotes the expected value of the signal. Given that the Gaussian variable that models the cumulative evolution of LPN has a zero mean value, its variance corresponds simply to the variables mean squared value. Now it's obvious that for properly estimating its variance we need many samples of this Gaussian variable, to have a precise estimate. But, how many samples? In [66], an expression is derived to assert a lower bound for the sampling size, N, given a desired confidence interval, $100(1-\rho)\%$, a predicted variance, σ^2 and an error margin, E:

$$N \geq \left\lceil \frac{z^2_{\rho/2}\sigma^2}{E^2} \right\rceil, \tag{5.14}$$

where $z_{\rho/2}$ is the commonly called *z-score*, which represents the number of standard deviations required around the mean value of a variable to assure with a $100(1-\rho)\%$ certainty that a variable sample is in the interval $[\mu - \sigma z_{\rho/2}, \mu + \sigma z_{\rho/2}]$. Fixing a confidence interval of 99%, corresponding to a z-score of approximately 2.576, and a maximum margin of error of 5%, and an upper bound for the variance equivalent to a LLW of

1 MHz, we obtain, for our simulation scenario:

$$N \geq \left\lceil \frac{2.576^2 (2\pi \frac{N_{\mathrm{SC}}}{64\mathrm{e}9} 1\mathrm{e}6)^2}{0.05^2} \right\rceil \simeq 9 \tag{5.15}$$

We would only need as little as 9 measurements of the LPN transitions to effectively estimate their variance. It is also important to emphasize that on our LPN estimates, a sample of the Gaussian variable corresponds to the difference between two consecutive samples. Having established how to calculate the values for $\Delta f_{\mathrm{TX,LO}}$, these were the practical results of such calculus, for the scenario of Figure 5.12, using a $N >> 9$:

$$\hat{\Delta f}_{\mathrm{TX}} \approx 78\,\mathrm{kHz} \qquad\qquad \hat{\Delta f}_{\mathrm{LO}} \approx 47\,\mathrm{kHz}$$

These values are obviously both very far from the real value, which, as we've mentioned, is 500 kHz for both lasers. Now, why does that happen? If the noise seems to be well reconstructed, why would the theoretical expression for the mathematical model not be directly applicable? The reason behind this mismatch is the low-pass filtering to which the estimates of the LPN are subject to. This filtering is caused by the usage of a number of taps and by the inter-symbolic spread caused by CD, which create an error on the estimate of the variance of the Gaussian variable responsible for the LPN evolution. To mitigate the error associated with this filtering, we have to slightly adapt expression (5.12). So, if instead of considering an LPN transition between two consecutive we consider the transition between a longer time interval, the effect of filtering will be relatively smaller, because filtering only affects quick transitions, due to its low-pass nature. Doing so will not affect the estimation of the LLW, thanks to the properties of Wiener processes, being them a fractal process. All we have to do to maintain the validity of expression (5.12) is to adjust T_s to the number of samples analyzed as one. This gives origin to the new expression to estimate LLW, given by:

$$\Delta f_{\mathrm{TX,LO}} = \frac{\sigma^2_{tx,lo;n}}{2\pi n T_s} \tag{5.16}$$

in which n is a natural integer that corresponds to the number of samples considered together as a unitary transition of the LPN and $\sigma^2_{tx,lo;n}$ is the variance obtained from the respective n-units transitions. This can be interpreted as a jump of n samples, in a time interval of nT_s. We have speculated on how, with longer samples jumps we would eventually mitigate the effect of the LPN filtering, and build up a good estimate of the LLW. Thus, let's see, still for the same simulation scenario, how does the LLW estimate evolve as a function of n. Figure 5.13 shows that same evolution. In the figure, we can observe how, in fact, for small values of n we cannot perform anywhere near a good estimate of the LLWs, however, any arbitrarily large value for n seems to lead to a good estimate for the value of LLW.

One question that can arise from the analysis of Figure 5.13 is: if the only effects that lead to a bad estimate of the value of the LLW are the number of taps and the pulse broadening caused by CD, both dependent of the symbol period, why does the estimate seem to start worsening again for higher values of n? Well, this has to do with the minimum required sample size. Increasing n has an important impact on the value

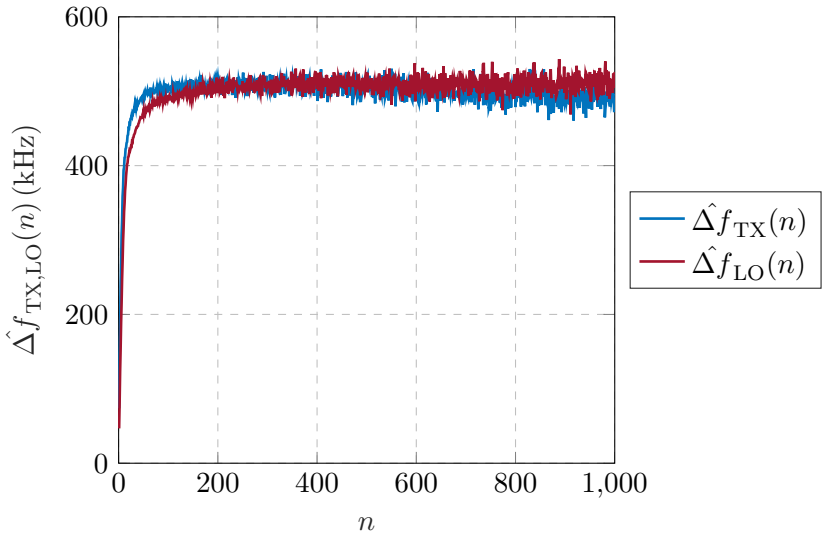

Figure 5.13: Estimation of $\Delta f_{\mathrm{TX,LO}}$ with the evolution of n, with N_{SC}=32, L=2000 km, SNR=19.5 dB, 5 taps on the DRS algorithm and $\Delta f_{\mathrm{TX,LO}}$=500 kHz.

of N. On the one hand, it increases the variance of the LPN, because the variance is a function of the period of time between LPN estimates. And, on the other hand, it decreases the number of samples available, considering that n samples are taken as one. Both these facts increase the value of N. This would not be a problem for practical implementations, since LLW can be considered as quasi-invariant over time, thus we would have virtually infinite samples to perform the assessment of the LLW. However, it poses a problem for simulated environments, where it is not feasible to perform very long simulations in a timely manner. Since we are working on a simulated environment, it is thus important to define an intermediate value of n, one that assures the mitigation of the impact caused by LPN filtering but simultaneously still fulfills the sampling size condition seen on expression (5.14), because we want to achieve confident estimates with minimal error.

Moreover, we need to analyze how does the minimum required n changes with N_{SC} and with the values of LLW. Figure 5.14 shows the same study but with the added results for both 8 and 64 subcarriers. Note that in a simulation environment, an increase in the number of subcarriers results in a decrease in the number of samples of the LPN, for a fixed overall number of simulated symbols. Consequently, we observe some impact on the precision of the estimate of the LLW, because, for the case of N_{SC}=64, the sample size required is only met for values of n at which the estimate of the value of LLW has not yet converged.

Figure 5.14 also shows a dependence of N_{SC} on the minimum value of n required, higher values of N_{SC} require smaller values of n. Just before we claimed that the bad assessment of the value of the LLW for samples of LPN close to one another was simply because of the filtering of the number of taps and of the pulse broadening caused by CD. If this is true, we should be able to attain total independence of the results from the number of subcarriers if we replace n by an n', which would correspond to a jump corresponding to the sampling period of the LPN, which is a function of the pilot-rate

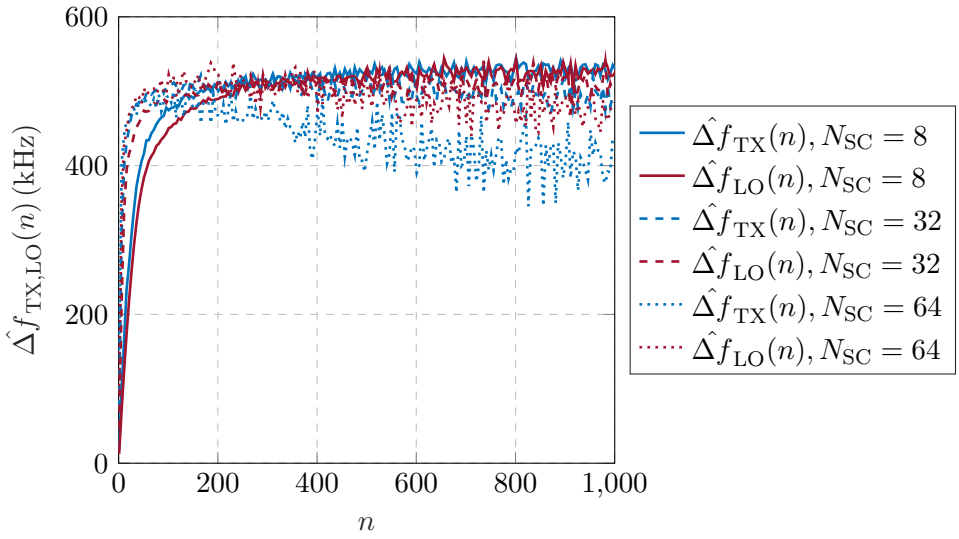

Figure 5.14: Estimation of $\Delta f_{\mathrm{TX,LO}}$ with the evolution of n, $\Delta f_{\mathrm{TX,LO}}$=500 kHz.

on the reference subcarriers, (5.8),

$$\begin{aligned} n' &= n(1 - R_{\mathrm{P}ref}) \\ &= n\left(\frac{N_{\mathrm{SC}}}{2} \cdot (1 - R_{\mathrm{P}})\right), \end{aligned} \tag{5.17}$$

by doing so, we can be sure that the misevaluation of the LLW is well solely attributed to the existence of the filtering and not dependent on any other factor. Figure 5.15 shows the result of performing the transformation from a n dependent on the number of subcarriers to an n' and, just as suspected, now the required value of n' overlaps regardless of the number of subcarriers (notice the difference on the scale of the horizontal axis).

Having achieved this independence of the number of subcarriers, it gives us a solid base for only doing the performance assessment of this digital monitoring technique for a single N_{SC} case, with the certainty that equivalent results would be achieved with any other possible N_{SC}. For the following results, the elected number of subcarriers will be 32, because it is the largest number of subcarriers for which the sampling size requirements can be met with a feasible number of simulated symbols. The optimum value of n', given the simulation scenario with a limited number of symbols simulated (2^{24} symbols) can be calculated from expressions (5.14) and (5.16). All we have to do is

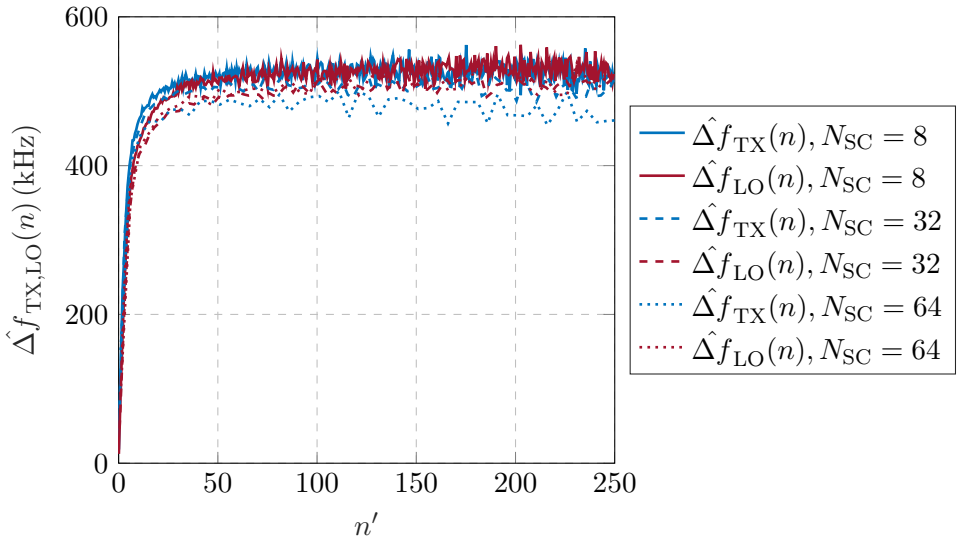

Figure 5.15: Estimation of $\Delta f_{\mathrm{TX,LO}}$ with the evolution of n', $\Delta f_{\mathrm{TX,LO}}$=500 kHz.

calculate the highest value of n' that still meets the sampling size requirement:

$$
\begin{aligned}
N &= \frac{2^{24}}{nN_{\mathrm{SC}}} \\
\Leftrightarrow \frac{z^2_{\alpha/2}\sigma^2}{E^2} &= \frac{2^{24}}{nN_{\mathrm{SC}}} \\
\Leftrightarrow \frac{2.576^2(2\pi\frac{nN_{\mathrm{SC}}}{64\mathrm{e}9}1\mathrm{e}6)^2}{0.05^2} &= \frac{2^{24}}{nN_{\mathrm{SC}}} \\
\Leftrightarrow \frac{2.576^2(2\pi\frac{1}{64\mathrm{e}9}1\mathrm{e}6)^2(nN_{\mathrm{SC}})^3}{0.05^2} &= 2^{24} \\
\Leftrightarrow n = \frac{2^8}{N_{\mathrm{SC}}}\sqrt[3]{\frac{0.05^2}{2.576^2(2\pi\frac{1}{64\mathrm{e}9}1\mathrm{e}6)^2}} \\
\Leftrightarrow n &\approx 272
\end{aligned}
$$

which, using expression (5.17), gives an n' of:

$$n' = n\left(\frac{N_{\mathrm{SC}}}{2}\cdot(1-R_{\mathrm{P}})\right) \approx 136$$

So far we have concluded that we can estimate the value of LLW without the impact of filtering and without a dependency with the N_{SC}. What we still need to evaluate, however, is the impact of the transmission length (originating different values of accumulated dispersion) and the impact of the ratio of how is the LLW distributed between the transmitter and the LO, because so far (in all experiments) it has been assumed an equally distributed LLW, that is, for the case of an overall LLW of 1 MHz, each of the two lasers have a LLW of 500 kHz. Note that this is the scenario in which the digital

monitoring really brings increased value, because if we always assumed the LLW to be the same in both lasers, a separation of the effects would not be required to perform digital monitoring of the respective LLW, it would be enough to monitor the LLW of the sum of the two effects and simply divide by a factor of two.

One particular interesting scenario to analyze is the case for which the LLW of the transmitter laser is much bigger than the one on the LO. In this scenario, the algorithm is expected to have worse performance, because when trying to extract the difference between the carrier phase estimations of the two reference subcarriers, they will be vastly similar, since the synchronous ϕ_{TX} component dominates the LPN. Given this fact, and considering that this algorithm is based on the accumulation of the differences between the LPN estimates, low values of Δf_{LO} will lead to the differences between two reference subcarriers being majorly caused by Gaussian noise, and we will thus overestimate ϕ_{LO}. Let's see how do these two factors at play interact with each other. Figure 5.16 shows the result of the estimation of the LLWs of the transmitter and LO lasers as a function of n'. For this scenario, the simulation parameters were similar to the ones on the last figure, but now changing the values of LLWs to Δf_{TX}=50 kHz and Δf_{LO}=5 kHz. Analyzing the results in Figure 5.16, we can see how there seems to be a huge error on the estimates of the value of LLWs. The Δf_{LO} has been overestimated by a factor of over 600%, and this error is dragged to the estimate of Δf_{TX}, also experiencing a big error of 60%. This invalidates the digital monitoring technique. Errors should be kept at a low value, to keep the interest in the digital monitoring.

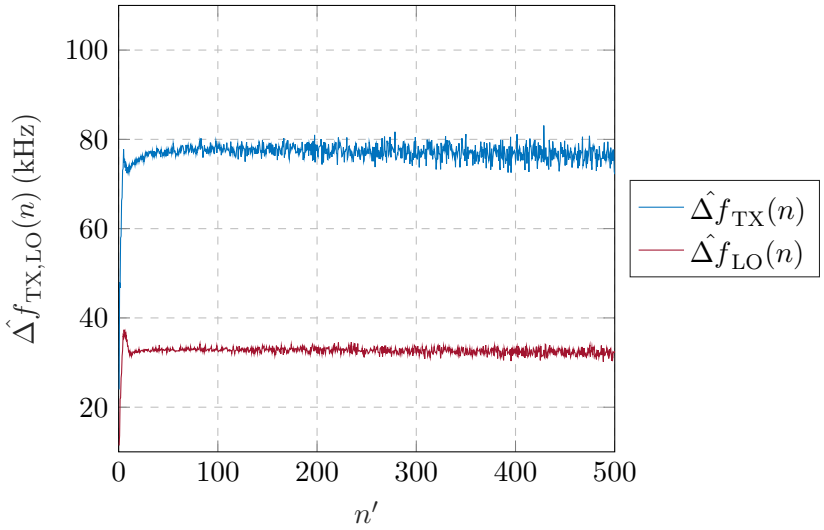

Figure 5.16: Estimation of $\Delta f_{\mathrm{TX,LO}}$ with the evolution of n', with Δf_{TX}=50 kHz and Δf_{LO}=5 kHz.

At this stage, we know that, in some critical cases, the performance of the digital monitoring technique is not anywhere near what would be desirable. This raises a question: is there any way we can improve these estimates? Is there any information that is not being used? In fact, there is. Let us look at Figure 5.17, where the block diagram of the DRS algorithm is revisited. Up to this point, estimates for Δf_{TX} and Δf_{LO} have been calculated from $\hat{\phi}_{\mathrm{TX}}$ and $\hat{\phi}_{\mathrm{LO}}$, points (3) and (4) in the figure, respectively. It has been shown that these estimates are worsened by the interplay between the cumulative

nature of the DRS algorithm and the Gaussian noise. However, at points (1) and (2) of the figure we have very good estimates of the overall LPN affecting two different subcarriers. And we know, from Section 2.2, that if we were to estimate the effective LLW of the overall LPN, Δf_{PN}, it would equal the sum of Δf_{TX} and Δf_{LO}. Let us do exactly that then, using $\hat{\phi}_{\text{PN},m}$, $\hat{\phi}_{\text{PN},n}$ and expression (5.16) to estimate Δf_{PN}. In Figure 5.18, the results of this estimate are displayed over the results of the previous figure.

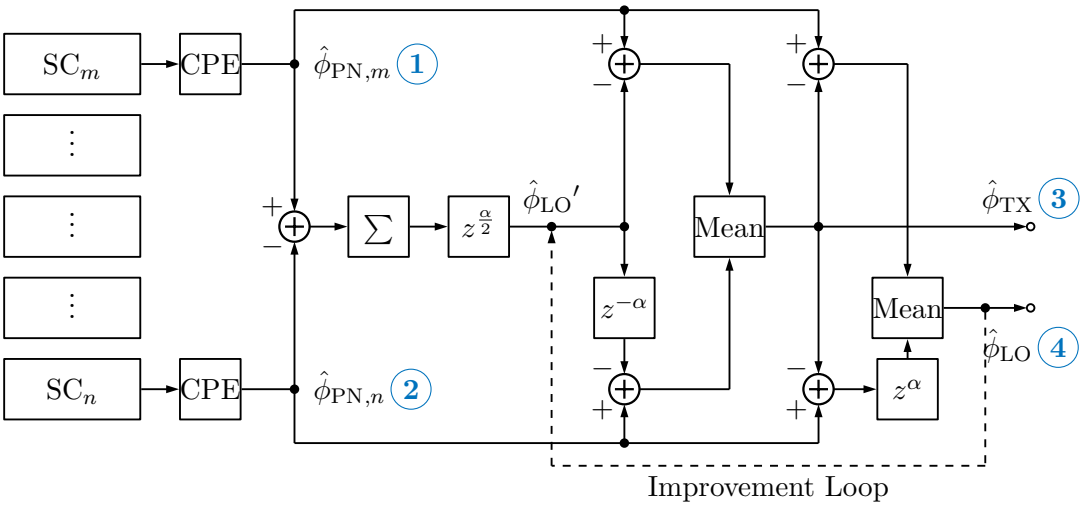

Figure 5.17: Recall of the block diagram of the DRS algorithm, with four moments labeled, moments in which LPN estimations are achieved.

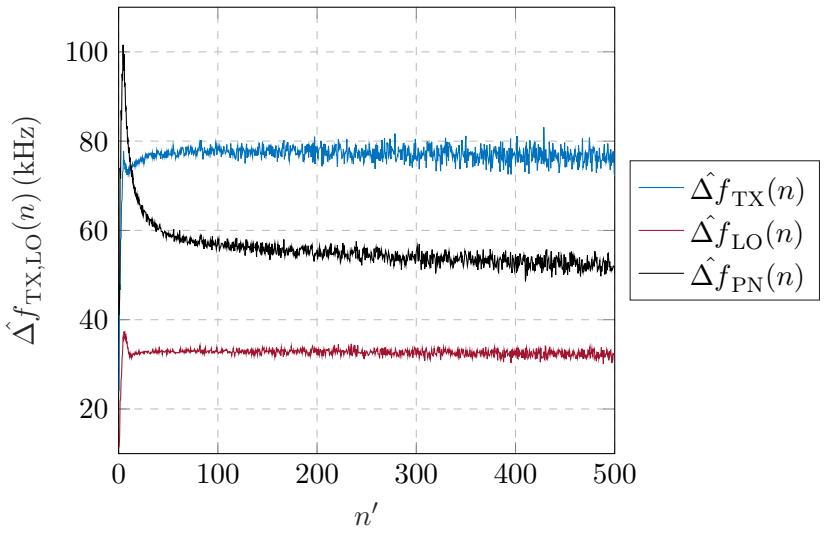

Figure 5.18: Estimation of $\Delta f_{\text{TX,LO,PN}}$ with the evolution of n', Δf_{TX}=50 kHz and Δf_{LO}=5 kHz, with the addition of the estimate of Δf_{PN}, having a theoretical value of 55 kHz.

Let us then focus our attention on the value of $\hat{\Delta f}_{\text{PN}}$. We can see how it is numer-

ically verified that $\hat{\Delta f}_{\mathrm{PN}}$ is very close to the sum of the real values of the transmitter and LO LLWs. Even though Δf_{TX} and Δf_{LO} are not properly measured due to the low tolerance to Gaussian noise of the DRS algorithm, the estimate of the overall LPN is not affected, having it been measured in a stage before the application of the DRS algorithm, and it constitutes a good estimation of the sum of both values of Δf_{TX} and Δf_{LO}. This is a very important conclusion. Because we now have established a common ground and a solid base to build our LLW estimates, independent of this apparent weakness of the DRS algorithm. Now we can build a measure to remove the overestimation of the LLW values. If, for instance, Δf_{LO} is overestimated, and we know that Δf_{PN} has a fixed value, we can now estimate $\hat{\hat{\Delta}} f_{\mathrm{TX}}$, given by:

$$\hat{\hat{\Delta}} f_{\mathrm{TX}} = \hat{\Delta f}_{\mathrm{PN}} - \hat{\Delta f}_{\mathrm{LO}} \tag{5.18}$$

this will result in a second estimate of the value of Δf_{TX}, but suffering an underestimation of the same magnitude as the overestimation of Δf_{LO}. Similarly, we can do the same for Δf_{LO} and obtain $\hat{\hat{\Delta}} f_{\mathrm{TX}}$. Figure 5.19 displays the addition of the lines of $\hat{\hat{\Delta}} f_{\mathrm{TX}}$ and $\hat{\hat{\Delta}} f_{\mathrm{LO}}$ over the results of the previous figure. Analyzing the entire panorama, we can take an interesting conclusion. The quantity of LLW at play in these over/underestimations is always the same value. This means that by averaging both pairs of estimates we will obtain as a result a much better estimate of $\Delta f_{\mathrm{TX,LO}}$. Furthermore, it is possible to conclude that this quantity at play in the over/underestimations is a function of the variance of the Gaussian noise affecting each of the LPN reconstructions.

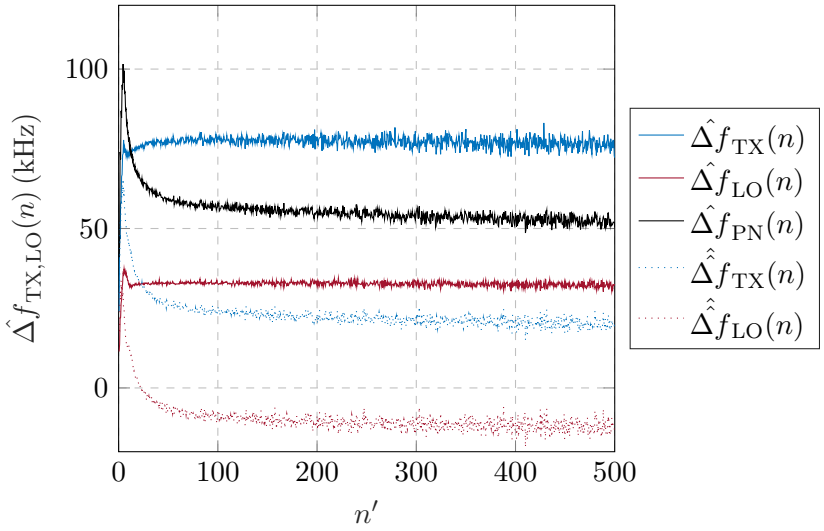

Figure 5.19: Estimation of $\Delta f_{\mathrm{TX,LO,PN}}$ with the evolution of n', using two different approaches for the estimation of $\Delta f_{\mathrm{TX,LO}}$, Δf_{TX}=50 kHz and Δf_{LO}=5 kHz.

From this point on, our values for the LPN estimates will be obtained averaging the values of the direct estimate of the LLW and the indirect estimate, through the complement between the overall LLW and the remaining LLW, of the other laser. These improved estimates can be seen in Figure 5.20. We can see on this figure how we were able to immensely reduce the error on the LLW estimates of both lasers, the error on $\hat{\Delta f}_{\mathrm{TX}}$ decreased from an error of over 60% to an error visibly below 10%. For $\hat{\Delta f}_{\mathrm{LO}}$ the

error is still relatively large, in the order of the 100%, however, while that represents a major relative error, we must bear in mind that, in a context in which the transmitter LLW is in the order of 50 kHz, an error of 5 kHz still represents a relative error below 10% taking into account the LLW of the overall LPN, still resulting in a fairly good estimate of the laser whose contribution is the biggest to the overall LPN.

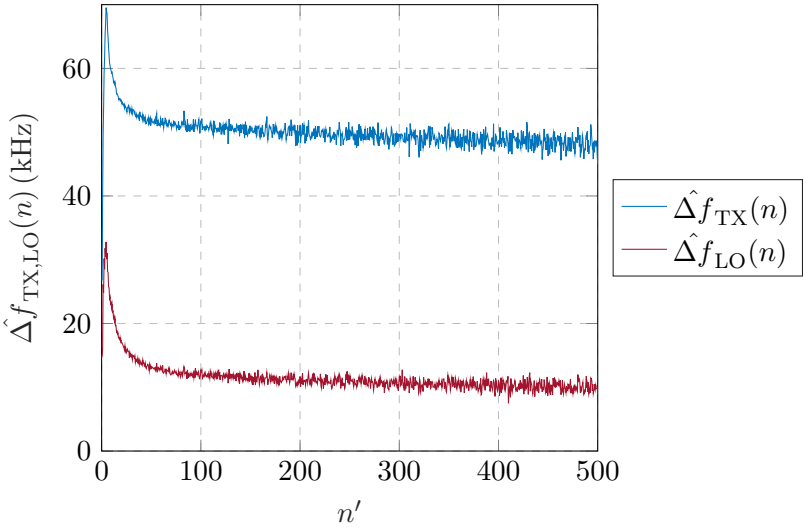

Figure 5.20: Improved estimation of $\Delta f_{\mathrm{TX,LO}}$ with the evolution of n', Δf_{TX}=50 kHz and Δf_{LO}=5 kHz.

Now that we have understood how to obtain the best estimates, optimizing the value of n', given the simulation limitations, and removing the impact of Gaussian noise on the estimate of the LLW, we are ready to test the performance of this digital monitoring technique in a wider range of simulations. To that end, a subset of tests was defined, encompassing all possible combinations of the parameters on Table 5.2, resulting in a total of 343 tests, each with the non-varying parameters kept equal to the previous simulations of this section.

Parameter	Simulated Values
L (km)	500; 1000; 1500; 2000; 3000; 4000; 5000
Δf_{TX} (kHz)	5; 50; 100; 150; 200; 350; 500
Δf_{LO} (kHz)	5; 50; 100; 150; 200; 350; 500

Table 5.2: Varying parameters on the simulations executed for the estimation of the system LLWs.

The results are assessed on Tables 5.3 and 5.4. Firstly, in Table 5.3 we evaluate how each value of LLW was estimated, independently of it being the value of the transmitter or receiver laser and independently of the transmission length. Then, in Table 5.4 we focus our attention on the dependency of the quality of the LLW estimation on the transmission length. On these tables, both the average values of error and the maximum are shown. Although it is obvious that in real applications only the maximum error should be a valid criterion, in this simulated scenario the average value is also of interest,

to serve as a validation of the good performance of the algorithm, and under the claim that the maximum values for error were, in part, a consequence of the limitations we have in the number of simulated symbols.

Δf (kHz)	Average Error (kHz)	%	Max. Error (kHz)	%
5	5.6	111.2	18.9	377.3
50	4.2	8.4	14.9	29.7
100	3.6	3.6	13.5	13.5
150	4.1	2.8	16.3	10.8
200	4.2	2.1	13.6	6.8
350	6.8	2.0	21.2	6.1
500	10.8	2.2	29.7	5.9

Table 5.3: Assessment of the estimates of each LLW in the several simulations in which such LLW was used.

Table 5.3 shows successful results on the estimation of the values of LLW. Each line corresponds to 98 different simulations, from the set of simulations performed. We see that very low values of LLW result in big percentage errors, which can be attributed to the higher relative weight of the Gaussian noise relative to the variance of the LPN process. For any evaluated LLW above or equal to 50 kHz we obtained an average percentage error of 10 percent, and even the extreme cases of the largest errors measured do not present enormous errors, never crossing the 30 percent barrier. Concerning the maximum values of error, we can see how they have a tendency to decrease with the increase of the LLW, which is in agreement with our previous conclusion that Gaussian noise may present more impact on the estimation of the LLW when it has a higher relative weight. Now, moving to the analysis of Table 5.4, in which each line corresponds to a total of 14 simulations, the LLW estimation does not show particular dependency on the transmission length. This is true except for really low LLWs, where a slight improvement was observed with the increase in the transmission length. This can be attributed to the fact that the increase in the transmission length contributes to larger accumulated CD, and consequently to a higher variance of the LPN, which increases the tolerance to the Gaussian noise responsible for lowering the correctness of the estimates.

To finalize this assessment, one thing that is left to analyze is how well can we evaluate what is the most impacting LLW between the contributions of the transmitter's and the receiver's laser, as a function of the ratio between both of their LLW. In the end, this is the most important aspect in which the digital monitoring technique must not fail, because being able to evaluate correctly which laser makes the worst contribution to LPN is what will allow a flexible system to adapt itself to a strategy that minimizes the impact of EEPN. For that objective, a new metric is defined, a Percentage of the Normalized Difference (PND) between the two estimates of the lasers of the same system. Considering two lasers, with a Δf ratio that corresponds to the smaller Δf, Δf_-, over the larger Δf, Δf_+, ($\Delta f_-/\Delta f_+$), PND is calculated using these two values of Δf and their respective estimates:

$$\text{PND} = \frac{\hat{\Delta f}_+ - \hat{\Delta f}_-}{\Delta f_+ - \Delta f_-} \times 100(\%) \tag{5.19}$$

L (km)	Δf (kHz)	Average Error (kHz)	%	Max. Error (kHz)	%
500	5	8.0	160.4	17.3	346.3
	150	7.6	5.0	16.3	10.8
	500	10.2	2.0	27.8	5.6
1000	5	8.4	169.0	18.9	377.3
	150	4.5	3.0	11.0	7.4
	500	10.4	2.1	29.7	5.9
1500	5	4.2	83.8	13.2	264.2
	150	3.1	2.1	9.6	6.4
	500	10.0	2.0	17.5	3.5
2000	5	4.2	83.5	14.2	284.4
	150	3.6	2.4	11.2	7.5
	500	12.9	2.6	20.6	4.1
3000	5	4.3	85.9	10.3	206.5
	150	2.4	1.6	5.9	3.9
	500	10.5	2.1	20.3	4.1
4000	5	4.6	92.7	12.2	244.9
	150	3.8	2.5	8.8	5.9
	500	10.8	2.2	19.9	4.0
5000	5	5.3	106.5	12.2	244.7
	150	3.7	2.5	9.4	6.3
	500	11.1	2.2	23.2	4.6

Table 5.4: Assessment of the LLW estimates as a function of L.

With this formulation, PND can be seen as a margin of confidence on the claim that a given LLW is larger than the other. Its value is expected to be more critical for higher Δf ratios. Table 5.5 shows the results of this evaluation, showing that, with success, we can always with confidence identify the most impacting LLW, even with the not so ideal margins of error seen on Table 5.3. The minimum measured value for PND was 80%, which represents that, in the worse simulated scenario, we still had a gap between our estimates that was equivalent to 80% of the real gap between them.

Δf ratio interval	Average PND	Min. PND	Nr. of Sims.
$[0; 1/40[$	106.6	104.1	28
$[1/40; 1/10[$	107.3	100.3	42
$[1/10; 1/4[$	106.5	99.0	56
$[1/4; 1/3[$	106.2	99.4	42
$[1/3; 1/2[$	105.7	94.6	42
$[1/2; 2/3[$	106.5	90.2	42
$[2/3; 1[$	107.8	82.6	42

Table 5.5: PND values for several $\Delta f_{-}/\Delta f_{+}$ ratios.

This section ends with the validation that we can always estimate with a reasonable amount of precision the LLWs of the transmitter and receiver lasers. This can be an interesting premise to new advanced flexible transceivers, because it allows the transceiver

to adapt to the impact of the LPN on the received signal. Possible adaptations include simpler things, such as the adaptation of the required PR and of the number of taps, given a certain impact of the LPN. But, a more interesting application can be the change of the CD mitigation approach, to minimize the impact of EEPN. Note that, while we have seen that the only contributor to EEPN was the LO LPN, that was only because we opted for post-detection CDE techniques, at the receiver. However, if we employ CD compensation based on the pre-distortion of the signal at the transmitter, the laser whose LLW contributes to EEPN is the one in the transmitter. Thus, if we know which laser has the highest LLW contribution, we could adapt our approach such that the contribution of EEPN is minimized.

Intentionally blank page.

Chapter 6

Conclusions and Future Work

6.1 Conclusions

In this thesis the limitations concerning carrier phase estimation as the subcarrier symbol rate decreases were evaluated and discussed, giving rise to alternative and more viable approaches that allow very small symbol rates, which wouldn't otherwise be possible with such low power requirements. This opens new doors to the full exploitation of the advantages of small symbol rates on the nonlinear fiber impairments effects.

In Chapter 3 we analyzed how much of a penalty is there associated with the choice of maintaining independent intra-subcarrier Carrier Phase Estimation (CPE). Considering that Laser Phase Noise (LPN) is estimated at best as fast as the symbol rate, and that the symbol rate is increasing inversely proportional to the number of subcarriers of the system, an increasing penalty is measured for a respectively increasing number of subcarriers, completely invalidating systems with a higher number of subcarriers even for commercially low values of Laser Line Width (LLW). Still in the same chapter, and being aware that Multi-Subcarrier (MSC) systems have a better tolerance to linear fiber impairments, we analyzed how did the general relation between the number of subcarriers and the performance behave when there is accumulated dispersion at play. The results revealed the existence of a clear compromise, between the number of subcarriers chosen and the time granularity of the LPN estimation, a compromise which was optimized for a number of four subcarriers, corresponding to a transmission rate of 16 GBaud. This left us with the hope that, once we could eliminate the impact of the low granularity on the CPE, we would remove one of the two limitations. Turning this compromise into a clear choice for a higher number of subcarriers. All we have to do is to increase the frequency of LPN estimation in a system that is apparently limited by the increasing symbol rate.

In Chapter 4 we introduced, implemented and assessed the performance of four different approaches to inter-subcarrier jointly processed CPE algorithms, with the fundamental goal of matching the LPN estimation periodicity achieved with single-carrier systems. In a Back-to-Back (B2B) simulation, these techniques could, in fact, remove the limitation of MSC systems, and successfully match the performance of single-carrier systems in the absence of accumulated dispersion. This was validated through simulations. The main objective of this thesis was to develop key methods that would allow MSC systems to match the performance of single-carrier systems, and it seemed to be concluded with success. However, once the performance was assessed in the presence of

Chromatic Dispersion (CD), the results did not match our expectations. The collaborative estimation of LPN removed the tolerance to CD previously measured on Chapter 3, in fact, any of the jointly processed schemes revealed a worse performance than the one of single-carrier systems. It was concluded that this was due to the assumption that the affecting LPN was the same on all subcarriers, and it demanded for another approach to jointly processed CPE. This chapter ends with the conclusion that the best approach so far was to simply use independently processed subcarriers, obeying the compromise between CD tolerance and the performance of the CPE algorithm. Moreover, it was also concluded that it must not be disregarded that nevertheless, these jointly processing techniques still represent the best choice for scenarios in which the transmission medium does not present significant dispersion. A particular case is free-space optical communication, which can still use these jointly processed techniques and possibly benefit from the longer symbol period.

Finally, in Chapter 5 the impact of assuming all the LPN for all the subcarriers was better understood, and, from that point, a novel approach was designed, the Dual-Reference Subcarrier (DRS) CPE. This novel approach has as a base concept the acknowledgment of two separable contributions to LPN, the transmitter laser's LPN and the Local Oscillator (LO)'s and uses two reference subcarriers to reconstruct them. We concluded that the performance was closer to optimum when the two reference subcarriers are positioned in the first and third quarters of the subcarriers agglomerate, but the ideal separation decreases as the transmission length increases. The achievable performance did not seem significantly better than the independently processed schemes for four and eight subcarriers, but it must be kept in mind that this was the first time a viable and CD tolerant jointly processing scheme was achieved, one that has results better than any other approach and at a smaller level of complexity, requiring only a single stage of CPE. Moreover, it enables the use of much higher numbers of subcarriers, without any significant measured impact with the change of the symbol rate, thus accomplishing the main objective of this thesis. Still in this chapter, a novel digital monitoring technique is studied, one whose door was opened by the nature of the DRS CPE. We have concluded that, with no significant additional complexity, the CPE can also serve as a monitoring subsystem, to evaluate the contributions of each of the two lasers of the system to the overall LPN, which opens a new research opportunity, allowing modern flexible transceivers to adapt the CPE approach in accordance to the measured LLWs to maximize performance, or even adapting systems parameters as required, such as the Pilot rate or the number of taps.

6.2 Future Work

While there has already been some extensive and thorough assessment of the DRS CPE, having been explored in several configurations and scenarios, it is now required to evaluate its performance in an experimental setup, namely, to fully explore the advantages brought by the tolerance of fiber nonlinear impairments, which haven't been considered on the simulated environment. Future work encompasses the following steps:

- Development of offline simulation and performance assessment with real experimental data and still resorting to the same simulator used on this thesis, for the digital signal processing of the receiver;

- Performing any necessary adjustment on the algorithm to be optimized for the contributions of Non-Linear Phase Noise (NLPN) in MSC signals;
- Hardware implementation, resorting to a Field Programmable Gate Array (FPGA), and experimental validation of the DRS algorithm, making use of the fiber transmission testbed provided by Instituto de Telecomunicações;
- Writing of a conference/journal paper reporting the experimentally achieved results;

Intentionally blank page.

Bibliography

[1] Peter J. Winzer. Scaling optical fiber networks: Challenges and solutions. *Opt. Photon. News*, 26(3):28–35, Mar 2015.

[2] Xiang Zhou and Chongjin Xie. *Enabling Technologies for High Spectral-Efficiency Coherent Optical Communication Networks*. John Wiley & Sons, Ltd, 2016.

[3] X. Liu, S. Chandrasekhar, and P. J. Winzer. Digital signal processing techniques enabling multi-tbs superchannel transmission: An overview of recent advances in dsp-enabled superchannels. *IEEE Signal Processing Magazine*, 31(2):16–24, 2014.

[4] John C. Cartledge, Fernando P. Guiomar, Frank R. Kschischang, Gabriele Liga, and Metodi P. Yankov. Digital signal processing for fiber nonlinearities. *Opt. Express*, 25(3):1916–1936, Feb 2017.

[5] G. Bosco. Advanced modulation techniques for flexible optical transceivers: The rate/reach tradeoff. *Journal of Lightwave Technology*, 37(1):36–49, 2019.

[6] P. Poggiolini, A. Nespola, Y. Jiang, G. Bosco, A. Carena, L. Bertignono, S. M. Bilal, S. Abrate, and F. Forghieri. Analytical and experimental results on system maximum reach increase through symbol rate optimization. *Journal of Lightwave Technology*, 34(8):1872–1885, 2016.

[7] Meng Qiu, Qunbi Zhuge, Mathieu Chagnon, Yuliang Gao, Xian Xu, Mohamed Morsy-Osman, and David V. Plant. Digital subcarrier multiplexing for fiber nonlinearity mitigation in coherent optical communication systems. *Opt. Express*, 22(15):18770–18777, Jul 2014.

[8] M. Cantono, F. P. Guiomar, A. Carena, and V. Curri. Networking benefit of multi-subcarrier transceivers. In *2018 Optical Fiber Communications Conference and Exposition (OFC)*, pages 1–3, 2018.

[9] H. Sun, M. Torbatian, M. Karimi, R. Maher, S. Thomson, M. Tehrani, Y. Gao, A. Kumpera, G. Soliman, A. Kakkar, M. Osman, Z. A. El-Sahn, C. Doggart, W. Hou, S. Sutarwala, Y. Wu, M. R. Chitgarha, V. Lal, H. Tsai, S. Corzine, J. Zhang, J. Osenbach, S. Buggaveeti, Z. Morbi, M. Iglesias Olmedo, I. Leung, X. Xu, P. Samra, V. Dominic, S. Sanders, M. Ziari, A. Napoli, B. Spinnler, K. Wu, and P. Kandappan. 800g dsp asic design using probabilistic shaping and digital sub-carrier multiplexing. *Journal of Lightwave Technology*, pages 1–1, 2020.

[10] O. Golani, D. Pilori, F. P. P. Guiomar, G. Bosco, A. Carena, and M. Shtaif. Correlated nonlinear phase-noise in multi-subcarrier systems: Modeling and mitigation. *Journal of Lightwave Technology*, 38(6):1148–1156, 2020.

[11] Fernando Guiomar, Luca Bertignono, Antonino Nespola, and Andrea Carena. Mitigation of transceiver bandwidth limitations using multi-subcarrier signals. pages 1–4, 07 2017.

[12] S. M. Bilal, C. Fludger, and G. Bosco. Carrier phase estimation in multi-subcarrier coherent optical systems. *IEEE Photonics Technology Letters*, 28(19):2090–2093, 2016.

[13] David James Krause, Han Sun, Yuejian Wu, John McNicol, and Kuang-Tsan Wu. Channel carrying multiple digital subcarriers, U.S. Patent 20140092924, Apr. 2014.

[14] Han Henry Sun, Abdullah Karar, Kuang-Tsan Wu, and Ahmed Awadalla. Transmission of subcarriers having different modulation formats, U.S. Patent 20160323039, Nov. 2016.

[15] Kuang-Tsan Wu and Mitshell L. Mitchell. Individually routable digital subcarriers, U.S. Patent 20190181960, Jun. 2019.

[16] Han Henry Sun, Kuang-Tsan Wu, Steven Joseph Hand, and Jeffrey T. Rahn. Clock recovery for digital subcarriers for optical networks, U.S. Patent 20190245643, Aug. 2019.

[17] Gary Mak and Mohammad Sotoodeh. Subcarrier power balance control, U.S. Patent 9577762, Feb. 2017.

[18] A. Carena, V. Curri, R. Gaudino, P. Poggiolini, and S. Benedetto. A time-domain optical transmission system simulation package accounting for nonlinear and polarization-related effects in fiber. *IEEE Journal on Selected Areas in Communications*, 15(4):751–765, 1997.

[19] A. Carena, V. Curri, G. Bosco, P. Poggiolini, and F. Forghieri. Modeling of the impact of nonlinear propagation effects in uncompensated optical coherent transmission links. *Journal of Lightwave Technology*, 30(10):1524–1539, 2012.

[20] Andrea Carena, Gabriella Bosco, Vittorio Curri, Yanchao Jiang, Pierluigi Poggiolini, and Fabrizio Forghieri. Egn model of non-linear fiber propagation. *Opt. Express*, 22(13):16335–16362, Jun 2014.

[21] Fernando P. Guiomar, Jacklyn D. Reis, Andrea Carena, Gabriella Bosco, António L. Teixeira, and Armando N. Pinto. Experimental demonstration of a frequency-domain volterra series nonlinear equalizer in polarization-multiplexed transmission. *Opt. Express*, 21(1):276–288, Jan 2013.

[22] Somayeh Ziaie, Nelson J. Muga, Fernando P. Guiomar, Gil M. Fernandes, Ricardo M. Ferreira, Ali Shahpari, António L. Teixeira, and Armando Nolasko Pinto. Experimental assessment of the adaptive stokes space-based polarization demultiplexing for optical metro and access networks. *J. Lightwave Technol.*, 33(23):4968–4974, Dec 2015.

[23] Kazuro Kikuchi. Fundamentals of Coherent Optical Fiber Communications. 34(1):1–23, 2016.

[24] G. P. Agrawal. *Fiber-optic communication systems.* John Wiley & Sons, 4th edition, 2010.

[25] Georgios Tzimpragos, Christoforos Kachris, Ivan B. Djordjevic, Milorad Cvijetic, Dimitrios Soudris, and Ioannis Tomkos. A Survey on FEC Codes for 100 G and beyond Optical Networks. *IEEE Communications Surveys and Tutorials*, 18(1):209–221, 2016.

[26] R. Schmogrow, S. Wolf, B. Baeuerle, D. Hillerkuss, B. Nebendahl, C. Koos, W. Freude, and J. Leuthold. Nyquist frequency division multiplexing for optical communications. In *2012 Conference on Lasers and Electro-Optics (CLEO)*, pages 1–2, 2012.

[27] Takahito Tanimura, Shoichiro Oda, Toshiki Tanaka, Takeshi Hoshida, Zhenning Tao, and Jens C. Rasmussen. A simple digital skew compensator for coherent receiver. *European Conference on Optical Communication, ECOC*, (1):1–2, 2009.

[28] Trung Hien Nguyen, Pascal Scalart, Mathilde Gay, Laurent Bramerie, Olivier Sentieys, Jean Claude Simon, Christophe Peucheret, and Michel Joindot. Blind transmitter IQ imbalance compensation in M-QaM optical coherent systems. *Journal of Optical Communications and Networking*, 9(9):D42–D50, 2017.

[29] Meng Qiu, Qunbi Zhuge, Mathieu Chagnon, Yuliang Gao, Xian Xu, Mohamed Morsy-Osman, and David V. Plant. Digital subcarrier multiplexing for fiber nonlinearity mitigation in coherent optical communication systems. *Optics Express*, 22(15):18770, 2014.

[30] F. P. Guiomar, L. Bertignono, A. Nespola, and A. Carena. Frequency-domain hybrid modulation formats for high bit-rate flexibility and nonlinear robustness. *Journal of Lightwave Technology*, 36(20):4856–4870, 2018.

[31] F. P. Guiomar, A. Carena, G. Bosco, L. Bertignono, A. Nespola, and P. Poggiolini. Nonlinear mitigation on subcarrier-multiplexed pm-16qam optical systems. *Opt. Express*, 25(4):4298–4311, Feb 2017.

[32] E. Ip and J. M. Kahn. Compensation of dispersion and nonlinear impairments using digital backpropagation. *Journal of Lightwave Technology*, 26(20):3416–3425, 2008.

[33] E. Ip. Nonlinear compensation using backpropagation for polarization-multiplexed transmission. *Journal of Lightwave Technology*, 28(6):939–951, 2010.

[34] F. P. Guiomar and A. N. Pinto. Simplified volterra series nonlinear equalizer for polarization-multiplexed coherent optical systems. *Journal of Lightwave Technology*, 31(23):3879–3891, 2013.

[35] F. P. Guiomar, S. B. Amado, C. S. Martins, and A. N. Pinto. Time-domain volterra-based digital backpropagation for coherent optical systems. *Journal of Lightwave Technology*, 33(15):3170–3181, 2015.

[36] Kazuro Kikuchi. Performance analyses of polarization demultiplexing based on constant-modulus algorithm in digital coherent optical receivers. *Opt. Express*, 19(10):9868–9880, May 2011.

[37] I Fatadin, D Ives, and S J Savory. Blind Equalization and Carrier Phase Recovery in a {16-QAM} Optical Coherent System. 27(15):3042–3049, 2009.

[38] F. Gardner. A bpsk/qpsk timing-error detector for sampled receivers. *IEEE Transactions on Communications*, 34(5):423–429, 1986.

[39] R. M. Ferreira, J. D. Reis, S. B. Amado, A. Shahpari, F. P. Guiomar, J. R. F. Oliveira, A. N. Pinto, and A. L. Teixeira. Performance and complexity of digital clock recovery for nyquist udwdm-pon in real time. *IEEE Photonics Technology Letters*, 27(21):2230–2233, 2015.

[40] Benedikt Baeuerle, Arne Josten, Felix Abrecht, Marco Eppenberger, Edwin Dornbierer, David Hillerkuss, and Juerg Leuthold. Multi-format carrier recovery for coherent real-time reception with processing in polar coordinates. *Optics Express*, 24(22):25629, 2016.

[41] J. C. M. Diniz, J. C. R. F. de Oliveira, E. S. Rosa, V. B. Ribeiro, V. E. S. Parahyba, R. da Silva, E. P. da Silva, L. H. H. de Carvalho, A. F. Herbster, and A. C. Bordonalli. Simple feed-forward wide-range frequency offset estimator for optical coherent receivers. *Opt. Express*, 19(26):B323–B328, Dec 2011.

[42] R. M. Ferreira, A. Shahpari, S. B. Amado, M. Drummond, J. D. Reis, A. N. Pinto, and A. L. Teixeira. Optimized carrier frequency and phase recovery based on blind m th power schemes. *IEEE Photonics Technology Letters*, 28(21):2439–2442, 2016.

[43] D. Rife and R. Boorstyn. Single tone parameter estimation from discrete-time observations. *IEEE Transactions on Information Theory*, 20(5):591–598, 1974.

[44] S. Hoffmann, S. Bhandare, T. Pfau, O. Adamczyk, C. Wordehoff, R. Peveling, M. Porrmann, and R. Noe. Frequency and phase estimation for coherent qpsk transmission with unlocked dfb lasers. *IEEE Photonics Technology Letters*, 20(18):1569–1571, 2008.

[45] O. E. Agazzi, M. R. Hueda, H. S. Carrer, and D. E. Crivelli. Maximum-likelihood sequence estimation in dispersive optical channels. *Journal of Lightwave Technology*, 23(2):749–763, 2005.

[46] D. Zibar, M. Piels, R. Jones, and C. G. Schäeffer. Machine learning techniques in optical communication. *Journal of Lightwave Technology*, 34(6):1442–1452, 2016.

[47] Timo Pfau, Sebastian Hoffmann, and Reinhold Noé. Hardware-efficient coherent digital receiver concept with feedforward carrier recovery for m-qam constellations. *J. Lightwave Technol.*, 27(8):989–999, Apr 2009.

[48] A. Viterbi. Nonlinear estimation of psk-modulated carrier phase with application to burst digital transmission. *IEEE Transactions on Information Theory*, 29(4):543–551, 1983.

[49] S M Bilal, G Bosco, J Cheng, A P T Lau, and C Lu. Carrier Phase Estimation Through the Rotation Algorithm for {64-QAM} Optical Systems. *J. Lightwave Technol.*, 33(9):1766–1773, may 2015.

[50] X. Zhou. An improved feed-forward carrier recovery algorithm for coherent receivers with m -qam modulation format. *IEEE Photonics Technology Letters*, 22(14):1051–1053, 2010.

[51] M. G. Taylor. Coherent detection method using dsp for demodulation of signal and subsequent equalization of propagation impairments. *IEEE Photonics Technology Letters*, 16(2):674–676, 2004.

[52] G. Goldfarb and G. Li. Chromatic dispersion compensation using digital iir filtering with coherent detection. *IEEE Photonics Technology Letters*, 19(13):969–971, 2007.

[53] Seb J. Savory. Digital filters for coherent optical receivers. *Opt. Express*, 16(2):804–817, Jan 2008.

[54] B. Spinnler. Equalizer design and complexity for digital coherent receivers. *IEEE Journal of Selected Topics in Quantum Electronics*, 16(5):1180–1192, 2010.

[55] T. Xu, G. Jacobsen, S. Popov, M. Forzati, J. Mårtensson, M. Mussolin, J. Li, K. Wang, Y. Zhang, and A. T. Friberg. Frequency-domain chromatic dispersion equalization using overlap-add methods in coherent optical system. *Journal of Optical Communications*, 32(2), Jan 2011.

[56] Jochen Leibrich and Werner Rosenkranz. Frequency domain equalization with minimum complexity in coherent optical transmission systems. *Optics InfoBase Conference Papers*, pages 1–3, 2010.

[57] C. S. Martins, F. P. Guiomar, S. B. Amado, R. M. Ferreira, S. Ziaie, A. Shahpari, A. L. Teixeira, and A. N. Pinto. Distributive fir-based chromatic dispersion equalization for coherent receivers. *Journal of Lightwave Technology*, 34(21):5023–5032, 2016.

[58] Mahdi Malekiha, Igor Tselniker, and David V. Plant. Chromatic dispersion mitigation in long-haul fiber-optic communication networks by sub-band partitioning. *Optics Express*, 23(25):32654, 2015.

[59] M. Magarini, L. Barletta, A. Spalvieri, F. Vacondio, T. Pfau, M. Pepe, M. Bertolini, and G. Gavioli. Pilot-symbols-aided carrier-phase recovery for 100-g pm-qpsk digital coherent receivers. *IEEE Photonics Technology Letters*, 24(9):739–741, May 2012.

[60] Fernando Guiomar. OptDSP: Digital signal processing MATLAB library for the simulation of coherent optical communication systems (v1.1), September 2017.

[61] A. Alvarado, E. Agrell, D. Lavery, R. Maher, and P. Bayvel. Replacing the soft-decision fec limit paradigm in the design of optical communication systems*. *Journal of Lightwave Technology*, 34(2):707–721, 2016.

[62] William Shieh and Keang-Po Ho. Equalization-enhanced phase noise for coherent-detection systems using electronic digital signal processing. *Opt. Express*, 16(20):15718–15727, Sep 2008.

[63] M. P. Yankov, L. Barletta, and D. Zibar. Low-complexity joint sub-carrier phase noise compensation for digital multi-carrier systems. In *2017 European Conference on Optical Communication (ECOC)*, pages 1–3, 2017.

[64] David Martinez, Yojiro Mori, Hiroshi Hasegawa, and Ken ichi Sato. Novel subcarrier multiplexing and subcarrier-synchronous phase estimation tolerant to laser phase noise. In *Advanced Photonics 2017 (IPR, NOMA, Sensors, Networks, SPPCom, PS)*, page SpW1F.5. Optical Society of America, 2017.

[65] A. M. Rosa Brusin, F. P. Guiomar, A. Lorences-Riesgo, P. P. Monteiro, and A. Carena. Enhanced resilience towards roadm-induced optical filtering using subcarrier multiplexing and optimized bit and power loading. *Opt. Express*, 27(21):30710–30725, Oct 2019.

[66] Douglas C. Montgomery and George C. Runger. *Applied Statistics and Probability for Engineers*. John Wiley & Sons, Inc., 3rd edition, 2002.